UNTANGLING ROOT TOPOLOGY IN PLANT PHENOTYPING DATA: FROM 2D ROOT HAIR ANALYSIS TO 3D ROOT ARCHITECTURE RECONSTRUCTION

by

PETER JACEK PIETRZYK

(Under the Direction of ALEXANDER BUCKSCH)

ABSTRACT

Roots play a central role in how plants acquire water and nutrients and are therefore critical for plant growth and stress tolerance. Because of their importance, root traits are increasingly targeted in breeding programs. However, their measurement remains difficult due to their complex, three-dimensional branching structures. Capturing root traits therefore requires accurate image data and robust computational methods. Although imaging methods such as microscopy and Structure-from-Motion (SfM) have improved over the past decades, the resulting measurements often contain structural ambiguities that complicate trait extraction. This can be seen in root hairs that overlap in 2D images, and in 3D reconstructions, where roots may cross and form intersections that are not part of the actual root architecture. These artifacts affect how roots are represented digitally and distort measurements of traits such as root hair length, lateral root density, or branching hierarchy.

In this dissertation I address this problem by developing algorithms that resolve intersections in 2D and 3D root structures. I present a method that identifies and separates intersecting root hairs in microscopy images, allowing the measurement of individual hairs across different species. Further, I optimize camera calibration in a 3D scanner to improve the quality of root reconstructions based on Structure from Motion, resulting in higher quality point clouds that can ultimately lead to better skeletonization and more reliable trait measurements. Finally, I develop an algorithm to resolve intersecting roots in 3D skeletons of root systems. Many root systems contain cycles that arise when branches cross in the point cloud. These cycles are removed when individual roots are detected, and the skeleton is restructured into a tree, allowing traits such as lateral root length and topology to be measured more accurately.

Together, these projects improve the accuracy of root phenotyping across different spatial scales. The algorithms I developed support measuring actual traits rather than indirect proxies or aggregated traits. Therefore, they contribute to a better understanding of root system architecture and enable the use of detailed root traits in studies of plant function and in breeding for more resilient crops.

INDEX WORDS: computer vision, phenotyping, root architecture, root hair, simulated annealing

UNTANGLING ROOT TOPOLOGY IN PLANT PHENOTYPING DATA: FROM 2D ROOT HAIR ANALYSIS TO 3D ROOT ARCHITECTURE RECONSTRUCTION

by

PETER JACEK PIETRZYK

B.Sc., Delft University of Technology, The Netherlands, 2012

M.Sc., Delft University of Technology, The Netherlands, 2015

A Dissertation Submitted to the Graduate Faculty of The University of Georgia in Partial Fulfillment of the Requirements for the Degree

DOCTOR OF PHILOSOPHY

ATHENS, GEORGIA

2025

UNTANGLING ROOT TOPOLOGY IN PLANT PHENOTYPING DATA: FROM 2D ROOT HAIR ANALYSIS TO 3D ROOT ARCHITECTURE RECONSTRUCTION

by

PETER JACEK PIETRZYK

Major Professor:	Alexander Bucksch
Committee:	Chris J. Peterson Shannon Quinn Christopher N. Topp

Electronic Version Approved:

Ron Walcott
Vice Provost for Graduate Education and Dean of the Graduate School
The University of Georgia
May 2025

ACKNOWLEDGEMENTS

I would first like to express my deepest gratitude to my advisor, Dr. Alexander Bucksch, for his guidance and support throughout my Ph.D. journey. He always gave feedback because he wanted me to get better, and over time, I have learned to value the importance of being resilient and thinking independently. I am incredibly grateful for the opportunities he has given me and for the mentorship that has shaped both my academic and personal growth.

I am also sincerely grateful to the members of my Ph.D. committee, Dr. Chris Peterson, Dr. Shannon Quinn, and Dr. Chris Topp, for their encouragement, patience, and invaluable insights.

A heartfelt thank you to Dr. Wolfgang Lukowitz, Dr. Shu-Mei Chang, Dr. John Burke, and Dr. Lisa Donavan for their mentorship, guidance, and continuous support—especially during my start at UGA, throughout the pandemic, my time alone at UGA, and during my transition back to Germany. I deeply appreciate everything they have done for me.

I am also incredibly thankful to Dr. Paola Barriga for her mentorship in teaching and her support in my professional development. Her guidance helped me grow immensely, not only in teaching but also as a person, giving me confidence throughout this challenging journey.

A special thank you to Dr. Patompong Saengwilai for his collaboration and guidance, which led to the development of DIRT/μ, as well as to his students, Neen Phan-Udom and Chartinun Chutoe, for their contributions. I also deeply appreciate the collaboration and support from Dr. Marc Libault and Dr. Lise Pingault on this project. I further would like to thank Joshua Carpenter for sharing data that made my final project on refining 3D root skeletons possible.

To all the members of the Computational Plant Science Lab, thank you for your help, support, and camaraderie. I would especially like to acknowledge Dr. Suxing Liu for his assistance in scanning roots and generating point clouds, and Wes Bonelli for helping me build Docker containers for DIRT/μ. My thanks also go to those who have been there for me in the lab: Dr. Margaret Frank, Dr. Ankita Roy, Dr. Chris Cotter, Jordan Knapp-Wilson, William LaVoy, and Jitrana Kengkanna. Your support has meant a lot to me.

I am also incredibly grateful to my friends, Melinda Guzman, Dr. Alan Peper, Dr. Piotr Tuczapski, Johnny Chen, Carter Newton and Dr. Andries Temme, for reminding me to take a step back, go camping and enjoy life beyond research. Your friendship has been a source of joy, balance and adventure.

Finally, I want to express my deepest appreciation to my mom, dad, and sister for their unconditional love and support. Your belief in me has been my greatest strength, and I could not have done this without you.

TABLE OF CONTENTS

APPENDICES

LIST OF TABLES

Page

LIST OF FIGURES

CHAPTER 1

INTRODUCTION AND LITERATURE REVIEW

Roots: Form, Function and Importance

In agricultural systems, phenotypic traits of plants play an important role in quantifying their productivity and adaptation to environmental stressors, particularly in the context of climate change and increasingly nutrient-depleted soils (Bucksch et al., 2017). As the global climate continues to undergo rapid transformations, which include changing temperatures and precipitation patterns as well as severe weather events, breeders are facing challenges to adapt crops to these new environments. In this context, understanding the interplay between genotype, environment, and phenotype is essential for breeding new crop varieties that can sustain and improve global food production (Hickey et al., 2019). One of the key components of a plant's ability to adapt to the changing environment is its root system, which to a large extent controls the uptake of resources, stress tolerance, and yield. Within this context, this dissertation focuses on improving computational phenotyping of root and root hair traits.

Roots are essential for the growth and survival of plants because they provide the interface between them and the soil. They play a critical role in water and nutrient absorption, and anchorage of the plant in the soil, and therefore directly influence the growth of the plant, its stress resistance, and overall fitness (Herder et al., 2010). In particular, root system architecture, which is the spatial configuration of roots, plays an important role in how plants tolerate drought and nutrient limitations in the soil (Lynch, 2019). Deeper root systems allow plants to absorb water and nutrients, such as nitrogen from deeper soils (Lynch, 2019; Lynch & Wojciechowski, 2015). Traits that are related to deeper roots, such as steeper root growth angles, are genetically controlled, and can maintain rice yields even in drought conditions (Uga et al., 2013). Similarly, in wheat, it was shown that lines with deeper roots achieved higher grain yield by accessing water in deeper soils under water-limited conditions (Wasson et al., 2012). These examples suggest that breeding crops for specific root traits may improve crop yield under water-limited conditions.

It is known that certain root traits enable better acquisition of nutrients from the soil and thus reduce the need for fertilizer in agricultural systems (Paez-Garcia et al., 2015). One example is that root architectures with fewer and longer lateral roots in maize plants improve the uptake of nitrogen (Zhan et al., 2015). Furthermore, root hairs, which are hair-like outgrowths from epidermal cells (Roy & Bucksch, 2021), greatly increase the root surface area and support the plant in absorbing water and nutrients from the soil (Carminati et al., 2017; Marin et al., 2021; Saengwilai et al., 2021). They are in particular helpful in absorbing immobile nutrients, such as phosphorus, from the soil by extending into non-depleted zones, areas in the soil that contain these nutrients (Jungk, 2001; Ma, Bielenberg, et al., 2001; Ma, Walk, et al., 2001). In combination with other root architecture traits, root hair traits can have synergistic effects in nutrient acquisition. A study on common bean found that phenotypes with long root hairs and shallow basal roots led to a 298% increase in biomass under low-phosphorus conditions compared to a phenotype with short root hairs and deep roots (Miguel et al., 2015). This phenotype was thus much more effective at acquiring P from the topsoil. Further, it was shown that the development of root hairs can depend on the root type (Nestler et al., 2016), indicating that a targeted selection of root traits is required to improve nutrient absorption. In general, many studies have now linked specific root traits, such as root depth, branching patterns, or root hair length, to better nutrient acquisition and stress tolerance, highlighting the importance of roots for improved breeding strategies.

Despite their critical role, root traits have historically been underexploited in breeding programs largely because of the difficulties in their measurement and phenotyping (Lynch, 2019). Traditional methods, such as root washing and manual tracing, are labor-intensive, destructive, and prone to measurement biases (Poorter et al., 2023). However, new developments in imaging and computational analysis are starting to shift this view, opening new possibilities for the integration of root traits into crop breeding strategies (Bucksch et al., 2014). The following sections give an overview of approaches for root phenotyping, the limitations of current methods, and the specific challenges that motivate this dissertation's focus.

Overview of Root Phenotyping Approaches

Traditional methods for studying roots often involve excavation and destructive sampling. One approach for phenotyping roots is *shovelomics*, which is defined as digging up roots with a shovel, washing them, and then scoring root architectural traits in a high-throughput manner (Trachsel et al., 2010). This approach allows measurements of traits such as root number, length, angles, and branching in field-grown plants. Soil coring results in samples of the roots at different depths of the soil, by extracting a cylinder of soil from the soil and washing the roots (Wasson et al., 2014). To observe roots in the natural soil environment, researchers have also developed methods to image roots *in situ*. One approach is the use of *minirhizotrons*, which are transparent tubes with a camera, that are inserted in the soil to observe roots as they grow, thus allowing repeated observations over time (Vamerali et al., 2012). Vincent et al. (2017) have also used these systems to measure root hair development in the soil. Similarly, *rhizoslides* and *rhizoboxes* allow imaging of roots that grow along a transparent surface, thus facilitating 2D imaging of the root architecture (Le Marié et al., 2014; Mašková & Weiser, 2019). Nevertheless, these systems provide limited insights into the complete spatial arrangement of the root system.

In the past two decades, modern technologies have revolutionized root phenotyping (Atkinson et al., 2019; Li et al., 2022). X-ray computed tomography (CT) and magnetic resonance imaging (MRI) provide three-dimensional (3D) measurements of roots within the soil, allowing detailed measurements of root structures and even root hairs (Claussen et al., 2023; Duncan et al., 2022). However, despite their advantages, these techniques are often limited due to their costs and restrictions on sample size and are therefore less suitable for large-scale experiments required in breeding programs. Nonetheless, they have greatly enhanced our ability to phenotype roots non-destructively.

Researchers have developed high-resolution and low-cost two-dimensional (2D) and 3D imaging systems to address limitations of destructive sampling and expensive non-destructive methods. High-resolution 2D imaging platforms using flatbed scanners or digital cameras allow the acquisition of images of washed roots, which can be analyzed using image analysis software. These simpler imaging setups are cheaper and more accessible to more labs than X-ray CT and MRI. Flatbed scanner systems allow high-resolution 2D scanning of washed roots spread in water or on a tray. Software such as RhizoVision Explorer can be then used to automatically measure traits like total length, average diameter, and branching counts (Seethepalli et al., 2021). The online platform Digital Imaging of Root Traits (DIRT), on the other hand, was specifically developed to be used in the field, thereby increasing the throughput of *shovelomics* and increasing the number of measurable traits (Das et al., 2015). Other software packages include GiA Roots (Galkovskyi et al., 2012), EZ-Root-VIS (Shahzad et al., 2018), and RootNav (Pound et al., 2013), which have greatly accelerated data processing, enabling larger experiments and new definitions of root traits. Notably, high-magnification microscopy together with automated image analysis can also be used to measure root hair traits (Guichard et al., 2019; Lu et al., 2022; Vincent et al., 2017). Image-based 3D reconstruction of roots, using methods such as Structure from Motion (SfM), is a newer cost-efficient approach to root phenotyping (Liu et al., 2021; Liu et al., 2023). By taking many 2D images of an excavated root system from different angles, researchers can generate a 3D model (i.e. a point cloud) of the root structure. While limited by the fact that roots may be damaged during excavation and cleaning, this method has made high-resolution root phenotyping more accessible for field-grown crops.

Challenges in Root Phenotyping

Despite these innovations, measuring traits of root hairs and the root system architecture with high throughput and accuracy remains difficult. Factors that make root phenotyping difficult are the structural complexity of roots, occlusions and intersections in 2D and 3D data, limitations of proxy-based measurements, and trade-offs between precision and throughput.

Structural Complexity: Root systems are among the most complex organs to phenotype due to their intricate branching structures and heterogeneity (Ryan et al., 2016). A single mature crop plant can have thousands of roots, ranging from a thick, woody taproot to fine root hairs, intertwined in three dimensions. This complexity makes it difficult to capture and analyze the entire root system across all spatial scales. Further, roots may have interdependent traits. Therefore, measuring one trait in isolation can miss the structural or functional context provided by other traits. This interdependence complicates comprehensive phenotyping, because meaningful interpretation often requires analyzing traits in combination, and not as separate and independent variables.

Occlusions and Intersections: In both 2D images and 3D models, roots and root hairs overlap or obscure one another, complicating the extraction of individual traits such as root hair length or the precise architecture of branching patterns (Bucksch, 2014; Choudhury et al., 2019).

Missed roots or merged root segments can lead to underestimation or overestimation of traits like root count, length, or average diameter. Addressing these errors related to occlusion is crucial for improving the accuracy of high-throughput root phenotyping pipelines.

Proxy-Based Measurement Limitations: Traditional metrics (like total root length or root:shoot ratio) capture only a fraction of the architecture's information. More detailed descriptors, like branching angles, individual root lengths, or topological indices exist, but require high-quality data and robust algorithms. Many automated root phenotyping methods rely on indirect measurements (e.g., estimating root hair traits based on pixel counts) rather than resolving individual root hairs. Such measurements might show that a plant has overall more root hairs or more roots, but not which aspect of root hairs or root architecture (e.g. root hair density, number of lateral roots, etc.).

Trade-Offs Between Precision and Throughput: A recurring theme in plant phenotyping and breeding is the balance between measuring traits accurately and measuring them in large quantities (Grondin et al., 2022). Some manual measurements can be more accurate but slow to measure, and on the other hand, automated methods are often fast but often approximate root traits rather than precisely measuring them.

These challenges underscore the need for advanced computational approaches that can resolve complex root structures and enable more precise trait measurements. A key bottleneck for this is to resolve structural intersections to measure individual root components rather than relying on aggregated or proxy-based metrics, which will be addressed in this dissertation.

Overview of Dissertation

The challenges outlined above underscore the need for more robust and scalable phenotyping methods. To bridge this gap, this dissertation presents three projects aimed at advancing computational root phenotyping. This work makes it possible to precisely extract biologically important traits by resolving root hairs that cross each other in 2D microscopy images and root branches in 3D skeletons of root structures. The work further shows that optimizing image acquisition settings for 3D root scanning can improve the quality of trait measurements. Together, these contributions help bridge the gap between high-throughput imaging and biologically accurate trait quantification, ensuring that root traits can be effectively linked to plant performance in breeding programs.

The second chapter focuses on the phenotyping of root hairs. Traditionally, root hair measurements have been done manually using optical 2D microscopes, a process that is both time-consuming and susceptible to bias. To overcome this, an automated pipeline called DIRT/μ (Digital Imaging of Root Traits at Microscale) was developed. This algorithm uses advanced image analysis and combinatorial optimization to resolve overlapping and intersecting root hairs in 2D images. The algorithm extracts individual root hair traits such as length, density, and curvature with high precision. By automating this process, DIRT/μ enables high-throughput phenotyping of root hairs, thereby making it feasible to include these traits in large-scale genetic studies and breeding programs.

The third chapter focuses on optimizing camera settings for a multi-camera root scanning system, which uses SfM to generate 3D root models. By calibrating camera settings such as focus, aperture, exposure time, and gain, this study demonstrates that careful parameter selection significantly improves model quality, reducing noise, which cannot be removed in post-processing steps, and enhancing trait extraction accuracy. This project provides a systematic evaluation of how camera calibration influences model quality, offering practical guidelines to improve the reproducibility and accuracy of 3D root phenotyping studies.

The fourth chapter shows a method for resolving intersecting branches in 3D root skeletons. The experimental work extends the algorithm used in DIRT/μ from 2D to 3D and integrates new features to resolve intersecting roots. The aim is to be able to reconstruct root branching patterns, improving our ability to quantify root architecture traits in three dimensions. Existing methods struggle to resolve overlapping root branches, leading to inaccurate trait estimates. Resoling intersecting roots in 3D root skeletons thus provides a more precise and detailed representation of root architecture.

References

Atkinson, J. A., Pound, M. P., Bennett, M. J., & Wells, D. M. (2019). Uncovering the hidden half of plants using new advances in root phenotyping. *Current Opinion in Biotechnology*, *55*, 1-8. https://doi.org/https://doi.org/10.1016/j.copbio.2018.06.002

Bucksch, A. (2014). A practical introduction to skeletons for the plant sciences. *Applications in Plant Sciences*, *2*(8), Article 1400005. https://doi.org/10.3732/apps.1400005

Bucksch, A., Atta-Boateng, A., Azihou, A. F., Battogtokh, D., Baumgartner, A., Binder, B. M., Braybrook, S. A., Chang, C., Coneva, V., DeWitt, T. J., Fletcher, A. G., Gehan, M. A., Diaz-Martinez, D. H., Hong, L. L., Iyer-Pascuzzi, A. S., Klein, L. L., Leiboff, S., Li, M., Lynch, J. P., . . . Chitwood, D. H. (2017). Morphological Plant Modeling: Unleashing Geometric and Topological Potential within the Plant Sciences. *Frontiers in Plant Science*, *8*, Article 900. https://doi.org/10.3389/fpls.2017.00900

Bucksch, A., Burridge, J., York, L. M., Das, A., Nord, E., Weitz, J. S., & Lynch, J. P. (2014). Image-based high-throughput field phenotyping of crop roots. *Plant Physiol*, *166*(2), 470-486. https://doi.org/10.1104/pp.114.243519

Carminati, A., Passioura, J. B., Zarebanadkouki, M., Ahmed, M. A., Ryan, P. R., Watt, M., & Delhaize, E. (2017). Root hairs enable high transpiration rates in drying soils. *New Phytologist*, *216*(3), 771-781. https://doi.org/10.1111/nph.14715

Choudhury, S. D., Samal, A., & Awada, T. (2019). Leveraging Image Analysis for High-Throughput Plant Phenotyping. *Frontiers in Plant Science*, *10*, Article 508. https://doi.org/10.3389/fpls.2019.00508

Claussen, J., Wittenberg, T., Uhlmann, N., & Gerth, S. (2023). "Chamber #8" - a holistic approach of high-throughput non-destructive assessment of plant roots. *Front Plant Sci*, *14*, 1269005, Article 1269005. https://doi.org/10.3389/fpls.2023.1269005

Das, A., Schneider, H., Burridge, J., Ascanio, A. K. M., Wojciechowski, T., Topp, C. N., Lynch, J. P., Weitz, J. S., & Bucksch, A. (2015). Digital imaging of root traits (DIRT): a high-throughput computing and collaboration platform for field-based root phenomics. *Plant Methods*, *11*(1), 51. https://doi.org/10.1186/s13007-015-0093-3

Duncan, K. E., Czymmek, K. J., Jiang, N., Thies, A. C., & Topp, C. N. (2022). X-ray microscopy enables multiscale high-resolution 3D imaging of plant cells, tissues, and organs. *Plant Physiol*, *188*(2), 831-845. https://doi.org/10.1093/plphys/kiab405

Galkovskyi, T., Mileyko, Y., Bucksch, A., Moore, B., Symonova, O., Price, C. A., Topp, C. N., Iyer-Pascuzzi, A. S., Zurek, P. R., Fang, S., Harer, J., Benfey, P. N., & Weitz, J. S. (2012). GiA Roots: software for the high throughput analysis of plant root system architecture. *Bmc Plant Biology*, *12*(1), 116. https://doi.org/10.1186/1471-2229-12-116

Grondin, A., Bhosale, R., Atkinson, J. A., Faye, A., Jones, D. H., Benson, E., Burridge, J., Sine, B., Vadez, V., Pridmore, T., Wells, D. M., Laplaze, L., Kane, N. A., & Bennett, M. J. (2022). High-throughput root phenotyping : opportunities and challenges for the adaptation of arid and semi arid crops to future climates. In N. A. Kane, D. Foncéka, & T. J. Dalton (Eds.), *Crop adaptation and improvement for drought-prone environments* (pp. 258-282). New Prairie Press. https://hal.science/hal-04169654

Guichard, M., Allain, J. M., Bianchi, M. W., & Frachisse, J. M. (2019). Root Hair Sizer: an algorithm for high throughput recovery of different root hair and root developmental parameters. *Plant Methods*, *15*(1), Article 104. https://doi.org/10.1186/s13007-019-0483-z

Herder, G. D., Van Isterdael, G., Beeckman, T., & De Smet, I. (2010). The roots of a new green revolution. *Trends in plant science*, *15*(11), 600-607. https://doi.org/10.1016/j.tplants.2010.08.009

Hickey, L. T., N. Hafeez, A., Robinson, H., Jackson, S. A., Leal-Bertioli, S. C. M., Tester, M., Gao, C., Godwin, I. D., Hayes, B. J., & Wulff, B. B. H. (2019). Breeding crops to feed 10 billion. *Nature Biotechnology*, *37*(7), 744-754. https://doi.org/10.1038/s41587-019-0152-9

Jungk, A. (2001). Root hairs and the acquisition of plant nutrients from soil. *Journal of Plant Nutrition and Soil Science*, *164*(2), 121-129.

Le Marié, C., Kirchgessner, N., Marschall, D., Walter, A., & Hund, A. (2014). Rhizoslides: paper-based growth system for non-destructive, high throughput phenotyping of root development by means of image analysis. *Plant Methods*, *10*(1), 13. https://doi.org/10.1186/1746-4811-10-13

Li, A., Zhu, L., Xu, W., Liu, L., & Teng, G. (2022). Recent advances in methods for in situ root phenotyping. *PEERJ*, *10*, e13638, Article e13638. https://doi.org/10.7717/peerj.13638

Liu, S. X., Barrow, C. S., Hanlon, M., Lynch, J. P., & Bucksch, A. (2021). DIRT/3D: 3D root phenotyping for field-grown maize (Zea mays). *Plant Physiology*, *187*(2), 739-757. https://doi.org/10.1093/plphys/kiab311

Liu, Y., Lv, Z., Zhang, Q., Zhao, J., Fang, Z., Gao, Z., & Su, Y. (2023). Comparison Study of Three Camera Calibration Methods Considering the Calibration Board Quality and 3D Measurement Accuracy. *Experimental Mechanics*, *63*(2), 289-307. https://doi.org/10.1007/s11340-022-00905-y

Lu, W., Wang, X., & Jia, W. (2022). Root hair image processing based on deep learning and prior knowledge. *Computers and Electronics in Agriculture*, *202*, Article 107397. https://doi.org/10.1016/j.compag.2022.107397

Lynch, J. P. (2019). Root phenotypes for improved nutrient capture: an underexploited opportunity for global agriculture. *New Phytologist*, *223*(2), 548-564. https://doi.org/10.1111/nph.15738

Lynch, J. P., & Wojciechowski, T. (2015). Opportunities and challenges in the subsoil: pathways to deeper rooted crops. *Journal of Experimental Botany*, *66*(8), 2199-2210. https://doi.org/10.1093/jxb/eru508

Ma, Z., Bielenberg, D. G., Brown, K. M., & Lynch, J. P. (2001). Regulation of root hair density by phosphorus availability in Arabidopsis thaliana. *Plant Cell and Environment*, *24*(4), 459-467. https://doi.org/10.1046/j.1365-3040.2001.00695.x

Ma, Z., Walk, T. C., Marcus, A., & Lynch, J. P. (2001). Morphological synergism in root hair length, density, initiation and geometry for phosphorus acquisition in Arabidopsis thaliana: A modeling approach. *Plant and Soil*, *236*(2), 221-235. https://doi.org/10.1023/a:1012728819326

Marin, M., Feeney, D. S., Brown, L. K., Naveed, M., Ruiz, S., Koebernick, N., Bengough, A. G., Hallett, P. D., Roose, T., Puertolas, J., Dodd, I. C., & George, T. S. (2021). Significance of root hairs for plant performance under contrasting field conditions and water deficit. *Annals of botany*, *128*(1), 1-16. https://doi.org/10.1093/aob/mcaa181

Mašková, T., & Weiser, M. (2019). The roles of interspecific variability in seed mass and soil resource availability in root system development. *Plant and Soil*, *435*(1), 395-406. https://doi.org/10.1007/s11104-018-3896-y

Miguel, M. A., Postma, J. A., & Lynch, J. P. (2015). Phene Synergism between Root Hair Length and Basal Root Growth Angle for Phosphorus Acquisition. *Plant Physiology*, *167*(4), 1430-U1504. https://doi.org/10.1104/pp.15.00145

Nestler, J., Keyes, S. D., & Wissuwa, M. (2016). Root hair formation in rice (Oryza sativa L.) differs between root types and is altered in artificial growth conditions. *Journal of Experimental Botany*, *67*(12), 3699-3708. https://doi.org/10.1093/jxb/erw115

Paez-Garcia, A., Motes, C. M., Scheible, W. R., Chen, R., Blancaflor, E. B., & Monteros, M. J. (2015). Root Traits and Phenotyping Strategies for Plant Improvement [article]. *Plants (Basel)*, *4*(2), 334-355. https://doi.org/10.3390/plants4020334

Poorter, H., Hummel, G. M., Nagel, K. A., Fiorani, F., von Gillhaussen, P., Virnich, O., Schurr, U., Postma, J. A., van de Zedde, R., & Wiese-Klinkenberg, A. (2023). Pitfalls and potential of high-throughput plant phenotyping platforms [Methods]. *Frontiers in Plant Science*, *14*. https://doi.org/10.3389/fpls.2023.1233794

Pound, M. P., French, A. P., Atkinson, J. A., Wells, D. M., Bennett, M. J., & Pridmore, T. (2013). RootNav: Navigating Images of Complex Root Architectures *Plant Physiology*, *162*(4), 1802-1814. https://doi.org/10.1104/pp.113.221531

Roy, A., & Bucksch, A. (2021). Root hairs vs. trichomes: Not everyone is straight! *Current Opinion in Plant Biology*, *64*, Article 102151. https://doi.org/10.1016/j.pbi.2021.102151

Ryan, P. R., Delhaize, E., Watt, M., & Richardson, A. E. (2016). Plant roots: understanding structure and function in an ocean of complexity. *Annals of botany*, *118*(4), 555-559. https://doi.org/10.1093/aob/mcw192

Saengwilai, P., Strock, C., Rangarajan, H., Chimungu, J., Salungyu, J., & Lynch, J. P. (2021). Root hair phenotypes influence nitrogen acquisition in maize. *Annals of botany*, *128*(7), 849-858. https://doi.org/10.1093/aob/mcab104

Seethepalli, A., Dhakal, K., Griffiths, M., Guo, H., Freschet, G. T., & York, L. M. (2021). RhizoVision Explorer: open-source software for root image analysis and measurement standardization. *AoB PLANTS*, *13*(6). https://doi.org/10.1093/aobpla/plab056

Shahzad, Z., Kellermeier, F., Armstrong, E. M., Rogers, S., Lobet, G., Amtmann, A., & Hills, A. (2018). EZ-Root-VIS: A Software Pipeline for the Rapid Analysis and Visual Reconstruction of Root System Architecture. *Plant Physiology*, *177*(4), 1368-1381. https://doi.org/10.1104/pp.18.00217

Trachsel, S., Kaeppler, S. M., Brown, K. M., & Lynch, J. P. (2010). Shovelomics: high throughput phenotyping of maize (Zea mays L.) root architecture in the field. *Plant and Soil*, *341*(1-2), 75-87. https://doi.org/10.1007/s11104-010-0623-8

Uga, Y., Sugimoto, K., Ogawa, S., Rane, J., Ishitani, M., Hara, N., Kitomi, Y., Inukai, Y., Ono, K., Kanno, N., Inoue, H., Takehisa, H., Motoyama, R., Nagamura, Y., Wu, J., Matsumoto, T., Takai, T., Okuno, K., & Yano, M. (2013). Control of root system architecture by DEEPER ROOTING 1 increases rice yield under drought conditions. *Nature Genetics*, *45*(9), 1097-1102. https://doi.org/10.1038/ng.2725

Vamerali, T., Bandiera, M., & Mosca, G. (2012). Minirhizotrons in Modern Root Studies. In S. Mancuso (Ed.), *Measuring Roots: An Updated Approach* (pp. 341-361). Springer Berlin Heidelberg. https://doi.org/10.1007/978-3-642-22067-8_17

Vincent, C., Rowland, D., Na, C., & Schaffer, B. (2017). A high-throughput method to quantify root hair area in digital images taken in situ. *Plant and Soil*, *412*(1-2), 61-80. https://doi.org/10.1007/s11104-016-3016-9

Wasson, A. P., Rebetzke, G. J., Kirkegaard, J. A., Christopher, J., Richards, R. A., & Watt, M. (2014). Soil coring at multiple field environments can directly quantify variation in deep root traits to select wheat genotypes for breeding. *Journal of Experimental Botany*, *65*(21), 6231-6249. https://doi.org/10.1093/jxb/eru250

Wasson, A. P., Richards, R. A., Chatrath, R., Misra, S. C., Prasad, S. V., Rebetzke, G. J., Kirkegaard, J. A., Christopher, J., & Watt, M. (2012). Traits and selection strategies to improve root systems and water uptake in water-limited wheat crops. *J Exp Bot*, *63*(9), 3485-3498. https://doi.org/10.1093/jxb/ers111

Zhan, A., Schneider, H., & Lynch, J. P. (2015). Reduced Lateral Root Branching Density Improves Drought Tolerance in Maize. *Plant Physiology*, *168*(4), 1603-U1885. https://doi.org/10.1104/pp.15.00187

CHAPTER 2

DIRT/µ: AUTOMATED EXTRACTION OF ROOT HAIR TRAITS USING COMBINATORIAL OPTIMIZATION [1]

---

[1] Pietrzyk, P., Phan-Udom, N., Chutoe, C., Pingault, L., Roy, A., Libault, M., Saengwilai, P. J., & Bucksch, A. (2024). DIRT/µ: automated extraction of root hair traits using combinatorial optimization. *Journal of Experimental Botany*, 76(2), 285-298. https://doi.org/10.1093/jxb/erae385

Reprinted here with permission of the publisher

Abstract

As with phenotyping of any microscopic appendages, such as cilia or antennae, phenotyping of root hairs has been a challenge due to their complex intersecting arrangements in two-dimensional images and the technical limitations of automated measurements. Digital Imaging of Root Traits at Microscale (DIRT/µ) is a newly developed algorithm that addresses this issue by computationally resolving intersections and extracting individual root hairs from two-dimensional microscopy images. This solution enables automatic and precise trait measurements of individual root hairs. DIRT/µ rigorously defines a set of rules to resolve intersecting root hairs and minimizes a newly designed cost function to combinatorically identify each root hair in the microscopy image. As a result, DIRT/µ accurately measures traits such as root hair length distribution and root hair density, which are impractical for manual assessment. We tested DIRT/µ on three datasets to validate its performance and showcase potential applications. By measuring root hair traits in a fraction of the time manual methods require, DIRT/µ eliminates subjective biases from manual measurements. Automating individual root hair extraction accelerates phenotyping and quantifies trait variability within and among plants, creating new possibilities to characterize root hair function and their underlying genetics.

Keywords: Abiotic stress, computer vision, microscopy, phenotyping, root hair, simulated annealing.

Introduction

Phenotypes exist across scales of organismal organization and change over time. This multiscale characteristic poses a major challenge in phenomics, making comprehensive measurement of phenotypes nearly impossible (Houle et al., 2010). Computational tools analysing digital images partly overcome this phenotyping problem and have been used to study the traits of human, animal, and plant phenotypes (Lürig et al., 2021). However, self-occlusions due to two-dimensional (2D) projection during imaging pose a major challenge for image-based measurements of phenotypes (Bucksch, 2014; Choudhury et al., 2019). This issue arises not only at large spatial scales, such as the branching of a tree, but also at the finest, microscopic scales. A common yet often small morphological trait present in many organisms is a collection of elongated appendages with important protective, physiological, or sensory functions, such as antennae, hairs, and trichomes, that are attached to the body of the organism (Seale et al., 2018). Each appendage has a simple linear morphology that could be easily traced and measured, but collectively, these appendages intersect with one another or can completely occlude one another when imaged. As a result, and despite the ubiquitous presence of elongated appendages in nature, computational tools to extract individual elongated appendages from images are scarce, making the comprehensive phenotyping of organisms with such appendages impossible.

An example of such appendages is root hairs, which are elongated epidermal cells of the root that laterally extend into the soil (Roy & Bucksch, 2021). Root hairs display distinguishing characteristics in length, density, and occurrence along the roots, which vary distinctively among species and genotypes and across environments. Root hair traits have been linked to higher water uptake and improved tolerance to drought (Cai & Ahmed, 2022; Carminati et al., 2017; Marin et al., 2021). In particular, the traits root hair length (RHL) and root hair density (RHD) have been further associated with increased tolerance to low levels of immobile nutrients in the soil. Under low levels of phosphorus (P), the traits RHL and RHD increase, and longer and denser root hairs increase P absorption (Ma, Bielenberg, et al., 2001; Ma, Walk, et al., 2001). Similar benefits have been described for low levels of mobile nutrients. Plants with longer root hairs have greater biomass under low nitrogen (N), a mobile nutrient, compared with plants with short root hairs (De Pessemier et al., 2022; Saengwilai et al., 2021). Root hair development can be separated into three distinct and complex pathways: the differentiation of epidermal root cells into root hair cells, the initiation of root hair growth, and root hair elongation. These underlie different and complex pathways (Libault et al., 2010), and therefore it is unsurprising that the control of RHL and RHD underlies separate genomic regions, for example in rice (Hanlon et al., 2023). Due to their role in nutrient and water uptake, root hairs provide an important breeding target for sustainable agriculture under drought and increasingly nutrient-depleted soils (Jungk, 2001; Rongsawat et al., 2021). To leverage the benefits of root hairs in agricultural production, the function and control of specific root hair traits must be addressed (Kohli et al., 2022).

Trait measurements of root hairs are challenging due to their small scale, three-dimensional (3D) nature, and often-complex arrangement. Microscopes, in combination with digital cameras, enable the capture of images of root hairs, which can be used to measure their traits. Bright-field and dark-field light microscopes, either compound or stereo, are the most common types for imaging root hairs due to their low cost and simple operation (Brown et al., 2012; Parker et al., 2000; Saengwilai et al., 2021). Other microscopy techniques, including confocal, electron, and light sheet fluorescence microscopy, can increase extractable information, but due to their higher cost, they are less accessible for most studies (Baumberger et al., 2003; Bibikova et al., 1998; Candeo et al., 2017; Czarnota et al., 2003; Singh et al., 2021). Similarly, imaging technologies for

3D measurements of root hairs exist but are financially unattainable for most labs and require data acquisition times that do not allow for high-throughput phenotyping (Daly et al., 2016; Keyes et al., 2017; Tracy et al., 2011). Root hairs can be counted and traced manually in microscopy images using software, such as ImageJ (Schindelin et al., 2012), to determine RHL and RHD. However, this manual task is time-consuming, tedious, and subjective to the researcher. On the other hand, determining these traits automatically is challenging due to the projection of root hairs onto a 2D plane, which causes combinatorial challenges to resolve the occlusions and intersections in the image data.

In recent years, semi-automated and automated methods have approached the combinatorial challenges with proxy measurements to phenotype root hairs. Vincent et al. (2017) used multivariate linear regression to determine root hair area *in situ* based on the machine-learning classification of root hair pixels in minirhizotron images. A method by Guichard et al. (2019) measures the length of mature root hairs, the distance of emerging root hairs to the root tip, and the length of the root hair growth zone and estimates the root hair growth rate, but this requires root hairs to grow orthogonal to the root and does not determine RHD. The results are based on slicing the profile of the root hairs along the root as a proxy measurement to quantify RHL and RHD, rather than measurements of individual root hairs. The results of this method were used to study the relevance of root hair traits for N acquisition in *Arabidopsis* (De Pessemier et al., 2022; Vincent et al., 2022). A third method, by Lu et al. (2022), classifies root hair pixels using deep learning to measure root hair area. Measured RHL is based on the length of a skeletal line of root hair regions across the entire image but does not separate individual hairs. All three methods identify root hair pixels with high accuracy but do not obtain actual counts of root hairs that resolve the complex challenges of occluding root hairs along an imaged root segment to calculate length and density traits.

In response to the challenges regarding root hair phenotyping, we developed Digital Imaging of Root Traits at Microscale (DIRT/μ), a method for extracting individual root hairs automatically from microscopy images in a statistically robust way. Our approach uses machine learning to classify image pixels as either root hair, root, or background because the 3D root hairs are being projected onto a 2D image plane. The projection leads to many intersections of root hairs in the imaging data whose resolution is beyond the capability of the human visual system. Resolving these many intersections in an image is non-trivial because every intersection of two or more root hairs can be resolved in multiple ways. Resolving this network of intersections can result in trillions of possible outcomes for a single image. We demonstrate that our approach works even in dense arrangements with many intersecting root hairs in a feasible time frame. As a result, we can measure the number of root hairs and the distribution of individual lengths and shapes. In this paper, we demonstrate the robustness and detail of the information derived from our method on three datasets.

Materials and Methods

The DIRT/μ algorithm works through sequential steps that begin by identifying image pixels as root hairs and result in the detection and representation of individual root hairs (Figure 2.1). First, image pixels are classified to distinguish between root hair, root, and background (Figure 2.1A-C). Next, a medial axis is extracted as the set of points equidistant from at least two boundary points of the classified root hair pixels, to represent its skeleton (Figure 2.1D). Then, we fit weighted splines to the medial axis, which are defined by a series of points representing

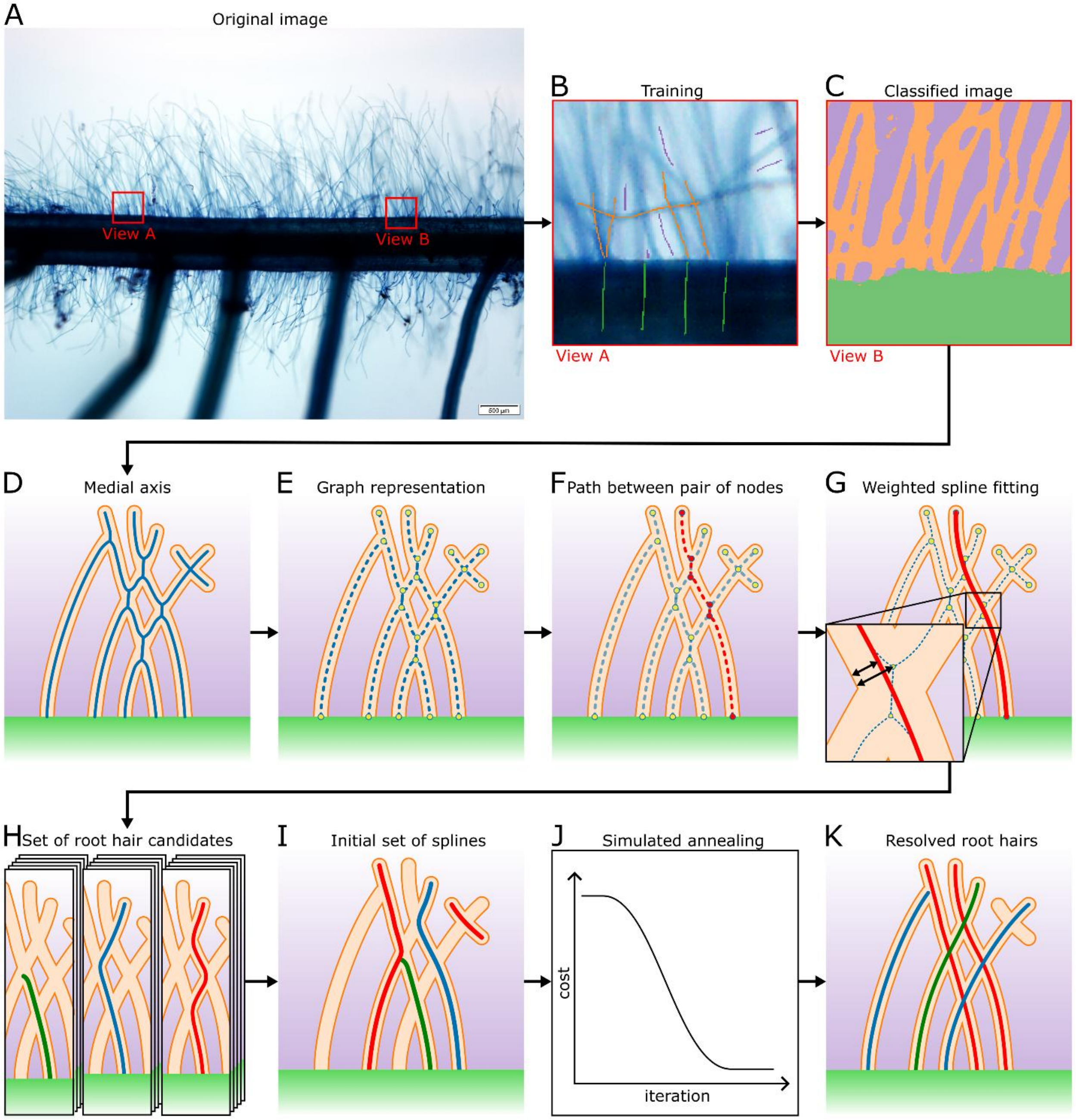

Figure 2.1: Workflow for extracting root hairs from a microscopy image. (A–C) To extract root hairs from a microscopy image (A), we create a training set with classes for root hair, root, and background (B) to classify pixels in the images (C). (D–F) We perform a medial axis transform on classified root hair pixels (D), identify junctions and termination points as nodes in the medial axis (E), and select a path between a set of two nodes (F). (G) Along the path, we fit a spline weighted by the diameter of the medial circle. (H) We repeat the weighted spline fitting for all close-by node pairs and retain only valid splines. (I–K) We select an initial set of random splines (I) and optimize the set using simulated annealing (J) to obtain fully reconstructed root hairs (K).

potential root hair segments, where each point has an associated weight influencing the shape of the curve (Figure 2.1E-G). The core idea of DIRT/μ is then to test whether combinations of these splines adhere to a priori criteria of root hair shape to compute iteratively a set of measurable root hairs (Figure 2.1I-K). The selected solution is the set of root hairs that minimizes the a priori criteria of root hair shape. The results enable us to compute estimations of traits, such as the number of root hairs, their shape, and their distribution. DIRT/μ is available on GitHub (Pietrzyk & Bucksch, 2022) and as a Docker container (Pietrzyk et al., 2022).

Ilastik classifies pixels to standardize input data across various imaging modalities

To reconstruct individual root hairs, we need to identify all pixels that correspond to root hairs. In addition, we need to identify pixels corresponding to the parent root to determine where root hairs emerge. We used the software ilastik to classify all image pixels as either root hair, root, or background (Berg et al., 2019), but any method resulting in a segmented tiff image could be used. The software provides a user interface to create training sets by manually annotating pixels according to their class and to preview the classification result interactively (Figure 2.1B). For the classification, we use a random forest classifier with features obtained from morphological filters on multiple spatial scales (Figure 2.1C; Supplementary Protocols S1, S2). Typically, a training set can be created within a few hours, and all root hair images from the same dataset can be classified in a batch process. Small segments of root hair or root are removed from the classified image (Supplementary Protocol S3). The benefit of using this machine-learning approach to classify pixels is that datasets obtained under different lab protocols can be used as input for DIRT/μ.

Building a relational graph data structure to order root hair segments

The classified image provides only rasterized data without information to identify individual root hairs. All the classified root hairs together result in a network of inseparable regions representing root hairs. We extract the medial axis from root hair pixels to create a relational graph of individual medial axis segments (Figure 2.1D; Supplementary Protocol S4). Each branching of the medial axis results from touching or intersecting root hairs. Each point on the medial axis is approximated by an image pixel and belongs to one of three types: (i) a termination point, if it has only one neighboring pixel on the medial axis; (ii) a medial axis segment (i.e. a line), if it has exactly two neighboring points on the medial axis; and (iii) a junction point, if it has more than two neighboring medial axis points. The relational graph of medial axis segments is then computed (Figure 2.1E). Nodes are embedded at the locations of the termination and junction points of the medial axis, and edges connect the nodes wherever a single medial axis segment connects termination and/or junction points. To consider parallel edges, which have the same start and end nodes in the graph, we add one node to the relational graph, representing paths from one junction or termination point of the medial axis to the next junction or termination point. The medial axis contains information about the curvature of root hair segments, and the relational graph illustrates the neighborhood topology of adjacent segments.

Rules to fit valid splines select root hair candidates as a combination of root hair segments

Based on the medial axis and the relational graph, it is possible to create a root hair candidate. This candidate is created by traversing a path along the relational graph from one node to another node and by fitting a smooth line to this path (Figure 2.1F, G). Traversing paths between alternative pairs of nodes and alternative paths between the same pair of nodes results in additional root hair candidates (Figure 2.1H). To limit the number of candidates, only nodes within reasonable proximity are used as pairs (Supplementary Protocol S5). For all paths, we use a weighted spline fitting method to create smooth lines, which remove medial axis artifacts at junctions to represent root hairs more accurately (Supplementary Protocol S6). We accomplish this task by weighting the spline at a location using the equation:

$$w = 1/\max\,(0.5, 0.5 + r_{MA} - r_{min}) \qquad \text{(Eq. 1)}$$

in which r_{MA} is the measured radius of the medial circle, r_{min} is the interpolated value between local minima of the measured radius along the medial axis, and 0.5 accounts for noise in the raster-based medial axis. The weights of individual spline points are increased iteratively until all points are between the root hair edge and the medial axis. As a result, spline sections at junctions with high radii are smoothed more than at thinner locations of the medial axis.

To reduce the number of splines further, we remove any invalid ones. We define an invalid spline as one with high curvature at junction points. We compute the total curvature for each spline and the segment curvatures for individual segments between adjacent nodes of the spline. Total and segment curvatures are defined as the integral of the spline curvature along its entire length and segment length, respectively (Supplementary Protocol S7). At each segment, we additionally determine a reference value as the smallest possible segment curvature at this segment based on the segment curvatures of all splines overlapping with this segment. We then compare the total curvature of a spline with the sum of the reference values of all its segments. This process enables us to quantify the spline's residual spline curvature to quantify its curviness compared with the optimal case of the lowest possible total curvature. Similarly, we locally compare each individual segment curvature of a spline with its reference value to obtain the residual segment curvature. Since the curviness value is scale-independent, we can define a threshold value of 180° for residual spline curvature and a threshold of 45° for residual segment curvature to remove invalid splines. As a result, only those splines remain that have low curvature at junction points of the medial axis.

Analysing spline relationships reduces combinatorial space

Some of the remaining splines will touch one another or overlap partially. Therefore, we define three relationships between splines and assign one relationship to each pair of splines (Figure 2.2). First, splines that overlap or intersect in an invalid manner result in conflicting relationships (Figure 2.2A; Supplementary Protocol S8). Splines that have a conflict are not allowed to be both parts of the same solution. Second, in all remaining cases, splines either do not touch or they intersect or overlap in a valid manner (Figure 2.2B, C). Third, splines that overlap at exactly one end are merged into one root hair candidate (Figure 2.2D). This categorization enables us to reduce the number of splines and, thus, keep the combinatorial space small.

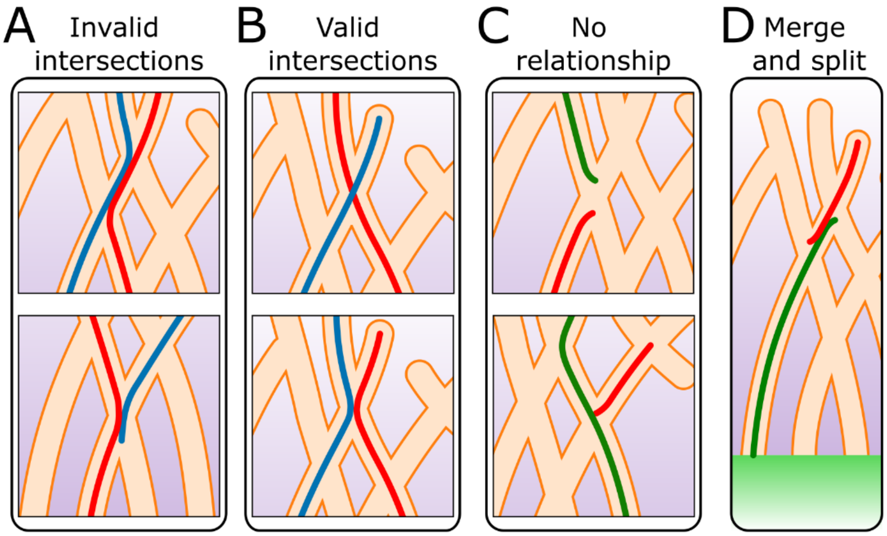

Figure 2.2: Rules established between pairs of splines. (A) Splines must not exist side by side if long internal sections of splines overlap, or if an end section of a spline overlaps with the internal section of another spline. (B, C) Splines can exist side by side if they intersect with large angles, touch slightly, or do not touch. (D) Two splines are treated as single root hairs if only two of their ends overlap. Removing one of the splines splits the root hair.

Combinatorial optimization identifies splines that correspond to root hairs

We use simulated annealing, a combinatorial optimization method, to determine an optimal solution by iteratively exploring various spline configurations that best reconstruct actual root hairs correctly and completely (Kirkpatrick et al., 1983). In our approach, we start with an initial set of randomly selected splines (Figure 2.1I) and iteratively make small changes to this set, by introducing or removing splines. At each iteration, we evaluate the new set of splines with a predefined cost function. If the new spline set has a lower cost, we accept it as the new current state. If the new spline set has a higher cost, we accept it with a probability that decreases as the temperature of the optimization process decreases, a concept defined as the temperature level. This approach allows the algorithm to occasionally accept worse solutions, helping it to avoid getting stuck in local minima and improving the chances of finding the global minimum at the end of the process (Figure 2.1J, K). The process stops once the stopping criterion is met. The parametrization of the simulated annealing process is automated and is based on the description by Orsila et al. (2008) (Supplementary Protocol S9).

Our method is based on solving a 0-1 integer problem with restored feasibility at each move (Abramson et al., 1996). This means that the initial set of randomly selected splines and all subsequent iterations must be feasible (i.e. all relationships between splines are valid). If a newly added spline violates the relationships shown in Figure 2.2A, then conflicting splines are removed to reestablish the validity of the current state of the spline set. Similarly, splines are merged or split when necessary. This method ensures that all intersecting root hairs are resolved correctly.

DIRT/μ quantifies the cost of a state of the spline set (i.e., how good it is) as a function of three parameters (Supplementary Figure S1; Table 2.1).

1. Minimum distance to root, D_{root}: we minimize the distances between each root hair candidate and the root in a least squares sense to minimize outliers at large distances to the root.

2. Residual total curvature, $K_{residual}$: we minimize the residual spline curvature of all candidates in a least squares sense to avoid candidates with excessive curvature.
3. Incompleteness, $R_{incomplete}$: we minimize the ratio between the length of all unresolved medial axis segments ($l_{unresolved\ MA}$) and the total length of the medial axis (l_{MA}) to quantify the degree of identified root hairs.

Table 2.1: Overview of optimization metrics. The table contains the calculation for the minimum distance to root, residual total curvature, and incompleteness, as well as their normalized values and explanations. The total cost is the weighted root-mean-square value of their normalized values.

	Values	Normalized values	Explanations
Minimum distance to root	$\mathrm{D_{root}} = \sqrt{\frac{1}{\mathrm{n}}\sum_{\mathrm{i=1}}^{\mathrm{n}} \mathrm{d_i^2}}$	$\widetilde{\mathrm{D}}_{\mathrm{root}} = \frac{\mathrm{D_{root}} - 1}{\mathrm{D_{max}} - 1}$	n is number of candidates; d_i is distance of candidate i to root in pixels; D_{max} is average length of all medial axis segments that connect to root.
Residual total curvature	$\mathrm{K_{residual}} = \sqrt{\frac{1}{\mathrm{n}}\sum_{\mathrm{i=1}}^{\mathrm{n}} \kappa_{\mathrm{i}}^2}$	$\widetilde{\mathrm{K}}_{\mathrm{residual}} = \frac{\mathrm{K_{residual}}}{\mathrm{K_{max}}}$	n is number of candidates; κ_i is residual spline curvature of candidate i; K_{max} is average of all residual total curvatures.
Incompleteness	$\mathrm{R_{incomplete}} = 1 - \frac{\mathrm{l_{unresolved\ MA}}}{\mathrm{l_{MA}}}$	$\widetilde{\mathrm{R}}_{\mathrm{incomplete}} = \mathrm{R_{incomplete}}$	l_{MA} is length of all medial axis segments; $l_{unresolved\ MA}$ is the length of medial axis segments that are unresolved.
Total cost	$\mathrm{cost} = \sqrt{\mathrm{w_1}\widetilde{\mathrm{D}}_{\mathrm{root}}^2 + \mathrm{w_2}\widetilde{\mathrm{K}}_{\mathrm{resisual}}^2 + \mathrm{w_3}\widetilde{\mathrm{R}}_{\mathrm{incomplete}}^2}\,, \sum_{\mathrm{k=1}}^{3} \mathrm{w_k} = 1$		w_1, w_2, and w_3 are user specified weights (for sensitivity analysis of weights, see Supplementary Figures S8, S9).

The total cost of the state of the spline set is computed as the weighted root-mean-square of all three metrics to balance their minimization. In conjunction with the three types of relationships between splines, the combinatorial optimization enables us to minimize the total cost and, thus, resolve intersecting root hairs in a computationally efficient manner. As a result, not all splines will perfectly fit the criteria, but the number of incorrectly identified root hairs is minimized, enabling the statistical evaluation of individual root hair measurements. Therefore, we use the state with the lowest total cost as our solution.

Root hair traits are measured relative to identified root hair splines

Given the identified root hairs in the state with the lowest total cost, we measure the lengths of all root hairs and the number of root hairs. We distinguish between root hairs on the main root (i.e. the root with largest diameter) and on thinner secondary roots emerging from the main root. Based on the length of the top and bottom edges of the main root and the number of root hairs, we determine RHD across the entire root, the densities on the top and bottom edges, the highest density in a 1 mm section, and the variation of density along the root. Further parameters can be derived from splines that represent root hairs; for example, parameters based on the curvature of the spline, which quantifies the rate of change in direction of the longitudinal axis of the root hair, such as the integral of absolute curvature along its length, average curvature, and maximum curvature.

Three test cases demonstrate the accuracy, precision, and reliability of DIRT/µ

We used root hair images from three experiments to demonstrate the feasibility of DIRT/µ and its benefits over manual root hair measurements (Table 2; Supplementary Protocols S10-S12). Dataset Mahidol I consists of 15 selected images of rice (*Oryza sativa*), maize (*Zea mays*), and common bean (*Phaseolus vulgaris*) roots and serves as a high-quality validation set. In this set, the images were chosen to represent the phenotypic variation, ranging from low to high RHDs, as well as short to long root hairs per species. We performed image classification in ilastik on each image individually due to differences in magnification between the images and to decouple the effects of the classification from root hair extraction. In all 15 images, we manually traced all visible root hairs and registered their lengths for comparison with the automatic measurements in ImageJ. Dataset Mahidol II, which is similar in experimental set-up to dataset Mahidol I, serves as a demonstration set with low-quality reference measurements. A total of 731 images were taken from rice, maize, and common bean roots, with three genotypes for each species, three to four samples per genotype, and in most samples between four and six images taken along the root. A total of 46 images, in which more than 50% of the root length was mislabeled as lateral root (e.g. due to being images not taken according to DIRT/μ protocol or due to the incorrect classification of pixels), were excluded after visual inspection. In contrast to the first dataset, we manually measured the length of only five representative root hairs and density along a representative section (approx. 1 mm) of the root. Dataset University of Nebraska-Lincoln (UNL), differing from the other datasets regarding experimental set-up and image acquisition, is a subset of a large dataset in which monochrome extended depth of field (EDF) images and validation data are available. We therefore utilized this dataset to test our algorithm on a different type of data, specifically using sorghum (*Sorghum bicolor*) under both well-watered and drought-stressed conditions. Additionally, we used this dataset as a medium-quality validation set, acknowledging that it lacked manual measurement for all root hairs in images containing more than 10 root hairs. After removing outliers through visual inspection (30 images) and excluding additional images in which fewer than two root hairs were detected or manually measured (97 images), 359 images were available for statistical evaluation.

Table 2.2: Summary of datasets used to evaluate the trait measurements of DIRT/μ. EDF, extended depth of field; NA, not available; RGB, red, green, blue.

	Dataset Mahidol I	Dataset Mahidol II	Dataset UNL
Number of images (images not analyzed)	15 (0)	685 (46)	359 (127)
Species (no. of genotypes, no. of plants per genotype, no. of images per plant)	Rice (1,5,1), Maize (1,5,1), Common bean (1,5,1)	Rice (3, 4, 5–6), Maize (3, 3–4, 1–7), Common bean (3, 3–4, 4–7)	Sorghum: 32 genotypes in drought, 31 genotypes in well-watered
Treatments	Control, -N, -P, -K	Control, -N, -P, -K	Well-watered, drought
Manual measurements	All root hairs	Length: five representative root hairs Density: representative section (approx. 1mm)	All root hairs and up to 10 or 20 in some images
Microscope	Olympus MVX10	Olympus MVX10	Leica MZ10 F
Color space	RGB	RGB	Gray/monochrome
Staining	Toluidine blue	Toluidine blue	Trypan blue
EDF	No	No	Yes
Resolution in μm/pixel	0.34–1.34	Rice: 0.67, maize: 1.34–1.72, common bean: 1.08	NA
Training set/classification	By individual image	Batch by genotype	Batch
Number of iterations	1000	1000	1000

Using the Mahidol I data, we tested the optimization parameters number of temperature levels (see Supplementary Protocol S9 for definition) and weights of individual cost criteria (w1, w2, and w3) for their sensitivity and to determine their optimal values. We processed all 15 images and calculated the resulting mean RHL ($\mathrm{RHL}_{\mathrm{mean}}$), maximum RHL ($\mathrm{RHL}_{\mathrm{max}}$), and standard deviation of RHL ($\mathrm{RHL}_{\mathrm{std}}$), as well as root hair number ($\mathrm{RH}_{\mathrm{num}}$) for a range of both optimization parameters. To determine the optimal number of temperature levels, we additionally calculated the total cost of the simulated annealing process and computation time. The number of temperature levels ranged between 25 and 10 000 and computations were replicated five times at each value. To test weights, we varied individual weights between 0.02 and 0.96 under the constraint that they sum to 1.0. For each combination of weights, we computed the Pearson correlation coefficient and root-mean-square error (RMSE) of RHL_{mean}, RHL_{max}, RHL_{std}, and RH_{num} between manual and automatic measurements.

Furthermore, we validated the DIRT/µ results using manual measurements of RHL statistics and RH_{num}. RHL statistics and RH_{num} were computed for each individual image in datasets Mahidol I and UNL. For RHL statistics, we computed RHL_{mean}, RHL_{max}, and RHL_{std}. For each individual dataset, we calculated the correlation between the measurements performed manually and those taken with DIRT/µ.

For the Mahidol II data, we compared the traits RHL_{mean}, RHL_{std}, the coefficient of variation of RHL (RHL_{CV}), and RHD between genotypes for the control group. For RHD, we took the quotient of the number of root hairs and the total length of the root edge. We further computed the correlation between measurements performed manually and with DIRT/µ by image in the same manner as for datasets Mahidol I and UNL. For the computation of correlations, 28 images with fewer than two root hairs in either manual or automatic measurements were omitted. For the rice genotype Sungyod, we analysed the effect of treatments on RHL_{mean}, RHL_{std}, RHL_{CV}, and RHD. For the same genotype, we further computed RHL_{mean} and RHD at different levels of organization: (i) separately for the top and bottom root edges per image, (ii) per image, and (iii) per plant sample (i.e. all images along the root axis). Values were obtained by pooling all the identified individual root hairs and root edge lengths at the corresponding level. Thus, we calculated RHL_{mean} for each sample as the mean of root hairs extracted from all images of the corresponding sample. We further calculated the RHD of a sample as the quotient of the number of root hairs in all sample images by the total length of root edges in all sample images. Values at the treatment and genotype level (e.g. RHL_{mean}) were calculated from the results at the plant sample level. To keep all results comparable, we only accounted for root hairs on the primary root and ignored root hairs emerging from thinner secondary lateral roots.

Results

Sensitivity analysis revealed a rapid convergence of DIRT/ μ to optimal results

The sensitivity analysis revealed that, at low numbers of temperature levels, all the measured variables (RHL_{mean}, RHL_{max}, RHL_{std}, RH_{num}, and total cost) diverged only slightly from values at 10 000 temperature levels (Supplementary Figures S2–S6). Although the results suggest a smaller number is sufficient to converge toward a low total cost and to distinguish traits between our samples, we chose to use 1000 temperature levels in our further analysis as a tradeoff to reduce computational time (Supplementary Figure S7) and to increase precision. Furthermore, varying the weights of individual cost criteria revealed the correlation between manual and automatic measurements of RHL_{mean} and RH_{num} was consistently high ($r^2=0.88-0.96$ and $r^2=0.61-0.71$, respectively) for all combinations of weights, but it was still highest for balanced weights (Supplementary Figure S8). Measurements of RMSE ranged between 44 and 94.7 µm for RHL_{mean} and between 40.6 and 52 root hairs for RH_{num} (Supplementary Figure S9). Both measurements, however, were lowest for low weights of the curvature metric and highest for low weights of the incompleteness metric. As a result, we used equal values for all weights for all further analysis.

Correlation analysis validates DIRT/µ and quantifies shortcomings in manual measurement methods

The distributions of manually and automatically measured RHLs in dataset Mahidol I displayed a good resemblance to each other (Figure 2.3A) and correlations between the validation data and automatic measurements of root hair traits were high in datasets Mahidol I (Figure 2.3B) and UNL (Figure 2.3C). With 1000 temperature levels and balanced weights, $\mathrm{RHL}_{\mathrm{mean}}$ correlated very strongly between manual and automatic measurements in dataset Mahidol I ($r^2=0.95$, $P<0.001$) and strongly in dataset UNL ($r^2=0.73$, $P<0.001$) but was slightly biased and underestimated with slopes of 0.66 and 0.55, respectively. For $\mathrm{RHL}_{\mathrm{max}}$, we obtained even stronger correlations in dataset Mahidol I ($r^2=0.97$, $P<0.001$) but the same correlation in dataset UNL ($r^2=0.73$, $P<0.001$). Both distributions had slopes very close to 1 (1.02 and 0.97). The correlation in $\mathrm{RHL}_{\mathrm{std}}$ was strong in dataset Mahidol I ($r^2=0.95$, $P<0.001$) but only moderate in dataset UNL ($r^2=0.59$, $P<0.001$), with slopes of 0.98 and 0.83, respectively. The performance regarding $\mathrm{RH}_{\mathrm{num}}$ was weaker than for the RHL statistics, with strong correlations in dataset Mahidol I ($r^2=0.69$, $P<0.001$) and moderate correlations in dataset UNL ($r^2=0.44$, $P<0.001$). The algorithm appeared to undercount the number of root hairs at higher densities [see outlier in the right graph of Figure 2.3B corresponding to Bean 1 (short-dense)], and thus underestimated the number of root hairs at such densities.

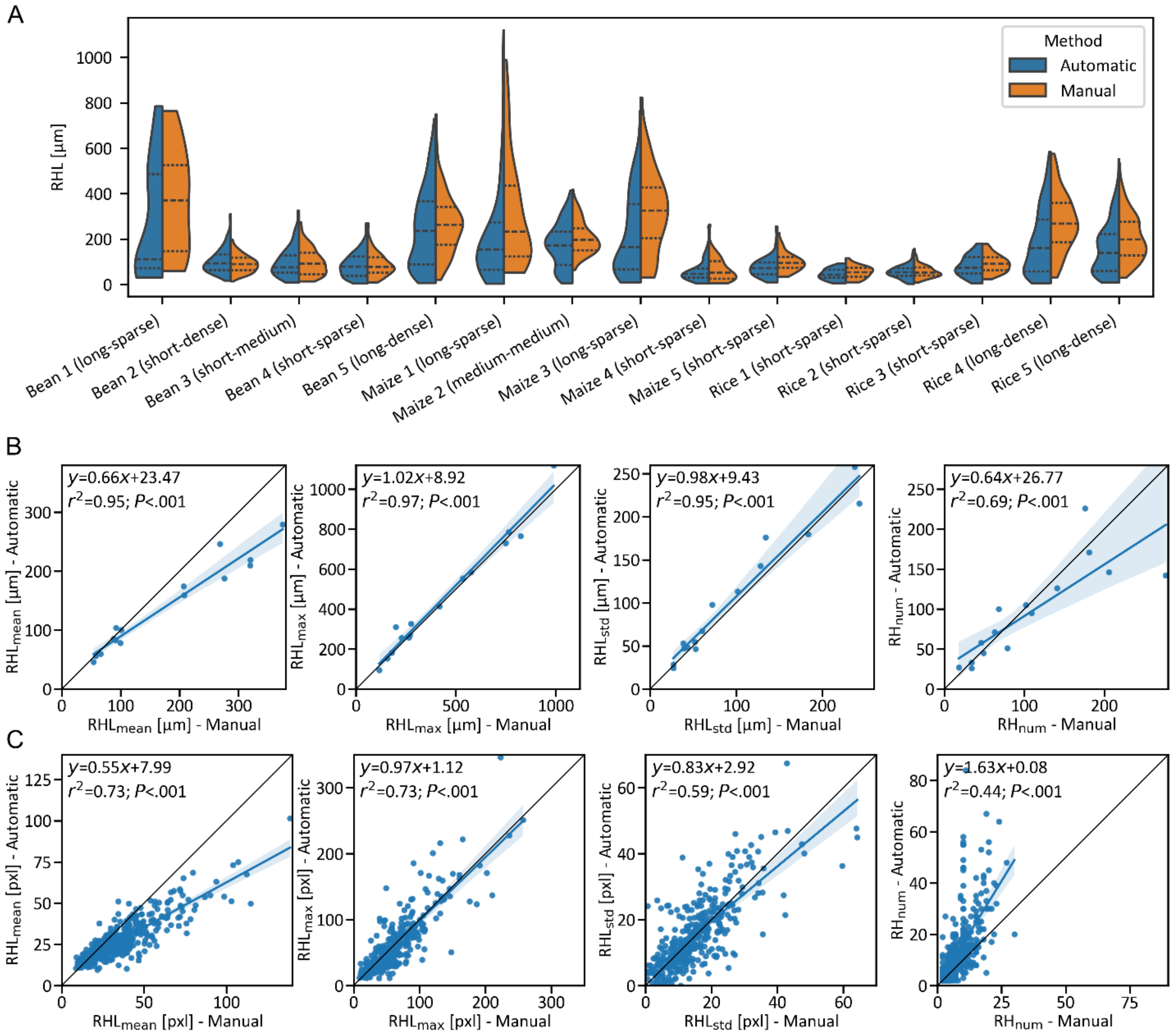

Figure 2.3: Validation of root hair measurements from automatic detection. (A) Distributions of length of all root hairs in individual images in dataset Mahidol I from our method (blue) and manual measurements (orange). The dashed center lines represent the median of the distribution and the dotted lines the quartiles. Each pair of automatic and manual distributions corresponds to one image. The names on the horizontal axis refer to their species and a description for root hair length and density in parentheses. (B) Correlations of RHL_{mean}, RHL_{max}, RHL_{std}, and RH_{num} in dataset Mahidol I between our method (vertical axis) and manual measurements (horizontal axis). (C) Correlations of RHL_{mean}, RHL_{max}, RHL_{std}, and RH_{num} in dataset UNL between our method (vertical axis) and manual measurements (horizontal axis). pxl, pixels; RHL_{mean}, mean root hair length; RHL_{max}, maximum root hair length; RHL_{std}, standard deviation of root hair length; RH_{num}, root hair number.

The measurements of RHL_{mean} in the control group of dataset Mahidol II indicated the shortest root hairs were in rice (KDML105: 90.7 µm; Phitsanulok 2: 84.8 µm; Sungyod: 71.3 µm), followed by common bean (DOR364: 196.0 µm; L8857: 223.8 µm; SEQ7: 234.4 µm), while maize had the longest root hairs (Takfa 1: 316.8 µm; Takfa 2: 366.4 µm; Takfa 3: 450.3 µm; Figure 2.4A), which agreed with our expectations and manual measurements. We observed the same pattern in RHL_{std} within individual plants (Supplementary Figure S10A). Using the coefficient of variation RHL_{CV}, we decoupled the variation in RHL from its absolute value, revealing the smallest values in RHL_{CV} for DOR364 (0.62) and SEQ7 (0.66) and the largest value for Takfa 3 (0.83; Supplementary Figure S10B). Visual inspection of these genotypes confirmed that beans generally had more uniform RHLs, and Takfa 3 had the most variation. We further observed the highest RHD in the rice genotypes KDML105 (34.04 mm^{-1}) and Phitsanulok 2 (31.02 mm^{-1}) and the smallest RHD in Takfa 1 (15.16 mm^{-1}; Supplementary Figure S10C).

In dataset Mahidol II, we compared the traits measured with DIRT/µ with those measured manually in individual images and grouped by genotype. In this dataset manual measurements of RHL were taken only from five root hairs and manual measurements of RHD were taken along a small section of the root. Automatic measurements of RHL_{mean} correlated well with the manual measurements within all nine genotypes (from r^2=0.53 to r^2=0.86; Figure 2.4B). The slopes of fitted regression lines were closest to 1 in the bean genotypes (0.67-0.79), and lowest for rice (0.22 to 0.40) and maize (0.39−0.44) genotypes. Correlations in RHL_{std} were the lowest, with values between r^2=0.13 for DOR364 and r^2=0.54 for Sungyod (Supplementary Figure S11). Nearly all the RHL_{std} values were higher in the automatic measurements than in the manual measurements. Correlations for the RHL_{max} range from r^2=0.21 for DOR364 to r^2=0.76 for Phitsanulok 2 (Supplementary Figure S12). Manual and automatic measurements of RHD correlated slightly weaker than measurements of RHL, ranging between r^2=0.21 and r^2=0.67, with bean genotypes and Takfa 2 having the lowest correlations (Supplementary Figure S13). Our measurements of RHD were lower than the manual measurements in bean (slope 0.21−0.51) and maize (slope 0.34−0.61) but higher in rice (slope 1.15–1.42).

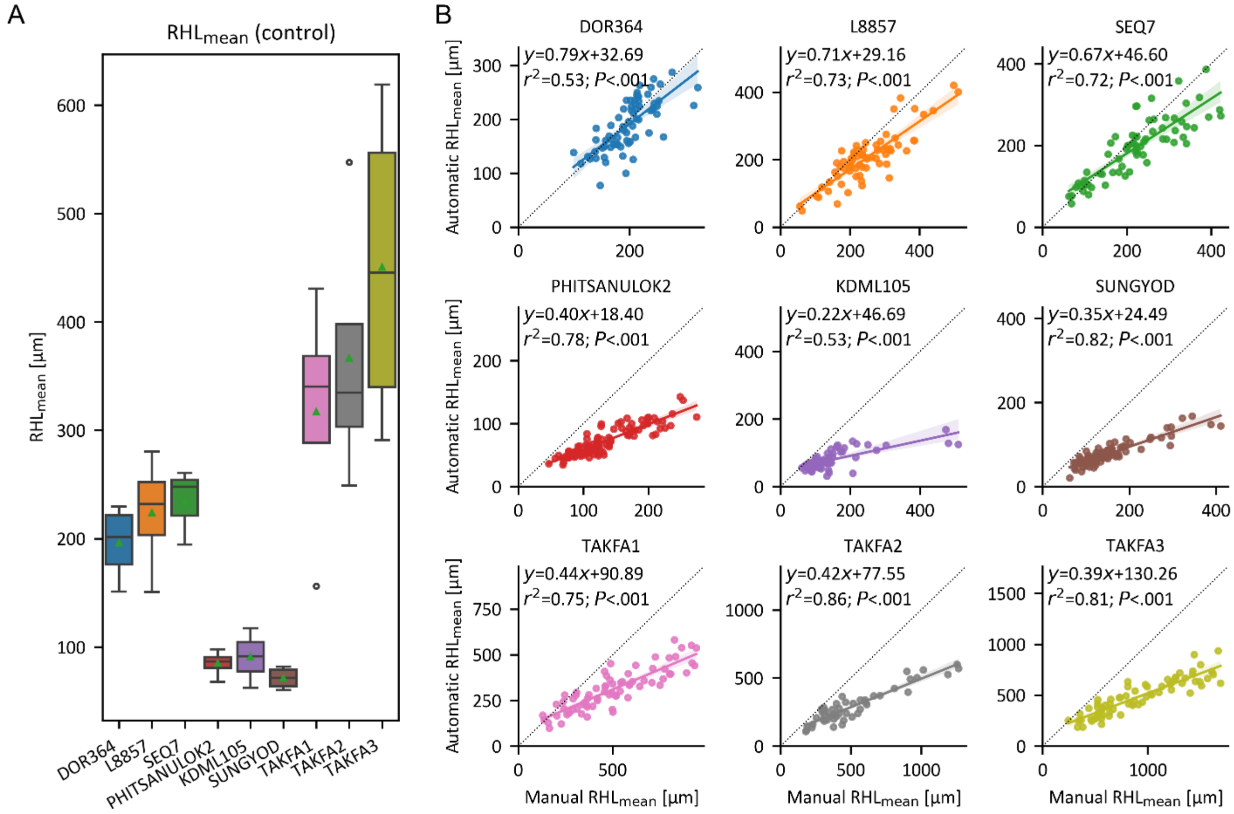

Figure 2.4: Measurements of mean root hair length (RHL_{mean}) in dataset Mahidol II. (A) Distribution of RHL_{mean} in the control group illustrated by genotype. RHL_{mean} was computed for individual plants. The box displays the quartiles of the distribution, the middle horizontal line represents the median, and the whiskers extend to 1.5 times the interquartile range from the lower and upper quartiles. Outliers outside the whiskers are represented as circles. The mean of the distribution is displayed as a green triangle. (B) Correlation for automatic and manual measurements of RHL_{mean}. Each plot includes the results of a single genotype. Each circle represents the RHL_{mean} per image. The lines represent the linear regression models with 95% confidence intervals. The horizontal and vertical axes are drawn at the same scale per panel. The dotted line represents the 1–1 line.

We further illustrate root hair trait measurements in the example of Sungyod (Figure 2.5). Root hairs under phosphorus stress were 25.82 µm longer than root hairs in the control group, but despite the large difference, it was not significant (P=0.103) (Figure 2.5A). Results for RHL_{std} were higher in the reduced phosphorus group than in the control (P=0.028) (Figure 2.5B). The RHL_{CV} under reduced nitrogen and reduced phosphorus was higher than in the control group, but the difference was not significant (P=0.063 and P=0.138) (Figure 2.5C). The RHD under reduced phosphorus was 15.86 root hairs mm^{-1} higher than in the control group (P=0.013) (Figure 2.5D). The measurements using DIRT/µ resulted in the full distribution of RHL, revealing an overall pattern and small nuances, such as skewness, kurtosis, or the proportions of smaller and longer root hairs, at the plant level (Figure 2.5E) or the individual image level (Figure 2.5F). There can be differences not only between treatments but also along the root axis of a single root (Figure 2.5F). In general, we frequently observed differences with a factor larger than 2 for RHL_{mean} and RHD at all levels of observation. For example, large differences occurred between the lower and upper edges of the root in a single image, between images along the root axis, and between individual samples (Figure 2.5G, H).

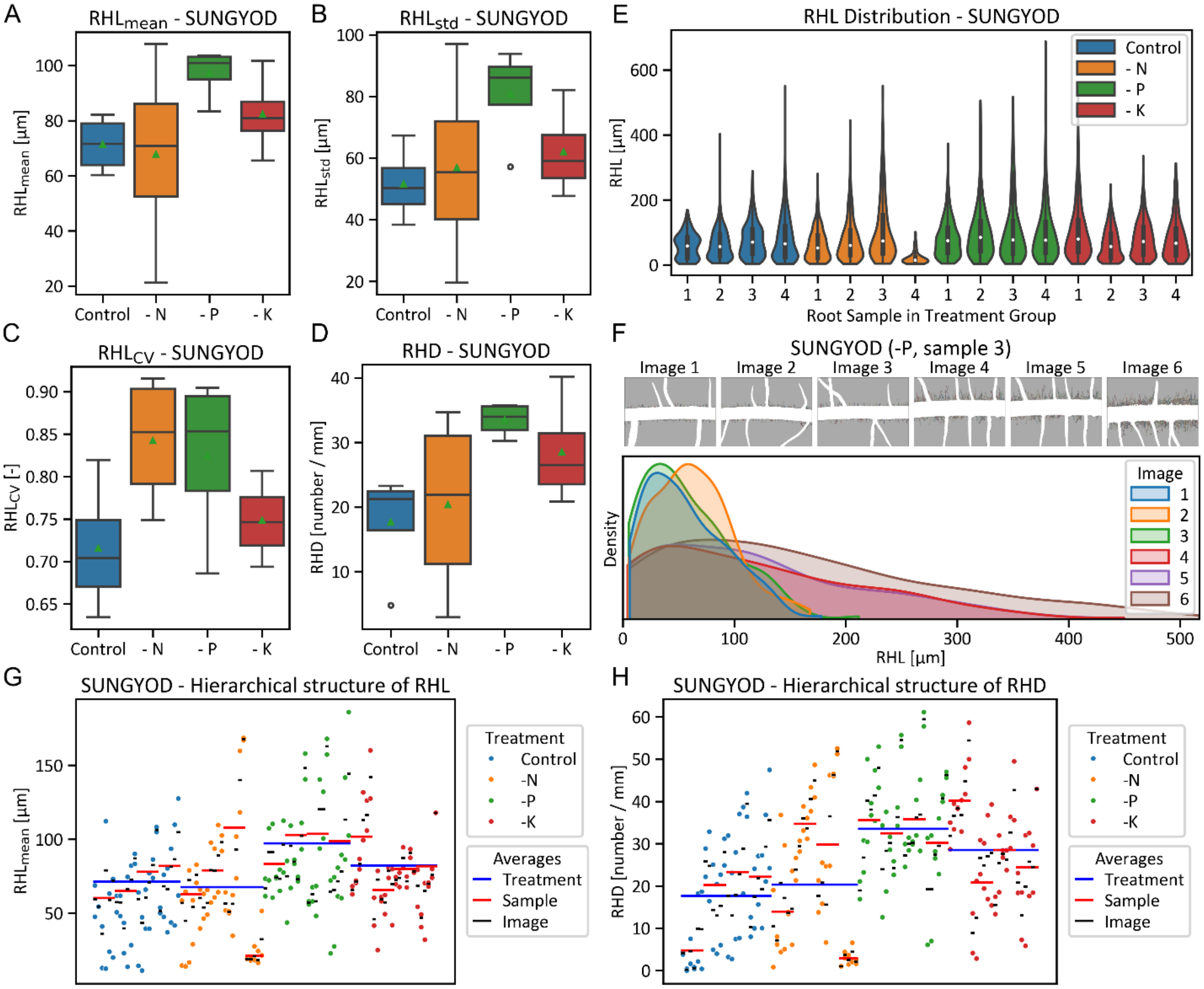

Figure 2.5: Analysis of rice genotype Sungyod in dataset Mahidol II. (A–D) $\mathrm{RHL}_{\mathrm{mean}}$ (A), $\mathrm{RHL}_{\mathrm{std}}$ (B), $\mathrm{RHL}_{\mathrm{CV}}$ (C), and RHD (D) were measured for all individual plants in the control, reduced nitrogen, reduced phosphorus, and reduced potassium groups. The box displays the quartiles of the distribution, the middle horizontal line represents the median, and the whiskers extend to 1.5 times the interquartile range from the lower and upper quartiles. Outliers outside the whiskers are represented as circles. The mean of the distribution is displayed as a green triangle. (E) Distributions of length of all root hairs in individual plants colored by treatment group. The white circle represents the median of the distribution, the black bar displays the quartiles, and the thin black centerline extends to 1.5 times the interquartile range from the lower and upper quartiles. (F) Distributions of length of all root hairs in all six individual images of sample 3 under phosphorus stress. (G–H) Overview of $\mathrm{RHL}_{\mathrm{mean}}$ (G) and RHD (H) measured at different levels of observation. The colored dots represent the measurements taken on one side of the root in a single image. A pair of colored dots aligned vertically represents one image. The corresponding black horizontal bar illustrates the measurement taken at the whole image level. Red horizontal bars represent the measurement taken from all images corresponding to a single plant. Blue horizontal lines display the mean value of all plants in each treatment group. RHD, root hair density; RHL, root hair length; $\mathrm{RHL}_{\mathrm{CV}}$, coefficient of variation of root hair length; $\mathrm{RHL}_{\mathrm{mean}}$, mean root hair length; $\mathrm{RHL}_{\mathrm{std}}$, standard deviation of root hair length.

The degree of occlusions drives the computation time of DIRT/μ

The computation time of our method is driven by the number of junction points on the initially extracted medial axis. For dataset Mahidol II, the computation time varied between 67 s for KDML105-p1-1 with 24 nodes and 112.9 h for TAKFA3-p2-6, which had 8692 nodes. The computation time for all 685 images of dataset Mahidol II was 3408.6 h. Combinatorial optimization accounted for most of the overall processing time (82.5%), followed by determining candidate root hairs (16.8%). Computational time increased linearly for images with more than 200 junctions in the medial axis (Supplementary Figure S14), was shortest for rice images, and was longest for maize images (Supplementary Figure S15).

Discussion

DIRT/μ eliminates user bias from root hair measurements and enables biological discovery by introducing previously inaccessible traits

Resolving intersections of root hairs in digital microscopy images enabled us to measure root hair traits that could not previously be automatically measured (Le Marie et al., 2014). By extracting individual root hairs (Figure 2.6), we determined the distribution of RHL in each image, with parameters such as its mean, maximum, standard deviation, and coefficient of variation, as well as RHD with high accuracy and precision. Comparison of traits measured with DIRT/μ to their manual measurements showed good correspondence in two independent datasets (Figure 2.3). However, in dataset Mahidol I (Figure 2.3B) we observed higher correlations and slopes closer to 1 than in dataset UNL (Figure 2.3C). We believe that this is caused by the lower quality of the manual measurements in dataset UNL, where not all root hairs were recorded in images with high RHD and which had a lower number of root hairs compared with dataset Mahidol I. Overall, our validation based on two datasets proves DIRT/μ can be used as a reliable tool to measure root traits from microscopy images.

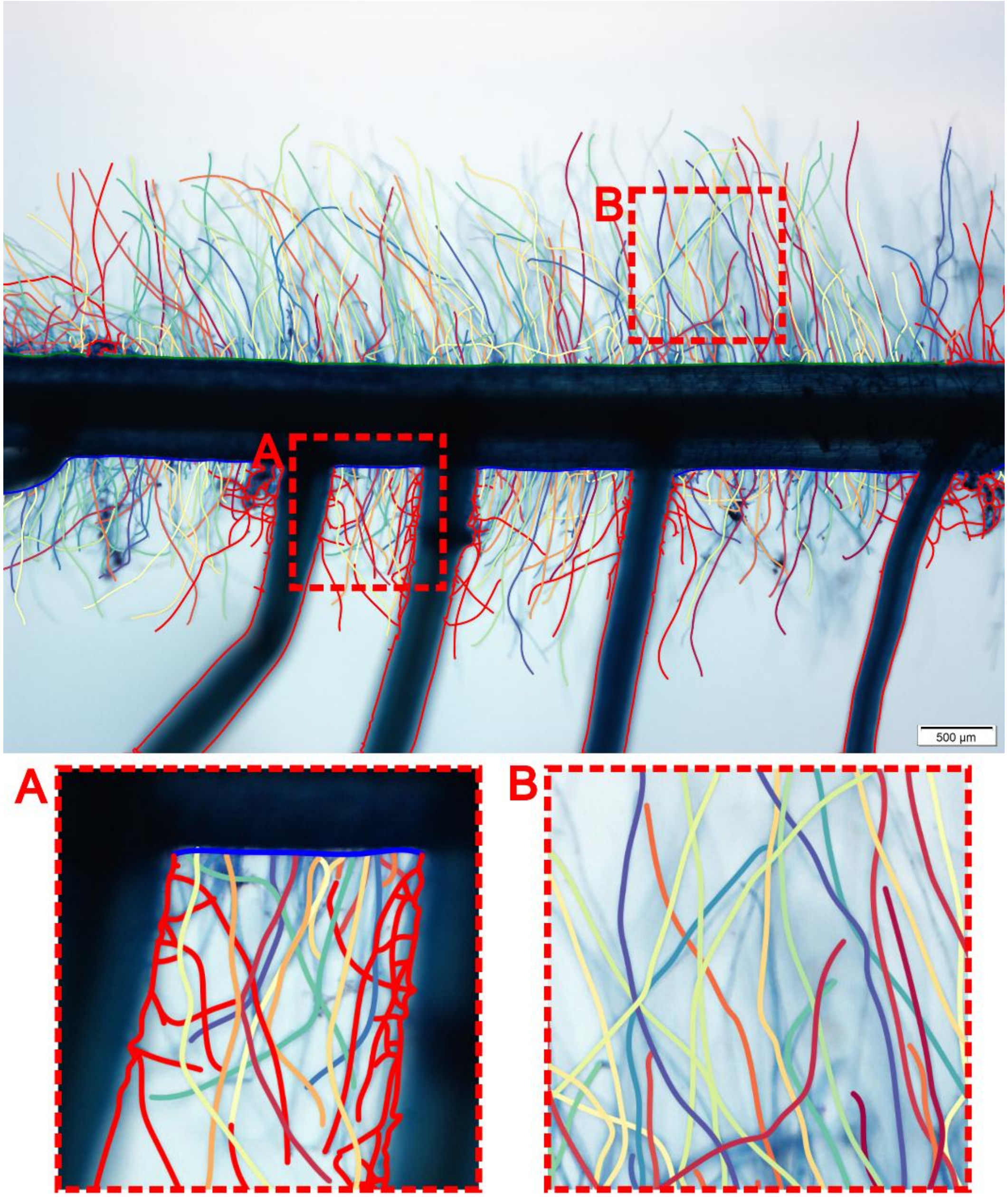

Figure 2.6: Original microscopy image of root TAKFA3-n3-1 with extracted root hairs. Valid root hairs growing on main root are plotted as lines in random colors, while root hairs on lateral roots are plotted in red. The top and bottom edges of the root are plotted in green and blue, respectively and the edges of lateral roots are plotted in red. Boxes A and B show zoom-in views of extracted root hairs.

The traits measured with DIRT/μ cannot be measured manually in a feasible time because of the often long and dense root hair arrangements. Assuming a measurement time of 10 s per root hair, it would require more than 330 h to track manually all 119 785 root hairs that were measured automatically using DIRT/μ in dataset Mahidol II. As such, a sub-sample of root hairs is often extracted manually to determine mean RHL and RHD, as was done in dataset Mahidol II. Manual measurements based on a small fraction of root hairs can, however, result in biased (i.e. often longer and denser) root hair traits (Figure 2.4B; Supplementary Figure S15) and cannot detect the distribution of RHL (Supplementary Figure S13). In the example of the rice genotype KDML105, we observed a fitted regression line with a slope of 0.22, and thus an almost 5-fold smaller $\mathrm{RHL}_{\mathrm{mean}}$ than measured with our method. We observed lower correlations and correspondences with slopes deviating strongly from 1 across the nine genotypes and the measured traits (Figure 2.4B and Supplementary Figures S13-S15). We demonstrated that results computed with our method correspond better to manual measurements when all root hairs (i.e., Datasets Mahidol I and UNL), rather than a subset (i.e., Dataset Mahidol II), are measured, suggesting that we eliminate bias compared to state-of-the-art manual scoring methods that only take a visually determined subset of root hairs into account.

By extracting individual root hairs, our method also overcomes the limitations of previous computational methods, which were limited to determining either root hair pixel area, root hair profile, or total RHL along a section of the root (Guichard et al., 2019; Lu et al., 2022; Vincent et al., 2017). From our experience, DIRT/μ is not completely robust to lower quality images or noise resulting from dirt, mycorrhizae, or damaged root hairs, which can result in misclassifications during the initial process. Images with clean root hairs and high contrast between root hairs and background consistently provided the best results. As such, we recommend staining root hairs and using a red, green, blue (RGB) camera to capture images. Even though DIRT/μ can resolve a high number of intersections between root hairs, it cannot distinguish root hair with complete overlap. Further, we observed that using a small focal depth minimized the remaining effects of the 2D projection on RHL and RHD measurements. When adhering to these recommendations, automatic extraction of individual root hairs from microscopy images with DIRT/μ has the potential for new biological discoveries in the plant sciences.

DIRT/μ is an open-source solution to automated high-throughput phenotyping of root hairs

Automating the process of individual root hair extraction increases the throughput of phenotyping root traits, resulting in quicker analysis. Our measurements found a high amount of variation in root hair traits within individual plants and between plants within the same experimental groups (Figure 2.5). DIRT/μ can address this variation by increasing the number of images taken along the root and by increasing the number of samples. The higher throughput at different sampling levels and precision can improve statistical inferences in root hair research (Blainey et al., 2014; Krzywinski et al., 2014; Lane & Murray, 2021). We note, however, that our pipeline is not fully automated, because obtaining the image classification as an input with ilastik requires human input. Nonetheless, data-specific training sets enable a diverse pool of experimental and technical set-ups, such as different microscopes and magnifications. Ilastik provides a simple interface, so anybody can learn to create a training set and classify a large set of microscopy images in batch processing on personal computers in a feasible time. However, unsupervised classification is an evolving field of research that promises to resolve manual training-set generation (Soltis et al., 2020). Further processing of classified images cannot be performed on personal computers and relies on high-performance computing due to the great combinatorial complexity of resolving intersecting root hairs. Outsourcing this step to high-performance computing through PlantIT (Bonelli et al., 2022) therefore enables large-scale screening of root hairs for users without a technical background.

DIRT/μ provides high-quality and affordable root hair phenotyping with good availability, accessibility, and applicability for all research labs around the world. PlantIT and CyVerse are easily accessible to researchers without any programming knowledge (Swetnam et al., 2023). Online workshops to learn about recommended experimental set-ups and the use of DIRT/μ are available for end users for training through PhenomeForce (Pietrzyk & Saengwilai, 2022).

DIRT/μ is an algorithmic basis that extends to many biological applications

Although we developed DIRT/μ primarily for, and tested it on, microscopy images, we believe it works on images taken in situ with mini- and micro-rhizotrons. Measurements of plant morphology across scales have great potential in plant sciences (Bucksch et al., 2017; Chitwood & Topp, 2015). DIRT/μ has the potential to phenotype any hair-like structure, such as trichomes in plants, antennae or hairs in insects, or cilia in the lungs. The main principles of the DIRT/μ algorithm (i.e. combinatorial rules, cost function, and combinatorial optimization) are dimension-free, such that measurements could be extended to 3D by fitting splines to an underlying 3D skeleton. Our algorithm was developed to extract microscopic, hair-like structures; however, modification of the combinatorial rules and cost function to resolve intersecting branches while preserving branching orders means it can be adapted to identify individual branches in higher-level branching structures, such as roots, leaves, and trees. Therefore, DIRT/μ can result in more rigorous phenotyping.

Declarations

Acknowledgements

We thank Wesley Bonelli for creating a Docker container and integrating DIRT/μ into PlantIT and Benjamin Smith for sharing his macro to preprocess the UNL dataset. The work was conducted while transitioning institutions for AB (University of Georgia to University of Arizona) and ML (University of Nebraska to University of Missouri).

Author contributions

PP, PJS, and AB: conceptualization; PP and AB: methodology; PP and AB: software; PP and AB: validation; PP: formal analysis; PP, NP-U, CC, LP, ML, and PJS: investigation; AB, ML, and PJS: resources; PP: data curation; PP and AB: writing—original draft; PP, NP-U, CC, LP, AR, ML, PJS, and AB: writing—review and editing; PP: visualization; AB: supervision; AB: funding acquisition.

Conflict of interest

The authors declare they have no conflicts of interest.

Funding

The research was supported by the NSF CAREER Award No. 2329282 and an iPlant/CyVerse Seed Grant 'High-throughput Computing Platform for Quantifying Root Traits from Images' to AB and by NSF Award No. 2425989 to ML. Any opinions, findings, and conclusions or recommendations expressed in this material are those of the author(s) and do not necessarily reflect the views of the National Science Foundation.

Data availability

The DIRT/μ algorithm is available at https://zenodo.org/doi/10.5281/zenodo.13614443 (doi: 10.5281/zenodo.13614444). All data used in this manuscript are available as part of the

Supplementary data or published in Figshare (doi: 10.6084/m9.figshare.24886500.v2; (Bucksch et al., 2024)).

References

Abramson, D., Dang, H., & Krishnamoorthy, M. (1996). A comparison of two methods for solving 0–1 integer programs using a general purpose simulated annealing algorithm. *Annals of Operations Research*, *63*(1), 129-150. https://doi.org/10.1007/bf02601642

Baumberger, N., Steiner, M., Ryser, U., Keller, B., & Ringli, C. (2003). Synergistic interaction of the two paralogous Arabidopsis genes LRX1 and LRX2 in cell wall formation during root hair development. *Plant Journal*, *35*(1), 71-81. https://doi.org/10.1046/j.1365-313X.2003.01784.x

Berg, S., Kutra, D., Kroeger, T., Straehle, C. N., Kausler, B. X., Haubold, C., Schiegg, M., Ales, J., Beier, T., Rudy, M., Eren, K., Cervantes, J. I., Xu, B., Beuttenmueller, F., Wolny, A., Zhang, C., Koethe, U., Hamprecht, F. A., & Kreshuk, A. (2019). ilastik: interactive machine learning for (bio)image analysis. *Nature Methods*, *16*(12), 1226-1232. https://doi.org/10.1038/s41592-019-0582-9

Bibikova, T. N., Jacob, T., Dahse, I., & Gilroy, S. (1998). Localized changes in apoplastic and cytoplasmic pH are associated with root hair development in Arabidopsis thaliana. *Development*, *125*(15), 2925-2934. https://doi.org/10.1242/dev.125.15.2925

Blainey, P., Krzywinski, M., & Altman, N. (2014). Replication. *Nature Methods*, *11*(9), 879-880. https://doi.org/10.1038/nmeth.3091

Bonelli, W., Liu, S., Cotter, C., Flory, M., Luck, M., & Bucksch, A. (2022). PlantIT: Containerized phenotyping in the cloud. *NAPPN Annual Conference*. https://doi.org/10.1002/essoar.10508354.1

Brown, L. K., George, T. S., Thompson, J. A., Wright, G., Lyon, J., Dupuy, L., Hubbard, S. F., & White, P. J. (2012). What are the implications of variation in root hair length on tolerance to phosphorus deficiency in combination with water stress in barley (Hordeum vulgare)? *Annals of botany*, *110*(2), 319-328. https://doi.org/10.1093/aob/mcs085

Bucksch, A. (2014). A practical introduction to skeletons for the plant sciences. *Applications in Plant Sciences*, *2*(8), Article 1400005. https://doi.org/10.3732/apps.1400005

Bucksch, A., Atta-Boateng, A., Azihou, A. F., Battogtokh, D., Baumgartner, A., Binder, B. M., Braybrook, S. A., Chang, C., Coneva, V., DeWitt, T. J., Fletcher, A. G., Gehan, M. A., Diaz-Martinez, D. H., Hong, L. L., Iyer-Pascuzzi, A. S., Klein, L. L., Leiboff, S., Li, M., Lynch, J. P., . . . Chitwood, D. H. (2017). Morphological Plant Modeling: Unleashing Geometric and Topological Potential within the Plant Sciences. *Frontiers in Plant Science*, *8*, Article 900. https://doi.org/10.3389/fpls.2017.00900

Bucksch, A., Saengwilai, P., Libault, M., Pingault, L., Pietrzyk, P., Phan-Udom, N., & Chutoe, C. (2024). All Supplement.zip (updated version 2). In: figshare.

Cai, G. C., & Ahmed, M. A. (2022). The role of root hairs in water uptake: recent advances and future perspectives. *Journal of Experimental Botany*, *73*(11), 3330-3338. https://doi.org/10.1093/jxb/erac114

Candeo, A., Doccula, F. G., Valentini, G., Bassi, A., & Costa, A. (2017). Light Sheet Fluorescence Microscopy Quantifies Calcium Oscillations in Root Hairs of Arabidopsis thaliana. *Plant and Cell Physiology*, *58*(7), 1161-1172. https://doi.org/10.1093/pcp/pcx045

Carminati, A., Passioura, J. B., Zarebanadkouki, M., Ahmed, M. A., Ryan, P. R., Watt, M., & Delhaize, E. (2017). Root hairs enable high transpiration rates in drying soils. *New Phytologist*, *216*(3), 771-781. https://doi.org/10.1111/nph.14715

Chitwood, D. H., & Topp, C. N. (2015). Revealing plant cryptotypes: defining meaningful phenotypes among infinite traits. *Current Opinion in Plant Biology*, *24*, 54-60. https://doi.org/10.1016/j.pbi.2015.01.009

Choudhury, S. D., Samal, A., & Awada, T. (2019). Leveraging Image Analysis for High-Throughput Plant Phenotyping. *Frontiers in Plant Science*, *10*, Article 508. https://doi.org/10.3389/fpls.2019.00508

Czarnota, M. A., Paul, R. N., Weston, L. A., & Duke, S. O. (2003). Anatomy of sorgoleone-secreting root hairs of Sorghum species. *International Journal of Plant Sciences*, *164*(6), 861-866. https://doi.org/10.1086/378661

Daly, K. R., Keyes, S. D., Masum, S., & Roose, T. (2016). Image-based modelling of nutrient movement in and around the rhizosphere. *Journal of Experimental Botany*, *67*(4), 1059-1070. https://doi.org/10.1093/jxb/erv544

De Pessemier, J., Moturu, T. R., Nacry, P., Ebert, R., De Gernier, H., Tillard, P., Swarup, K., Wells, D. M., Haseloff, J., Murray, S. C., Bennett, M. J., Inze, D., Vincent, C. I., & Hermans, C. (2022). Root system size and root hair length are key phenes for nitrate acquisition and biomass production across natural variation in Arabidopsis. *Journal of Experimental Botany*, *73*(11), 3569-3583. https://doi.org/10.1093/jxb/erac118

Guichard, M., Allain, J. M., Bianchi, M. W., & Frachisse, J. M. (2019). Root Hair Sizer: an algorithm for high throughput recovery of different root hair and root developmental parameters. *Plant Methods*, *15*(1), Article 104. https://doi.org/10.1186/s13007-019-0483-z

Hanlon, M. T., Vejchasarn, P., Fonta, J. E., Schneider, H. M., McCouch, S. R., & Brown, K. M. (2023). Genome wide association analysis of root hair traits in rice reveals novel genomic regions controlling epidermal cell differentiation. *BMC Plant Biol*, *23*(1), 6, Article 6. https://doi.org/10.1186/s12870-022-04026-5

Houle, D., Govindaraju, D. R., & Omholt, S. (2010). Phenomics: the next challenge. *Nature Reviews Genetics*, *11*(12), 855-866. https://doi.org/10.1038/nrg2897

Jungk, A. (2001). Root hairs and the acquisition of plant nutrients from soil. *Journal of Plant Nutrition and Soil Science*, *164*(2), 121-129.

Keyes, S. D., Zygalakis, K. C., & Roose, T. (2017). An Explicit Structural Model of Root Hair and Soil Interactions Parameterised by Synchrotron X-ray Computed Tomography. *Bulletin of Mathematical Biology*, *79*(12), 2785-2813. https://doi.org/10.1007/s11538-017-0350-x

Kirkpatrick, S., Gelatt, C. D., & Vecchi, M. P. (1983). Optimization by simulated annealing. *Science*, *220*(4598), 671-680. https://doi.org/10.1126/science.220.4598.671

Kohli, P. S., Maurya, K., Thakur, J. K., Bhosale, R., & Giri, J. (2022). Significance of root hairs in developing stress-resilient plants for sustainable crop production. *Plant Cell and Environment*, *45*(3), 677-694. https://doi.org/10.1111/pce.14237

Krzywinski, M., Altman, N., & Blainey, P. (2014). POINTS OF SIGNIFICANCE Nested designs. *Nature Methods*, *11*(10), 977-978. https://doi.org/10.1038/nmeth.3137

Lane, H. M., & Murray, S. C. (2021). High throughput can produce better decisions than high accuracy when phenotyping plant populations. *Crop Science*, *61*(5), 3301-3313. https://doi.org/10.1002/csc2.20514

Le Marie, C., Kirchgessner, N., Marschall, D., Walter, A., & Hund, A. (2014). Rhizoslides: paper-based growth system for non-destructive, high throughput phenotyping of root development by means of image analysis. *Plant Methods*, *10*, Article 13. https://doi.org/10.1186/1746-4811-10-13

Libault, M., Brechenmacher, L., Cheng, J. L., Xu, D., & Stacey, G. (2010). Root hair systems biology [Review]. *Trends in plant science*, *15*(11), 641-650. https://doi.org/10.1016/j.tplants.2010.08.010

Lu, W., Wang, X., & Jia, W. (2022). Root hair image processing based on deep learning and prior knowledge. *Computers and Electronics in Agriculture*, *202*, Article 107397. https://doi.org/10.1016/j.compag.2022.107397

Lürig, M. D., Donoughe, S., Svensson, E. I., Porto, A., & Tsuboi, M. (2021). Computer Vision, Machine Learning, and the Promise of Phenomics in Ecology and Evolutionary Biology. *Frontiers in Ecology and Evolution*, *9*, Article 642774. https://doi.org/10.3389/fevo.2021.642774

Ma, Z., Bielenberg, D. G., Brown, K. M., & Lynch, J. P. (2001). Regulation of root hair density by phosphorus availability in Arabidopsis thaliana. *Plant Cell and Environment*, *24*(4), 459-467. https://doi.org/10.1046/j.1365-3040.2001.00695.x

Ma, Z., Walk, T. C., Marcus, A., & Lynch, J. P. (2001). Morphological synergism in root hair length, density, initiation and geometry for phosphorus acquisition in Arabidopsis thaliana: A modeling approach. *Plant and Soil*, *236*(2), 221-235. https://doi.org/10.1023/a:1012728819326

Marin, M., Feeney, D. S., Brown, L. K., Naveed, M., Ruiz, S., Koebernick, N., Bengough, A. G., Hallett, P. D., Roose, T., Puertolas, J., Dodd, I. C., & George, T. S. (2021). Significance of root hairs for plant performance under contrasting field conditions and water deficit. *Annals of botany*, *128*(1), 1-16. https://doi.org/10.1093/aob/mcaa181

Orsila, H., Salminen, E., & Hämäläinen, T. D. (2008). *Best practices for simulated annealing in multiprocessor task distribution problems* (Vol. 16).

Parker, J. S., Cavell, A. C., Dolan, L., Roberts, K., & Grierson, C. S. (2000). Genetic interactions during root hair morphogenesis in Arabidopsis. *Plant Cell*, *12*(10), 1961-1974. https://doi.org/10.1105/tpc.12.10.1961

Pietrzyk, P., Bonelli, W., & Bucksch, A. (2022). *DIRT/mu container*. Docker. https://hub.docker.com/r/computationalplantscience/dirtmu

Pietrzyk, P., & Bucksch, A. (2022). *DIRT/mu repository*. GitHub. https://github.com/Computational-Plant-Science/DIRTmu

Pietrzyk, P., & Saengwilai, P. (2022). *PhenomeForce 2022: DIRT/mu for root hairs phenotyping*. https://www.youtube.com/live/fwQIPYXAaYI?si=p7oKzvUKSNMUthhV

Rongsawat, T., Peltier, J. B., Boyer, J. C., Very, A. A., & Sentenac, H. (2021). Looking for Root Hairs to Overcome Poor Soils. *Trends in plant science*, *26*(1), 83-94. https://doi.org/10.1016/j.tplants.2020.09.001

Roy, A., & Bucksch, A. (2021). Root hairs vs. trichomes: Not everyone is straight! *Current Opinion in Plant Biology*, *64*, Article 102151. https://doi.org/10.1016/j.pbi.2021.102151

Saengwilai, P., Strock, C., Rangarajan, H., Chimungu, J., Salungyu, J., & Lynch, J. P. (2021). Root hair phenotypes influence nitrogen acquisition in maize. *Annals of botany*, *128*(7), 849-858. https://doi.org/10.1093/aob/mcab104

Schindelin, J., Arganda-Carreras, I., Frise, E., Kaynig, V., Longair, M., Pietzsch, T., Preibisch, S., Rueden, C., Saalfeld, S., Schmid, B., Tinevez, J. Y., White, D. J., Hartenstein, V., Eliceiri, K., Tomancak, P., & Cardona, A. (2012). Fiji: an open-source platform for biological-image analysis. *Nature Methods*, *9*(7), 676-682. https://doi.org/10.1038/nmeth.2019

Seale, M., Cummins, C., Viola, I. M., Mastropaolo, E., & Nakayama, N. (2018). Design principles of hair-like structures as biological machines. *Journal of the Royal Society Interface*, *15*(142), Article 20180206. https://doi.org/10.1098/rsif.2018.0206

Singh, G., Pereira, D., Baudrey, S., Hoffmann, E., Ryckelynck, M., Asnacios, A., & Chaboute, M. E. (2021). Real-time tracking of root hair nucleus morphodynamics using a microfluidic approach. *Plant Journal*, *108*(2), 303-313. https://doi.org/10.1111/tpj.15511

Soltis, P. S., Nelson, G., Zare, A., & Meineke, E. K. (2020). Plants meet machines: Prospects in machine learning for plant biology. *Applications in Plant Sciences*, *8*(6), Article e11371. https://doi.org/10.1002/aps3.11371

Swetnam, T. L., Antin, P. B., Bartelme, R., Bucksch, A., Camhy, D., Chism, G., Choi, I., Cooksey, A. M., Cosi, M., Cowen, C., Culshaw-Maurer, M., Davey, R., Davey, S., Devisetty, U., Edgin, T., Edmonds, A., Fedorov, D., Frady, J., Fonner, J., . . . Lyons, E. (2023). CyVerse: Cyberinfrastructure for Open Science. *bioRxiv*, 2023.2006.2016.545223. https://doi.org/10.1101/2023.06.16.545223

Tracy, S. R., Black, C. R., Roberts, J. A., & Mooney, S. J. (2011). Soil compaction: a review of past and present techniques for investigating effects on root growth. *Journal of the Science of Food and Agriculture*, *91*(9), 1528-1537. https://doi.org/10.1002/jsfa.4424

Vincent, C., Ebert, R., & Hermans, C. (2022). Root hair quantification is an accessible approach to phenotyping important functional traits. *Journal of Experimental Botany*, *73*(11), 3304-3307. https://doi.org/10.1093/jxb/erac102

Vincent, C., Rowland, D., Na, C., & Schaffer, B. (2017). A high-throughput method to quantify root hair area in digital images taken in situ. *Plant and Soil*, *412*(1-2), 61-80. https://doi.org/10.1007/s11104-016-3016-9

CHAPTER 3

OPTIMIZING ROOT PHENOTYPING: ASSESSING THE IMPACT OF CAMERA CALIBRATION ON 3D ROOT RECONSTRUCTION [2]

---

[2] Pietrzyk, P., Liu, S., & Bucksch, A. Submitted to *Plant Methods*, March 9, 2025

Abstract

Accurate 3D reconstruction is essential for high-throughput plant phenotyping, particularly for studying complex structures such as root systems. While photogrammetry and Structure from Motion (SfM) techniques have become widely used for 3D root imaging, the camera settings used are often underreported in studies, and the impact of camera calibration on model accuracy remains largely underexplored in plant science. In this study, we systematically evaluate the effects of focus, aperture, exposure time, and gain settings on the quality of 3D root models made with a multi-camera scanning system. We show through a series of experiments that calibration significantly improves model quality, with focus misalignment and shallow depth of field (DoF) being the most important factors affecting reconstruction accuracy. Our results further show that proper calibration has a greater effect on reducing noise than filtering it during post-processing, emphasizing the importance of optimizing image acquisition rather than relying solely on computational corrections. This work improves the repeatability and accuracy of 3D root phenotyping by giving useful calibration guidelines. This leads to better trait quantification for use in crop research and plant breeding.

Background

Plant phenotyping has undergone a significant transformation thanks to advanced imaging and computer vision techniques (Fiorani & Schurr, 2013; Li et al., 2020; Paulus, 2019; Pound et al., 2017), particularly to exploit the information encoded in a plant's morphology (Bucksch et al., 2017) from a whole plant level (Dhondt et al., 2013) to single-cell structures like unicellular root hairs (Pietrzyk et al., 2024). Within this area of research, high-resolution three-dimensional (3D) reconstruction of plants has emerged as a powerful tool for studying plant architecture (Bao et al., 2019; Boogaard et al., 2023; Chéné et al., 2012), growth dynamics (Daviet et al., 2022; Salter et al., 2021), and responses to various environmental or agricultural stimuli (Rossi et al., 2022). Among technologies to create such 3D models of plants are Lidar (Lin, 2015; Sun et al., 2018), laser light-section (Uhrmann et al., 2011), depth cameras (Chéné et al., 2012), and X-ray Computed Tomography (CT) (Claussen et al., 2023; Duncan et al., 2022), as well as methods based on collections of two-dimensional (2D) color images (Liu et al., 2017; Nguyen et al., 2016). These non-destructive and high-throughput approaches provide valuable insights into crop yield and plant resistance to biotic and abiotic stress, whether in the field or indoors, spanning scales from plant organs to individual plants to whole plots (Walter et al., 2015). The insights include key information improving crop productivity and plant resilience to biotic and abiotic stress.

Image-based phenotyping of crop roots (Bucksch et al., 2014), in particular, has gained prominence due to the pivotal role of roots in nutrient uptake, water acquisition, and overall plant performance (Lynch, 2019; Paez-Garcia et al., 2015; Tracy et al., 2020). The integration of root phenotyping with 3D measurement techniques can significantly enhance our ability to capture and analyze root traits and to identify corresponding genes (Topp et al., 2013). While X-ray CT has been used to study root traits of plants grown in pots, in recent years 3D reconstruction from 2D images has been increasingly utilized to measure traits of excavated roots from plants grown in the field. By utilizing camera rigs equipped with multiple high-resolution 2D color cameras and employing techniques from close-range photogrammetry, researchers can now generate detailed 3D models of plant roots in a cost-efficient way (Liang et al., 2020; Liu et al., 2021; Sunvittayakul et al., 2022). However, the success of this phenotyping technique heavily depends on the quality of the generated 3D point clouds, as it forms the foundation for further processing steps such as skeletonization and trait extraction (Liu et al., 2023).

Central to the success of 3D reconstruction of plants, both roots and shoots, from 2D images is the careful calibration of the camera itself, i.e. intrinsic and extrinsic parameters, and the adjustment of camera settings, as for example focus, aperture, shutter speed, and gain. The two types of calibration play distinct but complementary roles in producing high-quality 3D points clouds for phenotyping.

Camera calibration refers to the estimation and correction of intrinsic parameters, which include focal length, principal point, and lens distortion, and extrinsic parameters that are related to the camera's position and orientation in space (Luhmann et al., 2016; Remondino & Fraser, 2006). This process ensures that the geometry of a scene is accurately defined and is often performed automatically using methods such as Structure from Motion (SfM) (Schönberger et al., 2016). Proper calibration is essential for ensuring that the 3D reconstruction reflects the true spatial relationship within the scene. The capability to automatically self-calibrate cameras using algorithms such as SfM, eliminating the need for manual camera calibration by the user, is an appealing feature for large-scale plant phenotyping and has allowed many researchers to use 3D reconstruction of plants at organ, individual plant, and plot scales.

On the other hand, camera settings—such as focus, aperture, shutter speed, and gain—do not directly alter the geometric calibration but play a crucial role in optimizing image quality (see Box 3.1). These settings affect the clarity, sharpness, and exposure of the captured images, which in turn influences the accuracy of the resulting 3D point cloud (Eltner & Sofia, 2020). Many of these settings can be interdependent. For example, changing either the root or the camera position will require readjustment of the camera's focus. Similarly, changing the aperture (f-value) from a wide-open iris with f/2 to a small iris with f/8 will increase Depth of Field (DoF) and thus the overall sharpness of the imaged root. At the same time, the closed iris allows less light to reach the camera sensor and thus results in darker images, which must be compensated for either with longer exposure times, higher gain or additional light to obtain the same image brightness. As a result, it is crucial to consider the effect of each setting on image quality and define requirements to adjust these.

Despite their critical role in image quality, camera settings are often underreported in plant phenotyping studies (Liang et al., 2020; Wu et al., 2020). Some studies evaluate the effect of other variables, such as image resolution or viewing angle, on model quality but either do not report aperture, shutter speed and gain at all or use vague language (Li et al., 2021; Lu et al., 2020; Rossi et al., 2020). Suboptimal camera settings can result in deteriorated 3D reconstructions, making the subsequent skeletonization and root trait extraction less reliable. The insufficient reporting of these settings in turn can impact the reproducibility of the results, as has already been observed with the lack of documentation and transparency in the development of other imaging pipelines for plant phenotyping (Lobet, 2017).

Focus addresses the distance between the camera's sensor and the focal point, where the subject appears sharpest in the image. A camera focused on the root ensures that specific regions of the roots, especially fine root structures, are sharp and detailed. Poor focus can blur essential features, making it difficult to reconstruct accurate 3D models.

Aperture controls the amount of light entering the camera and affects the DoF, i.e. the range of the scene that appears sharp. A small aperture (high f-number) increases the DoF, ensuring more of the plant is in focus, which is crucial for capturing detailed structures in complex root systems. However, a smaller aperture (small f-number) reduces light, requiring adjustments in other settings like shutter speed to maintain brightness, and can result in blur caused by diffraction.

Shutter speed determines the exposure time—the duration that the camera sensor is exposed to light. In dynamic environments, such as phenotyping platforms where cameras or plants may move, a fast shutter speed prevents motion blur. However, a faster shutter reduces the amount of light reaching the sensor, potentially darkening the image.

Gain (ISO) controls the camera sensor's sensitivity to light. Increasing gain brightens the image in low-light conditions but introduces noise, which can obscure fine plant details. Lower gain settings are preferred to minimize noise and preserve image clarity for accurate 3D reconstructions.

Box 3.1: Definition of common camera settings.

Considering these factors, this study aims to guide non-experts through the camera setup process and to illustrate the influence of specific camera settings on the quality and accuracy of 3D point clouds of roots. By using a multi-view 3D system with ten cameras rotating around an excavated maize root crown (Liu et al., 2021), our research aims to explore how variations in focus, aperture, shutter speed, gain and other camera settings affect the resulting 3D models.

Although the study is based on this particular system, the underlying principles are broadly applicable to other multi-view reconstruction systems. Given the dense and highly occluded nature of maize root crowns with fine structures in the order of 100 microns in diameter, achieving accurate reconstructions is challenging but essential for precise phenotyping. The pipeline for 3D reconstruction incorporates COLMAP (Schönberger et al., 2016) to generate a 3D point cloud and a noise filtration process to reduce noise and eliminate blunders caused by the reconstruction. By assessing the impact of camera calibration on 3D point cloud quality, this study evaluates the robustness of 3D reconstruction across different camera set-ups and challenging working environments, ultimately contributing to more reliable and reproducible phenotyping pipelines in crop science.

Materials and Methods

Root Samples

We selected 12 samples of contrasting maize (*Zea mays*) root architectures (Figure 3.1). The plants were grown in Hagerstown silt loam soil and harvested 81 d after planting at the Pennsylvania State University's Russell E. Larson Agricultural Research Center in August 2018. After harvesting, we removed the shoot above all root-producing nodes and air-dried them on a greenhouse bench. Roots were transported to the University of Georgia in Athens, GA, and were then carefully stored to avoid any damage and then imaged for this publication in February 2023.

3D Root Scanner

The 3D root scanner is described in (Liu et al., 2021) and consists of 10 cameras mounted on a round metal frame that rotates around the root sample. The scanner uses The Imaging Source DFK 27BUJ003 color cameras with 1/2.3 inch Aptina CMOS MT9J003 sensors. This camera has a maximum resolution of 10.7 megapixels, and its shutter speed ranges from $\frac{1}{20{,}000}$ to ¼ sec, gain from 0 to 12 dB, and white balance from -2 to 6 dB. The cameras are further equipped with The Imaging Source TCL 0616 5 Mega Pixel lenses with 1/1.8 inch format, fixed 6 mm focal length, aperture range from f/1.6 to f/16, and a minimum object distance of 0.1 m.

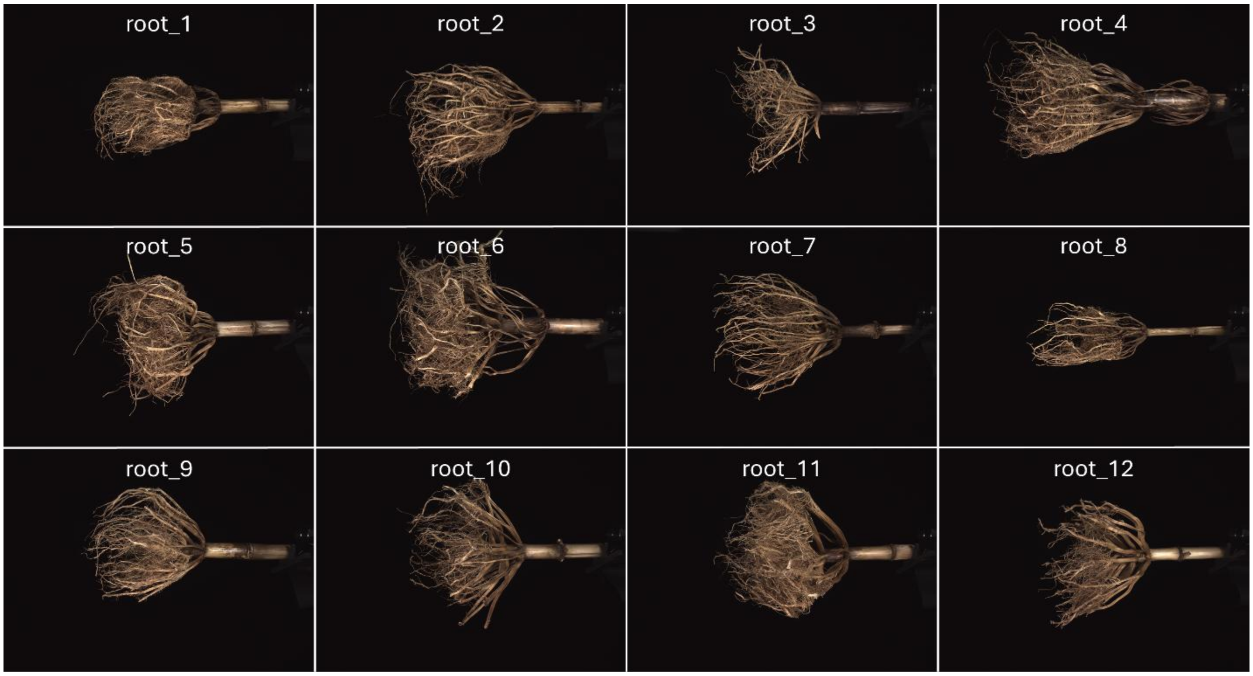

Figure 3.1: Overview of all 12 selected roots. All images were taken using the calibrated scanner set-up and have the same scale.

Adjustment of Camera Settings

To increase 3D root model quality and accuracy of measured root traits, we developed a procedure to set up the scanner, which included the position and orientation of the root sample itself and settings for the cameras and environment as listed in Table 3.1. Other factors related to the computation of the 3D model, such as intrinsic and extrinsic parameter calibration with COLMAP and its meta-parameters, were not considered. During the calibration process, we used the software tcam-capture by The Imaging Source to interactively view and save images and to test camera settings of individual cameras. We turned off the automatic adjustment of exposure and gain during this process and manually set all other camera parameters.

Table 3.1: List of parameters that were adjusted during the set-up, together with an indication of whether parameters were calibrated and analyzed for their effect on model quality.

Object	**Setting**	**Calibrated and tested**
Root	Position	Yes
	Orientation	No
Camera	Position	Yes
	Orientation	Yes
	Focus	Yes
	Aperture	Yes
	Exposure time	Yes
	Gain	Yes
	White balance	No
	Image format/quality	Yes
Environment	Light source (position and power)	No

Experiments

Experiment 1

We performed two experiments to determine the effect of scanner parameters on the quality of point clouds. An overview of the parameters used in each experiment is given in Table 3.2. In Experiment 1, we performed two tests (E1#1 and E1#2), each with all twelve roots, resulting in a total of 24 scans. The first test uses a calibrated scanner setup (focused on center, aperture of f/4, exposure time of 1/30 sec and 0 dB gain), while for the second test we simulated an uncalibrated setup using the settings from Table 3.2. For the uncalibrated scan we used an aperture of f/2 to reduce DoF, set the focal point 10cm behind or in front of the scanner center alternating between cameras, and increased gain by 12 dB (equivalent to a 16-fold exposure) to introduce speckle. Due to the higher gain and the wider aperture, we had to reduce exposure time to 1/1000 sec, which still resulted in overexposed images.

Table 3.2: Overview of parameters used in each test of Experiments 1 and 2. Bold characters indicate settings that differ from the calibrated state. The symbol * in test E2#06 indicates that one camera was set to 1/30 sec instead 1/8 sec.

	# roots	# images	Cam. dist. to center (cm)	Focus (cm from center)	Aperture	Exposure time (sec)	Gain (dB)	White balance (R, G,B)	jpg quality	Other
Experiment 1										
E1#1: Calibrated	12	680	44,2	+/-0	f/4	1/30	0	(91, 64, 76)	95	-
E1#2: Uncalibrated	12	680	44,2	**+/-10**	**f/2**	**1/1000**	**12**	(91, 64, 76)	95	**1 stop brighter**
Experiment 2										
E2#01: Calibrated	3	680	44,2	+/-0	f/4	1/30	0	(91, 64, 76)	95	-
E2#02: Jpg 100	3	680	44,2	+/-0	f/4	1/30	0	(91, 64, 76)	**100**	-
E2#03: 1/125sec	3	680	44,2	+/-0	f/4	**1/125**	0	(91, 64, 76)	95	**2 stops darker**
E2#04: 1/60sec	3	680	44,2	+/-0	f/4	**1/60**	0	(91, 64, 76)	95	**1 stop darker**
E2#05: 1/15sec	3	680	44,2	+/-0	f/4	**1/15**	0	(91, 64, 76)	95	**1 stop brighter**
E2#06: 1/8sec	3	680	44,2	+/-0	f/4	**1/8***	0	(91, 64, 76)	95	**2 stops brighter**
E2#07:1/125sec, +6dB	3	680	44,2	+/-0	f/4	**1/125**	**6**	(91, 64, 76)	95	-
E2#08: 1/500sec, +12dB	3	680	44,2	+/-0	f/4	**1/500**	**12**	(91, 64, 76)	95	-
E2#09: f/2, 1/125sec	3	680	44,2	+/-0	**f/2**	**1/125**	0	(91, 64, 76)	95	-
E2#10: f/8, 1/8sec	3	680	44,2	+/-0	**f/8**	**1/8**	0	(91, 64, 76)	95	-
E2#11: f/8, 1/15sec, +3dB	3	680	44,2	+/-0	**f/8**	**1/15**	**3**	(91, 64, 76)	95	-
E2#12: f/8, 1/30sec, +6dB	3	680	44,2	+/-0	**f/8**	**1/30**	**6**	(91, 64, 76)	95	-
E2#13: +/-10cm (#1)	3	680	44,2	**+/-10**	f/4	1/30	0	(91, 64, 76)	95	-
E2#14: +/-10cm (#2)	3	680	44,2	**+/-10**	f/4	1/30	0	(91, 64, 76)	95	-
E2#15: +/-10cm, f/2, 1/125sec (#1)	3	680	44,2	**+/-10**	**f/2**	**1/125**	0	(91, 64, 76)	95	-
E2#16: +/-10cm, f/2, 1/125sec (#2)	3	680	44,2	**+/-10**	**f/2**	**1/125**	0	(91, 64, 76)	95	-
E2#17: +/-10cm, f/8, 1/15sec, +3dB (#1)	3	680	44,2	**+/-10**	**f/8**	**1/15**	**3**	(91, 64, 76)	95	-
E2#18: +/-10cm, f/8, 1/15sec, +3dB (#2)	3	680	44,2	**+/-10**	**f/8**	**1/15**	**3**	(91, 64, 76)	95	-
E2#19: +/-17cm	3	680	44,2	**+/-17**	f/4	1/30	0	(91, 64, 76)	95	-
E2#20: +/-17cm, f/2, 1/125sec	3	680	44,2	**+/-17**	**f/2**	**1/125**	0	(91, 64, 76)	95	-
E2#21: +/-17cm, f/8, 1/15sec, +3dB	3	680	44,2	**+/-17**	**f/8**	**1/15**	**3**	(91, 64, 76)	95	-
E2#22: Distance +10cm	3	680	**54.2/50.2**	+/-0	f/4	1/30	0	(91, 64, 76)	95	-
E2#23: Camera orientation	3	680	44,2	+/-0	f/4	1/30	0	(91, 64, 76)	95	**Camera orientation**
E2#24: Root position	3	680	44,2	+/-0	f/4	1/30	0	(91, 64, 76)	95	**Root position**

Experiment 2

Experiment 2 consisted of 24 individual tests (E2#01 to E2#24) with three roots (root_3, root_4 and root_9) to further measure the sensitivity of point cloud quality and trait accuracy to individual and combined changes in scanner parameters. The first test (E2#01) acts as our calibrated setup, followed by a series of tests to study the effect of image compression (jpg quality), exposure time and gain. In E2#02 we increased image quality by reducing image compression; in E2#03 to E2#06 we changed exposure time to either under- or overexpose images; and in E2#07 we increased gain to produce grain and at the same time reduced exposure time to keep the same image brightness as in the calibrated setting. In tests E2#13 to E2#21 we changed the camera focus either alone or in combination with narrower or wider DoF. During these tests, we had to reduce exposure time at large aperture (f/2) and increase exposure time and gain at smaller apertures (f/8) to not alter image brightness. Tests E2#22 to E2#24 focused on the geometric setup of scanner and root. In E2#22, we increased the distance between the root and cameras by moving eight cameras back by 10 cm and two back by only 6 cm due to lamp mountings. In E2#23 we turned the cameras' views by approximately 10° to 15° alternating left and right from the straight view to the scanner center, such that roots were not completely imaged, or lamps were visible in images. This setup simulates suboptimal or misaligned camera configurations that may occur under field or high-throughput conditions, where perfect alignment is not always feasible. Finally, in E2#24 we moved the root 7 cm up and 7 cm to the side to simulate a lower resolution. Experiment 2 resulted in a total of 72 scans.

Scanning and Model Reconstruction

To minimize potential effects of other factors on our analysis we performed all scans in the same manner. As such, each root was marked with a black dot on the stem to assure the same placement of each root into the scanner between different tests. Further, the rotating metal frame started in the same position for all scans and revolved over an angle of 335°. Images were taken every 5°, resulting in 680 images per scan. For image acquisition the rotation of the frame was halted. All images were saved in jpg format and have a resolution of 3872 x 2764 pixels. We then computed 3D models for all 24 scans in Experiment 1 and all 72 scans in Experiment 2 with DIRT/3D (COLMAP) as described in Liu et al. (2023). In Experiment 2 the reconstruction of root_9 in tests E2#06 and E2#23 failed.

All reconstructed models were then cleaned. Points not belonging to the root were manually cropped and the stem was cropped upward from the marked black dot using CloudCompare v2.12.4 (Kyiv) (*CloudCompare*, 2022). We further applied a statistical outlier removal (SOR) filter using PyntCloud (de la Iglesia Castro et al., 2022), where for each point the mean distance to its ten nearest neighbors was computed and points with a value larger than the model's mean plus three times the standard deviation were excluded. This cleaning process resulted in the removal of isolated points and in a visible reduction of noise in the point cloud.

Feature Extraction

We then assessed the effects of calibration and other scanner settings on point cloud quality and accuracy of measured 3D root traits in Experiment 1 and Experiment 2. To assess point cloud quality, we computed the local features curvature, anisotropy, linearity, planarity, and sphericity in each 3D model based on Principal Component Analysis (PCA) using the procedure outlined in Zhang et al. (2022). Features were calculated for each point by selecting the *k* nearest neighbors of each point and performing a principal component analysis to calculate the eigenvalues (λ_1, λ_2 and λ_3) of the first, second and third principal components at the local point distribution. Based on the values the shape of the point distribution can be determined. For example, a large λ_1 compared to λ_2 and λ_3 represents a linear point distribution as would be expected in fine roots, while similar values for λ_1 and λ_2 compared to a small value for λ_3 represent a planar distribution as we can expect on the surface of the plant's stem. As such, we expect the values of linearity and planarity in our root models to decrease with increased noise due to a bad scanner setup.

Statistical Analysis

In Experiment 1 we computed the means of the features curvature, anisotropy, linearity, planarity, and sphericity using k equal to 200 in each point cloud before and after application of the SOR filter for models of all tests. We then analyzed the effect of calibration as well as filtering on all five features using a paired t-test. In Experiment 2 we computed the mean values of curvature, anisotropy, linearity, planarity, and sphericity without the SOR filter for all tests (E2#02 – E2#23) and compared them to the calibrated setup (E2#01) as a percentage change.

Results

Scanner Calibration

Calibration Objectives

The calibration of the root scanner is a critical process that ensures accurate and precise imaging for 3D reconstruction. To achieve this, we established specific calibration goals and defined the necessary actions to meet them (Table 3.3). Based on these, the first step in the calibration process is setting the position and orientation of the cameras, light sources, and root. This ensures that the root system is well-covered in all images. Once this setup is complete, we focus the cameras on the scanner's center, where the root will be placed. With the root positioned and the cameras' focal point aligned in the scanner center, we adjust the DoF by selecting an appropriate aperture setting. Since DoF is a key calibration parameter, the aperture should be set to maximize sharpness across the entire root system, rather than being used to adjust image brightness. However, since light and the camera’s diffraction limit can be limiting factors, the aperture should be kept as large as possible while still maintaining sufficient DoF. After setting the aperture, we adjust the white balance to achieve a natural color representation in the images. Finally, we fine-tune exposure time and gain to ensure adequate brightness without degrading image quality. By following this systematic approach, the scanner can effectively capture detailed imagery of complex root structures, enabling accurate 3D reconstructions and analyses. Each of these steps requires careful manual and visual precision, highlighting the importance of a well-prepared setup for achieving precise calibration, as discussed in the following sections.

Table 3.3: Overview of objectives to achieve high-quality root images.

Goals	Actions	Dependencies/Tradeoffs/other
Maximize coverage of root in all images.	Position root in scanner's center. Move cameras forward/backward. Orient cameras to scanner's center.	Depends on root and scanner size. Can result in lower resolution to fit root in image; limited by fixed field of view.
360° view of root.	Position root in scanner's center. Orient cameras to scanner's center. Distribute cameras on arch.	Limited by rotation angle of scanner and distribution of cameras.
Consider varying root density.	Orient root along scanner's axis of rotation. Place more cameras toward bottom of root.	Results in less images of top view of root.
Sharp root images.	Center the focal point on scanner's center. Close aperture (larger f-number) to increase DoF. Move cameras further away from root to increase DoF.	Depends on root position and size, and camera distance. Results in darker images. Larger distances lead to lower resolution.
Homogenous illumination of root.	Add more diffuse light.	Space on arch is limited. Light source must not be visible in images. Heat accumulation.
Avoid camera shake and motion blur.	Keep exposure time as short as possible.	Results in darker images.
Limit noise in image.	Set gain close to minimum value (higher gain results in speckle). Ideally set to zero.	Less gain results in darker images.
Image quality	Set low image compression. Set white balance.	Low compression leads to bigger file size.
Avoid under/overexposure of root.	Set light, exposure and gain to appropriate levels. Do not use aperture to control brightness. Use diffuse light from multiple sources.	Avoid overexposed images, because saturated pixels cannot be recovered. Underexposed parts can be enhanced.

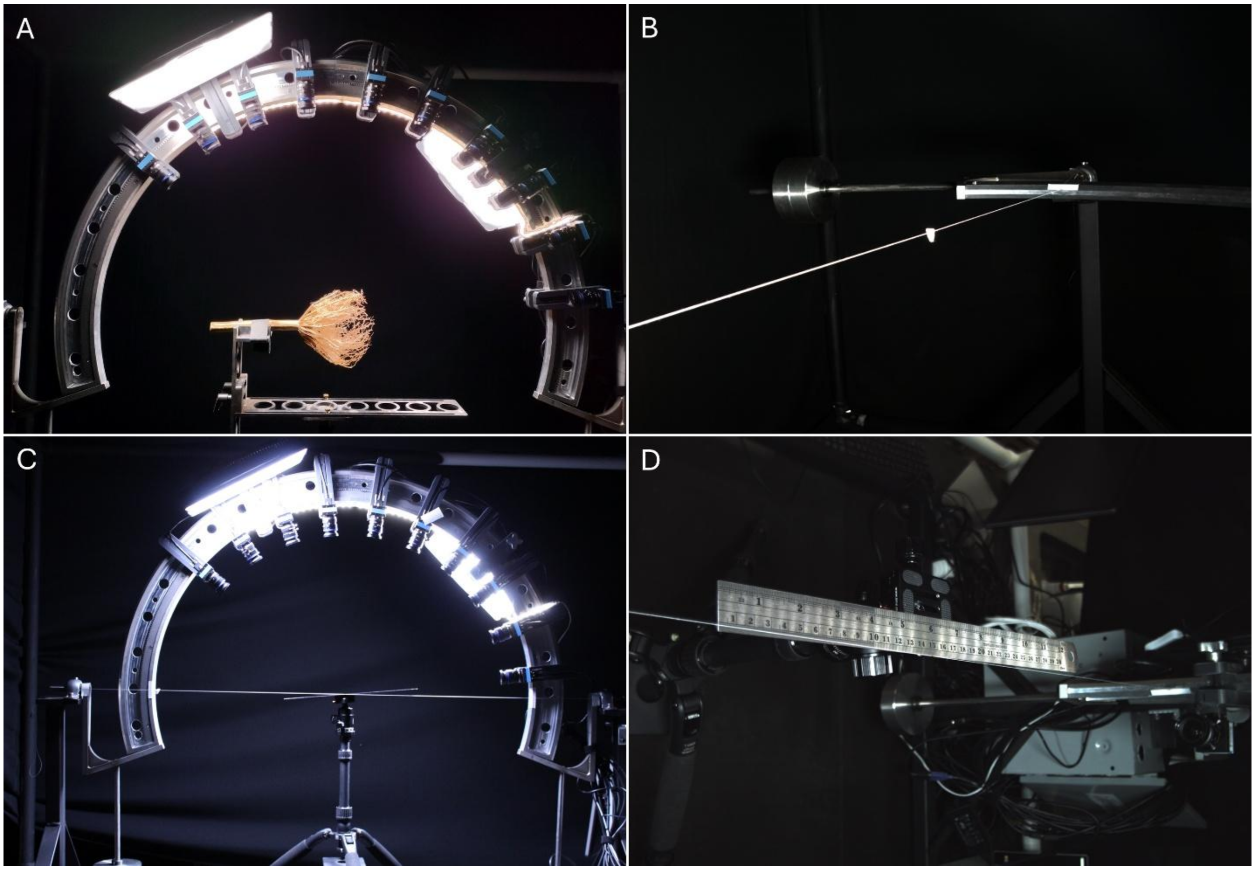

Figure 3.2: Image of calibrated scanner with maize root and calibration steps. (A) The calibrated scanner with the root in the center. (B) A white marker attached to thread spanned across the center of the scanner as seen from a camera. (C) A ruler was placed in the center of the scanner and tilted to focus each camera. (D) The ruler as seen from a camera.

Scanner Calibration Procedure

Pre-calibration: Before initiating the calibration process, baseline adjustments were made to enable initial captures of images and the calibration of camera position and orientation. The power settings of the light sources were set to their maximum value. This preliminary step involved setting rough adjustments of focus, aperture and exposure based on visual inspection of the images to facilitate further adjustment during the calibration process.

Root position and orientation: We positioned the root in the center of the scanner such that the distance between the center of the root system and cameras does not change when the camera rig rotates around the root, enabling the use of a constant focusing distance (Figure 3.2A). We further aligned the stem and the scanner's axis of rotation, with the stem pointing away from the scanner's motor and the bottom of the root pointing toward it.

Camera Position: The scanner calibration process started with adjustments to the position of all ten cameras on the arch. The rightmost camera (PiController) was set at an angle of 7.5° from the rotation axis of the camera arch allowing images from the bottom and inside of the root crown (Figure 3.2A). We uniformly spaced the remaining nine cameras at an angle of 15° between them, resulting in an overall coverage of 135°. All cameras were moved as far forward toward the scanner as was possible on the mounting attached to the arch, resulting in a distance between the scanner center and camera sensors of 44.2cm. Due to thicker roots and fewer fine roots at the top of the root system, we did not place cameras on the left side of the scanner.

Camera Orientation: The process of adjusting camera orientation began by positioning a white marker at the center of the scanner, corresponding to the anticipated location of the root (Figure 3.2B). To achieve this, a white thread was extended across the scanner, spanning from one side to the other along the rotational axis of the scanner arch. Moreover, the midpoint of the thread was identified, and a white marker was affixed to it, ensuring enhanced visibility of the scanner's center in images captured by all ten cameras. Subsequently, all cameras were aligned to orient the marker as closely as possible to image centers. It should be noted that only adjustments to the camera's yaw angle (i.e., rotation left or right) were performed due to the fixed mounting of the cameras on the arch. As such, the pitch and roll angles were not adjustable. Throughout this adjustment process, TCam Capture facilitated real-time image monitoring. Consequently, the reorientation of all cameras toward the center of the scanner was achieved.

Light Sources: The two light sources were attached to the arch such that they were as far apart as possible without being in the field of view of any of the cameras (Figure 3.2A). At this point we kept the power of the light source at the maximum setting.

Camera Focus: Optimization of camera focus was crucial for maintaining sharp focus of the entire root structure throughout all camera positions. Because the cameras used are not equipped with automatic focus this procedure had to be performed manually and individually for all ten cameras. For focus distance the lens had markings at 0.1m, 0.3m and infinity. As such, this step posed the greatest difficulty and demanded considerable time. To facilitate this process, a ruler was affixed to a camera tripod before being placed inside the scanner (Figure 3.2C). The ruler was then pointed toward the camera and tilted to produce an angle of 45° between the ruler and the straight line from the scanner's center to the camera's center. It was further ensured that the ruler's center was always aligned with the center of the scanner during the entire process. The aperture of the camera was then set to the lowest f-number (f/1.6) by turning the aperture ring of the lens to create a shallow DoF. An image was captured using TCam Capture, and the focus point was determined based on the sharpness of the ruler's lines and numbers in the image (Figure 3.2D). The focus was then adjusted to focus on the center of the ruler by turning the focus ring accordingly. If the focus was found to be too close to the camera, the focus distance was increased; conversely, if the focus was too far from the camera, it was decreased. Another image was captured using the TCam Capture tool to verify the accuracy of the focus. This process was repeated until optimal results were achieved for all cameras.

Aperture: Ensuring an optimal DoF was paramount to maintain sharpness across the entire root system. We utilized the same setup with a ruler from the previous calibration step to facilitate DoF assessment (Figure 3.2D). Visual inspection of the sharpness of the ruler's lines and numbers in images served as our guide in selecting the ideal aperture setting. Our criterion for achieving sufficient DoF encompassed the sharpness of all markings on the 30 cm long ruler.

The aperture range of our camera lenses spanned from f/1.6 (large iris) to f/16 (small iris). We initiated the process with an aperture setting of f/2 as our starting point, progressively increasing the f-number using only settings marked on the camera lenses (i.e., f/2, f/2.8, f/4, f/8) until the desired DoF was attained. These settings facilitated straightforward calculations of exposure times needed to compensate for the smaller iris by doubling exposure time between f/2 and f/2.8, f/2.8 and f/4, and quadrupling exposure time between f/4 and f/8, ensuring consistent image brightness across different aperture settings.

Compensating for darker images resulting from smaller apertures necessitated a corresponding increase in exposure time. Given the inherent trade-off between DoF and image brightness associated with aperture adjustment, we selected f/4 as the largest aperture that would still yield sharp representations of all parts of the root system.

White balance: To also ensure natural looking images the white balance of the camera was calibrated. To obtain the value for white balance we placed a white sheet of paper in front of a camera and used TCam Capture’s feature to automatically adjust white balance. This was repeated for each camera and the detected values for red, green and blue were averaged across all cameras, resulting in the values 91, 64 and 76 for the red, green and blue channels, respectively. These values were used in TCam Capture to set the white balance.

Exposure time: As previously mentioned, it is generally imperative to maintain the exposure time as short as possible to mitigate camera shake and motion blur. Due to the non-moving root and the static position of the cameras during exposure we expected that these would not be a major concern. However, we observed that thin and long roots vibrated. In either case of short and long exposure time this would lead to inaccuracies during 3D reconstruction and neither short nor long exposure times would be able to alleviate its effect. In this setup, an exposure of 1/30 sec resulted in images with sufficient brightness, while not overexposing any parts of the root system.

Gain: Finally, the gain was adjusted. After aperture, exposure time and illumination, an increase in gain is the last possibility to enhance image brightness. Nevertheless, high gain also leads to increased noise levels in the form of speckle within the image. Therefore, efforts were made to maintain the gain at the lowest level. Since the exposure time of 1/30 sec seemed to suffice for image brightness, the gain was set to its lowest value of 0 dB (TCam Capture setting of 100).

Experiment 1

We used all 12 roots to compare the calibrated scanner setup versus an uncalibrated scanner setup, resulting in 24 root models. All models were manually cleaned and cropped, and outliers were removed with the SOR filter. For all models the five features and number of points were calculated before and after applying the SOR filter.

Quality assessment

The effects of calibrating the scanner and cameras on the images of the roots can be easily observed by visual inspection of the images. In the image of the calibrated scanner the complete root system is well exposed, i.e. all roots are sufficiently bright and none are overexposed (Figure 3.3, top). Further all parts in the front and back of the root remain sharp, and details such as fine roots can be seen as well as the resolution of the image allows. In contrast, the root system in the uncalibrated image is overexposed due to the combined effects of a large aperture and high gain; the roots that are closer to the camera are blurred due to the incorrect focus and large aperture, and speckle is visible due to the high gain.

A visual presentation of a 3D model generated with COLMAP after scanner calibration and its linear, planar, and spherical features are given in Figure 3.4. A comparison of the 3D point cloud with the image corresponding to the same viewing angle shows accurate resemblance between the overall root structures as well as fine roots. Generally, it can be observed though that fine roots appear thicker in the 3D model than in the image. The visualization of linearity, planarity, and sphericity shows differences between separate parts of the root. Due to the large surface area the stem has the largest values in planarity, while linearity and sphericity are low. Some smaller regions on the stem show smaller values of planarity and higher values of sphericity. Larger values of planarity can be further seen at the thickest roots. Linear features can only be detected in fine roots within the root crown if they are sufficiently thin. Overall, only a few points exhibit this high linearity. Regarding sphericity no visible points exhibit a large value, but many points corresponding to thicker roots in the crown root show a moderate sphericity around a value of 0.5.

The effects of calibration and filtering on the reconstructed models are visualized by the noise present on the stem cross-section in Figure 3.5. In both the uncalibrated and calibrated setups several isolated outliers are present because of mismatched image pixels during the 3D reconstruction. This type of noise was successfully removed in both cases by application of the SOR filter. Nonetheless, the root model from the uncalibrated scanner exhibits a rougher stem surface with more noise than the root model from the calibrated scan. This characteristic even prevails after the application of the SOR filter. As such, we see that the root model from the calibrated scan together with filtering results in the most accurate representation of the planar stem surface.

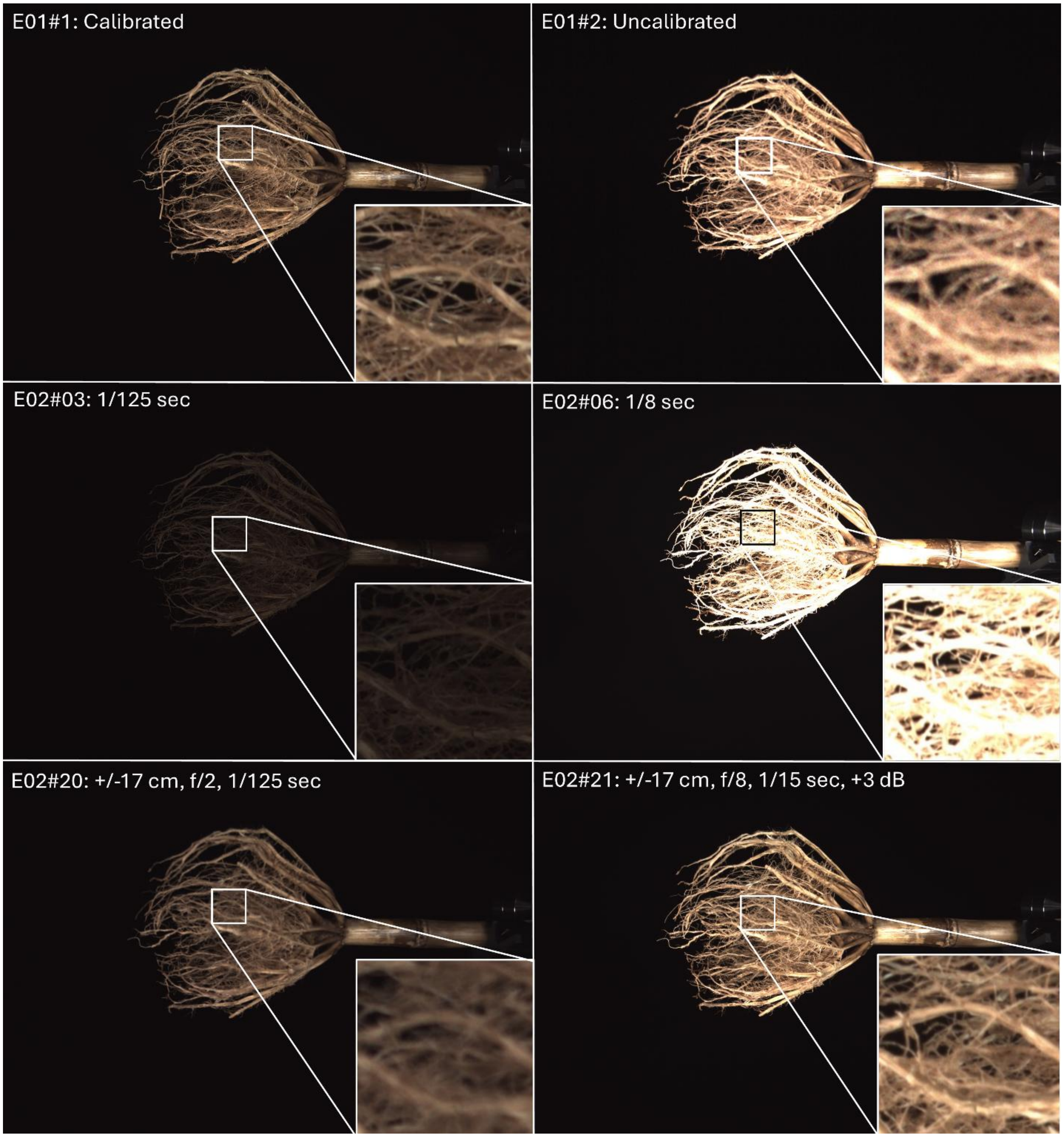

Figure 3.3: Images of root_9 from six different tests. The boxes zoom into a small part of the root crown in each image to highlight differences coming from different scanner setups. The top row shows the calibrated and uncalibrated setup, the middle row the effects of image brightness (due to exposure time), and the bottom row the combined effects of focus and aperture.

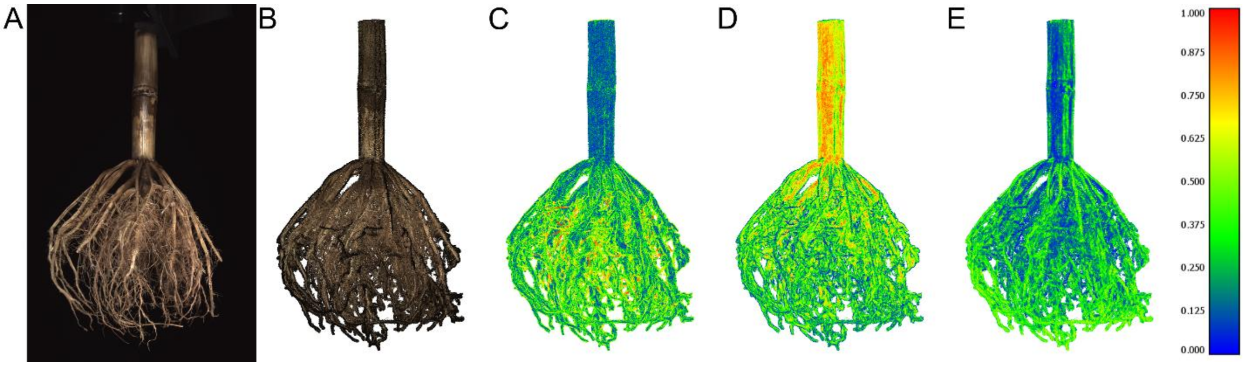

Figure 3.4: Image and 3D models with original root color and computed features for root sample root_9. (A) Cropped jpg image of root taken during the scanning process with calibrated scanner. (B) 3D point cloud of root after reconstruction with COLMAP and after cleaning and filtering, where points correspond to 3D measurements of the root. (C-E) Features illustrating the local distribution of points using 200 nearest neighbors (k=200), where (C) depicts linearity, (D) planarity and (E) sphericity on a scale from 0 to 1. High values of linearity, planarity or sphericity are thus shown in red, whereas low values are shown in blue.

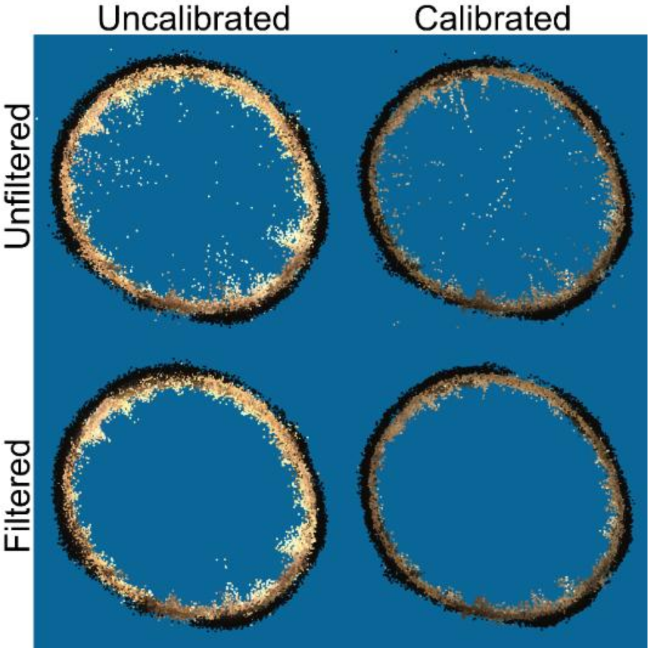

Figure 3.5: Effect of calibration and filtering on point cloud quality shown at the cross-section of the stem. Cross-sections of stems were cropped above the root crown from point clouds of sample root_9 and have a width of approximately 1 cm. The top-left cross-section was taken from the uncalibrated and unfiltered, top-right from calibrated and unfiltered, bottom left from uncalibrated and filtered, and the bottom right from the calibrated and filtered model.

For the calculation of the five features, we used a value of 200 for the number of neighbors, *k*. Our choice was based on an assessment of the mean curvature, mean anisotropy, mean linearity, mean planarity, and mean sphericity using different values for *k* (10, 25, 50, 100, 200, 300, 400) in all twelve models from test E1#1. The logic for choosing a value of 200 was therefore that planarity converges to a relatively stable value at *k* equal to 200 (see Figure 3.6). All features were computed with PyntCloud (de la Iglesia Castro et al., 2022).

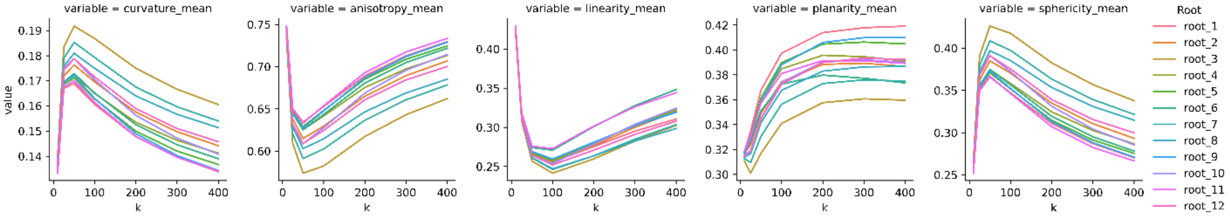

Figure 3.6: Mean of the five features (curvature, anisotropy, linearity, planarity, and sphericity) for 12 root models as a function of k (number of nearest neighbors). Each line depicts the mean value of a single root model. Features were computed on models from the calibrated scanner setup in test E1#1 and before the application of the SOR filter.

Computation of the five features enabled us to quantify differences in local point distributions between 3D models. Figure 3.7 shows that local point distributions of the whole 3D model change because of the scanner calibration. Overall, we observed an increase in linearity, planarity and consequently anisotropy, and a decrease in curvature and sphericity with the calibrated scanner. We further observed the same effect of scanner calibration on local point distribution in all twelve roots (see Figure 3.8). In models from the calibrated scan without SOR filter the mean curvature across all 12 roots decreased by 7.1% from 0.169 to 0.157 ($p<0.001$), mean anisotropy increased by 5.2% from 0.634 to 0.667 ($p<0.001$), mean linearity increased by 6.3% from 0.261 to 0.278 ($p<0.001$), planarity increased by 4.5% from 0.373 to 0.389 $p<0.001$)

and sphericity decreased by 9.1% from 0.366 to 0.333 (p<0.001) compared to models from uncalibrated scans (see Table 3.4). Similarly, we saw a mean decrease in the number of points by 3.2% from 5,702,920 to 5,519,870.4 (p<0.01).

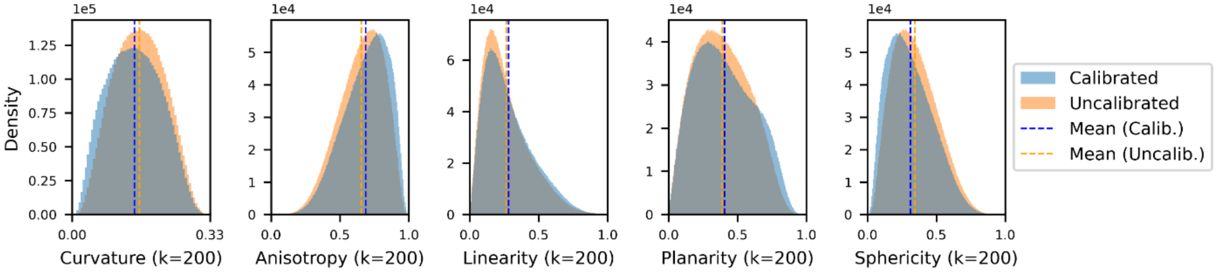

Figure 3.7: Histograms showing the distribution and mean values of curvature, anisotropy, linearity, planarity, and sphericity of sample root_9 before and after scanner calibration. Features were computed before the application of the SOR filter and with k=200. The width of each bin is 0.005.

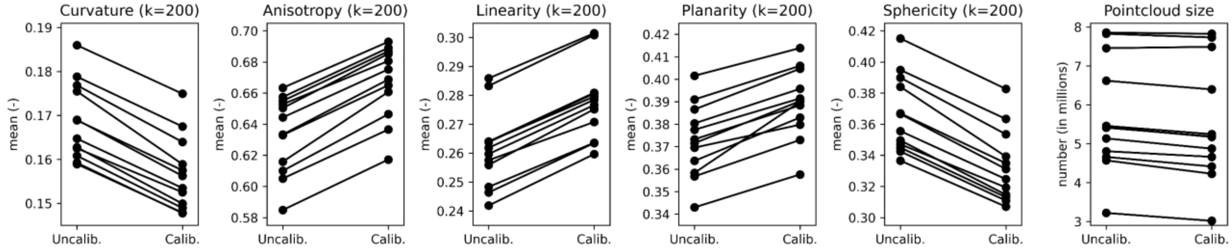

Figure 3.8: Effect of calibration on curvature, anisotropy, linearity, planarity, sphericity, and point cloud size for paired samples. Values on the left and right in each plot correspond to measurements of point clouds from uncalibrated and calibrated scans, respectively. For curvature, anisotropy, linearity, planarity, and sphericity each filled circle represents its mean calculated for a single point cloud. Point cloud size is shown as the total number of points in each point cloud. All values were computed before the application of the SOR filter. The lines connecting circles indicate corresponding pairs of models before and after calibration.

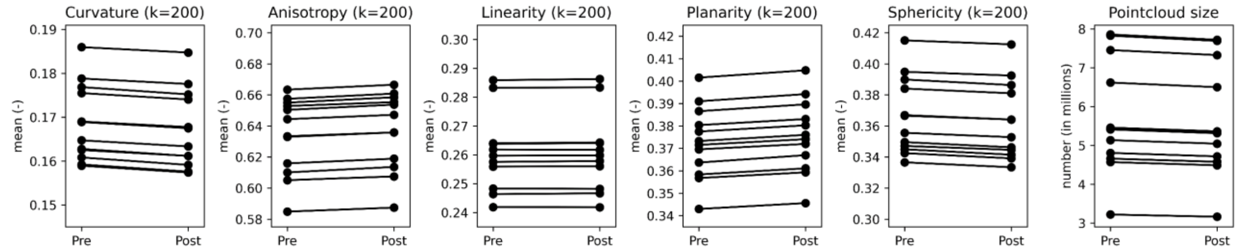

Figure 3.9: Effect of SOR filter on curvature, anisotropy, linearity, planarity, sphericity, and point cloud size for paired samples. Values on the left and right in each plot correspond to measurements of point clouds before and after the SOR filter, respectively. For curvature, anisotropy, linearity, planarity, and sphericity each filled circle represents its mean calculated for a single point cloud. Point cloud size is shown as the total number of points in each point cloud. All values were computed for the uncalibrated scanner setup. The lines connecting circles indicate corresponding pairs of models before and after the SOR filter.

Table 3.4: Mean values for curvature, anisotropy, linearity, planarity, sphericity, and point cloud size over all twelve roots. Mean values are shown for uncalibrated-unfiltered, calibrated-unfiltered, uncalibrated-filtered, and calibrated-filtered point clouds. Change is computed with respect to uncalibrated-unfiltered root models.

	Unfiltered Uncalibrated	Unfiltered Calibrated		Filtered Uncalibrated		Filtered Calibrated	
	Mean	Mean	Change (%)	Mean	Change (%)	Mean	Change (%)
Curvature	0.169	0.157	-7.1%	0.167	-0.9%	0.155	-8.1%
Anisotropy	0.634	0.667	5.2%	0.637	0.5%	0.671	5.8%
Linearity	0.261	0.278	6.3%	0.261	0.1%	0.278	6.5%
Planarity	0.373	0.389	4.5%	0.376	0.8%	0.392	5.3%
Sphericity	0.366	0.333	-9.1%	0.363	-0.8%	0.329	-10.0%
Point cloud size	5,702,920.0	5,519,870.4	-3.2%	5,602,054.2	-1.8%	5,425,764.8	-4.9%

We further tested which effect filtering has on the local point distribution by comparing features before and after the application of the SOR filter in the uncalibrated scan (see Figure 3.9). In models after SOR filtering the mean curvature decreased by 0.9% from 0.169 to 0.167 ($p<0.001$), mean anisotropy increased by 0.5% from 0.634 to 0.637 ($p<0.001$), mean linearity increased only by 0.1% (p<0.01), planarity increased by 0.8% from 0.373 to 0.376 (p<0.001) and sphericity decreased by 0.8% from 0.366 to 0.363 (p<0.001) compared to models without filtering (see Table 3.4). Similarly, we saw a decrease in the mean number of points by 1.8% from 5,702,920 to 5,425,764.8 (p<0.001). Further, we observed that the sum of the individual effects of calibration and filtering at large adds up to the same amount as the effect of calibration combined with filtering (Table 3.4).

Experiment 2

In Experiment 2 we performed a total of 24 tests using three models (only two models in tests E2#06 and E2#23). All resulting models were manually cleaned and cropped. Next the five features, number of points, and root traits were computed without the application of the SOR filter.

Quality assessment

The individual adjustments to the scanner setup can have a significant impact on the quality of the images taken. In the highly underexposed images of test E02#03 with an exposure time of 1/125 sec the image is just bright enough that the root can be seen, while in the overexposed images of test E02#06 with an exposure time of 1/8 sec most parts of the root are severely overexposed, such that they appear as plain white and hence fewer features of the fine roots are visible (Figure 3.3, middle). In images from test E02#20, the use of a large aperture (f/2) resulted in bad focus and shallow DoF, causing most details in fine roots to appear too blurred to discern. In contrast, the issue is largely resolved in images from test E02#21, where a small aperture (f/8) resulted in a greater DoF (Figure 3.3, bottom)

The effect of changes to individual scanner settings or groups of camera settings on the five features and point cloud size is shown in Figure 3.10. Overall, most tests had little to no effect (under 1-2%) on curvature, anisotropy, linearity, planarity, sphericity or point cloud size. The largest decrease and the largest increase in curvature relative to the calibrated scan were in test E2#24 with modified root position (-5.3%) and test E2#20 with an unfocused camera and large aperture (24.4%), respectively. The largest decreases in anisotropy (-16.2%), linearity (-13.6%) and planarity (-18.0%) were also in test E2#20 with an unfocused and large aperture setting. And the largest increases in anisotropy (3.5%), linearity (4.1%) and planarity (3.0%) were in test E2#24 with modified root position. The largest decrease in point cloud size was in test E2#20 with an increased camera-to-root distance (3.3%) and the largest increase was in test E2#16 with an unfocused camera and large aperture. Despite the large effect in some tests, only 8 out of 23 tests had deviations in either feature values or point cloud size from the calibrated setup that are larger than five percent.

We observed noteworthy effects in tests related to very short or long exposure times, large apertures, unfocused setups and altered scanner-root geometries. Setups with short (E2#03) and long (E2#06) exposure times, i.e. under- and overexposed images, resulted in a smaller point cloud size but had only a small effect on geometric features. Increasing the aperture to f/2 (E2#09) resulted in slightly worse geometric features but reducing it to f/8 (E2#10) only resulted in small differences under 1.1% compared to the calibrated scans, indicating that the narrower DoF caused by the larger aperture of f/2 resulted in a decrease in model quality. An aperture of f/2 and the focal point being 10cm off-center (E2#15 and E2#16) resulted in worsening of all five features but did not affect point cloud size. Contrary to that, the focal point being 10cm off-center with our standard aperture of f/4 (E2#13 and E2#14) and a small aperture of f/8 (E2#17 and E2#18) showed no effect on any feature or the point cloud size. Further, moving the focal point 17cm off-center with a large aperture of f/2 (E2#20) resulted in the largest increases in curvature and sphericity, the largest decreases in anisotropy, linearity, and planarity, and the second largest decrease in point cloud size over all tests. This effect was reduced by using a smaller aperture of f/4 (E2#19), and almost completely removed by using an aperture of f/8 (E2#21). These results show that increased distance of the focal point from the scanner center, the root thus being unfocused, and shallow DoF due to larger apertures reduce model quality. Their combined effect of unfocused setup and shallow DoF amplifies the decrease even further. The effect of an unfocused camera can, to a large extent, be compensated for by the large DoF stemming from a small aperture and vice versa, the effect of a shallow DoF can be compensated for by accurate focusing on the scanner center. Increasing the distance between cameras and the root resulted in the largest observed reduction in point cloud size and moving the root off-center on average improved features and reduced point cloud size, but the effect was driven by one root only.

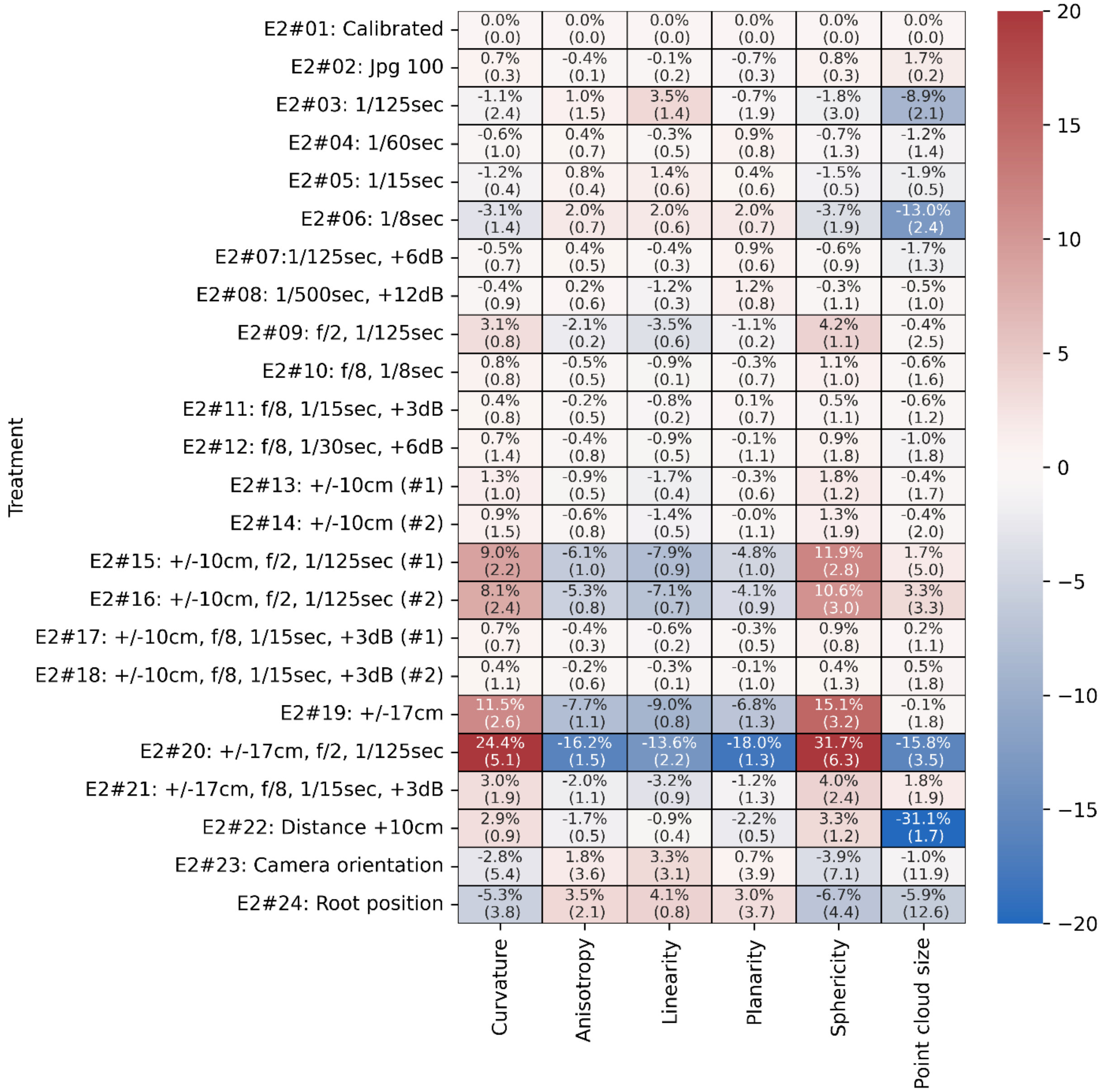

Treatment	Curvature	Anisotropy	Linearity	Planarity	Sphericity	Point cloud size
E2#01: Calibrated	0.0% (0.0)	0.0% (0.0)	0.0% (0.0)	0.0% (0.0)	0.0% (0.0)	0.0% (0.0)
E2#02: Jpg 100	0.7% (0.3)	-0.4% (0.1)	-0.1% (0.2)	-0.7% (0.3)	0.8% (0.3)	1.7% (0.2)
E2#03: 1/125sec	-1.1% (2.4)	1.0% (1.5)	3.5% (1.4)	-0.7% (1.9)	-1.8% (3.0)	-8.9% (2.1)
E2#04: 1/60sec	-0.6% (1.0)	0.4% (0.7)	-0.3% (0.5)	0.9% (0.8)	-0.7% (1.3)	-1.2% (1.4)
E2#05: 1/15sec	-1.2% (0.4)	0.8% (0.4)	1.4% (0.6)	0.4% (0.6)	-1.5% (0.5)	-1.9% (0.5)
E2#06: 1/8sec	-3.1% (1.4)	2.0% (0.7)	2.0% (0.6)	2.0% (0.7)	-3.7% (1.9)	-13.0% (2.4)
E2#07:1/125sec, +6dB	-0.5% (0.7)	0.4% (0.5)	-0.4% (0.3)	0.9% (0.6)	-0.6% (0.9)	-1.7% (1.3)
E2#08: 1/500sec, +12dB	-0.4% (0.9)	0.2% (0.6)	-1.2% (0.3)	1.2% (0.8)	-0.3% (1.1)	-0.5% (1.0)
E2#09: f/2, 1/125sec	3.1% (0.8)	-2.1% (0.2)	-3.5% (0.6)	-1.1% (0.2)	4.2% (1.1)	-0.4% (2.5)
E2#10: f/8, 1/8sec	0.8% (0.8)	-0.5% (0.5)	-0.9% (0.1)	-0.3% (0.7)	1.1% (1.0)	-0.6% (1.6)
E2#11: f/8, 1/15sec, +3dB	0.4% (0.8)	-0.2% (0.5)	-0.8% (0.2)	0.1% (0.7)	0.5% (1.1)	-0.6% (1.2)
E2#12: f/8, 1/30sec, +6dB	0.7% (1.4)	-0.4% (0.8)	-0.9% (0.5)	-0.1% (1.1)	0.9% (1.8)	-1.0% (1.8)
E2#13: +/-10cm (#1)	1.3% (1.0)	-0.9% (0.5)	-1.7% (0.4)	-0.3% (0.6)	1.8% (1.2)	-0.4% (1.7)
E2#14: +/-10cm (#2)	0.9% (1.5)	-0.6% (0.8)	-1.4% (0.5)	-0.0% (1.1)	1.3% (1.9)	-0.4% (2.0)
E2#15: +/-10cm, f/2, 1/125sec (#1)	9.0% (2.2)	-6.1% (1.0)	-7.9% (0.9)	-4.8% (1.0)	11.9% (2.8)	1.7% (5.0)
E2#16: +/-10cm, f/2, 1/125sec (#2)	8.1% (2.4)	-5.3% (0.8)	-7.1% (0.7)	-4.1% (0.9)	10.6% (3.0)	3.3% (3.3)
E2#17: +/-10cm, f/8, 1/15sec, +3dB (#1)	0.7% (0.7)	-0.4% (0.3)	-0.6% (0.2)	-0.3% (0.5)	0.9% (0.8)	0.2% (1.1)
E2#18: +/-10cm, f/8, 1/15sec, +3dB (#2)	0.4% (1.1)	-0.2% (0.6)	-0.3% (0.1)	-0.1% (1.0)	0.4% (1.3)	0.5% (1.8)
E2#19: +/-17cm	11.5% (2.6)	-7.7% (1.1)	-9.0% (0.8)	-6.8% (1.3)	15.1% (3.2)	-0.1% (1.8)
E2#20: +/-17cm, f/2, 1/125sec	24.4% (5.1)	-16.2% (1.5)	-13.6% (2.2)	-18.0% (1.3)	31.7% (6.3)	-15.8% (3.5)
E2#21: +/-17cm, f/8, 1/15sec, +3dB	3.0% (1.9)	-2.0% (1.1)	-3.2% (0.9)	-1.2% (1.3)	4.0% (2.4)	1.8% (1.9)
E2#22: Distance +10cm	2.9% (0.9)	-1.7% (0.5)	-0.9% (0.4)	-2.2% (0.5)	3.3% (1.2)	-31.1% (1.7)
E2#23: Camera orientation	-2.8% (5.4)	1.8% (3.6)	3.3% (3.1)	0.7% (3.9)	-3.9% (7.1)	-1.0% (11.9)
E2#24: Root position	-5.3% (3.8)	3.5% (2.1)	4.1% (0.8)	3.0% (3.7)	-6.7% (4.4)	-5.9% (12.6)

Figure 3.10: Heatmap of results from Experiment 2 showing effects of individual scanner settings on curvature, anisotropy, linearity, planarity, sphericity, and point cloud size. The first number represents the mean change in percent with respect to the calibrated scanner setup (E2#01) and the number in parentheses represents its standard deviation. Red colors indicate an increase and blue a decrease.

Discussion

Summary of findings

In this study, we created a methodical calibration pipeline to improve a multi-camera rig used for 3D reconstruction of plant roots. We then tested how camera calibration affected the quality of 3D reconstructions of maize root crowns, paying special attention to camera settings like focus, aperture, exposure time, and gain. Our results demonstrate that proper calibration of these settings significantly enhances the quality of reconstructed 3D models. Specifically, misalignment of the focal plane and shallow DoF led to increased noise and loss of fine root structures. Our results show how important it is to properly calibrate a scanner in order to improve the quality of a point cloud, lower noise, and make root trait extraction more reliable.

The results from Experiment 1 showed that using a properly calibrated scanner greatly improves the accuracy of 3D reconstructions. This was shown by higher linearity, planarity, and anisotropy values, as well as lower curvature and sphericity values. These improvements indicate a more structured and less noisy point cloud, which is critical for later steps of the analysis like root skeletonization and trait extraction. Furthermore, filtering using the SOR method, which is useful to remove outliers, had a relatively small effect compared to the benefits of proper scanner calibration. This suggests that reducing noise at the image acquisition stage is more effective than relying solely on post-processing steps.

Experiment 2 provided more detailed insights into the sensitivity of 3D reconstruction quality to individual camera settings. We observed that small deviations from the calibrated setup, such as slight changes in exposure time or gain, had minimal impact on point cloud quality. However, more substantial deviations, in particularly poor focus combined with a shallow DoF (achieved by using a large aperture), resulted in a severe decline in model quality. Interestingly, our results also demonstrated that increasing the DoF (by reducing the aperture size) could partially compensate for slight misfocusing. However, this trade-off required adjusting exposure time and gain to maintain proper image brightness. These findings underscore the importance of carefully selecting camera settings to optimize both sharpness and brightness while minimizing noise.

Comparison to other fields

The role of camera settings in 3D reconstruction is well understood in photogrammetry, yet its systematic evaluation in plant phenotyping remains limited. While proper camera calibration has been studied in forestry (Frey et al., 2018), archaeology (Bucchi et al., 2020; Novotny, 2019), and in the geosciences (Mosbrucker et al., 2017; O'Connor et al., 2017), plant phenotyping presents unique challenges. Unlike forestry and remote sensing, where large-scale features dominate and motion blur is a primary concern due to the fast movement of camera, root phenotyping deals with small, highly occluded structures, making DoF and focus calibration critical. Studies in archaeology (Nicolae et al., 2014) and small object reconstruction (Gallo et al., 2014; Menna et al., 2017) also emphasize DoF as a major limitation in close-range photogrammetry. However, these studies often suggest focus stacking or tilt-shift lenses as solutions, which may not be feasible for high-throughput plant phenotyping due to time constraints and system complexity.

Our results align with recommendations from these fields, particularly in emphasizing manual focus control, optimizing the exposure triangle (gain/ISO, exposure time, aperture), and maintaining consistency in scanning geometry. However, root phenotyping requires additional considerations, such as accounting for organic structures with varying surface properties and fine root details, which are more sensitive to poor calibration than rigid objects in archaeological photogrammetry.

Limitations and Future Work

Despite these findings, some limitations in our research remain. First, our study did not evaluate the effects of intrinsic and extrinsic calibration (e.g., focal length, lens distortion, and camera poses), as this was handled automatically by COLMAP. Future work could explore how manual intrinsic and extrinsic calibration using calibration boards compares with automated methods in terms of reconstruction accuracy.

A second limitation of this study is that we did not explicitly test the effects of diffraction at very small apertures (e.g., f/11–f/16), which could reduce sharpness due to light wave interference (Gallo et al., 2014; Martins et al., 2015). While our findings suggest f/4 to f/8 as an optimal range, future work could systematically analyze the diffraction limit in plant phenotyping setups. Additionally, light distribution was not fully explored, which could introduce artifacts in 3D reconstructions, a factor that may also influence phenotyping workflows. Future research could test controlled lighting environments to further optimize 3D scanning conditions.

Additionally, while our results demonstrate that a calibrated setup produces more reliable point clouds, further validation with different plant species and environmental conditions is needed to assess the generalizability of our findings. Moreover, variations in point cloud density might influence k-nearest neighbor calculations used for feature extraction, which should be considered in future studies. Finally, this study demonstrates that scanner calibration significantly improves 3D model quality, but we did not explicitly assess its impact on root trait measurements, such as root length, diameter, or volume, which should be investigated in future studies to fully understand the biological implications of improperly setup calibrated camera setups.

Conclusions

In this study, we developed and validated a camera calibration pipeline aimed at improving the accuracy and reproducibility of 3D root phenotyping. Our results show that careful adjustment of focus, aperture, and exposure settings significantly improves model accuracy, and that calibration has a stronger effect on point cloud quality than post-processing filters alone. Furthermore, we identified the most critical factors affecting reconstruction accuracy, with poor focus and a shallow DoF being the most detrimental. Importantly, we demonstrated that increasing DoF can mitigate the effects of slight misfocusing, providing practical guidelines for optimizing camera settings in future studies.

Our findings contribute to the broader effort of improving transparency and reproducibility in plant phenotyping. By providing a structured calibration workflow, we aim to assist researchers in setting up robust imaging pipelines that produce high-quality 3D models. Future research should explore additional calibration factors, such as intrinsic and extrinsic parameter refinement and different lighting conditions, to further enhance the robustness of 3D root phenotyping methodologies. Ultimately, improved imaging practices will facilitate more precise quantification of root traits, advancing our understanding of plant growth and resilience in diverse environments.

Declarations

Ethics approval and consent to participate

Not applicable.

Consent for publication

Not applicable.

Availability of data and materials

All data used in the manuscript is available in the BioImage Archive under the DOI: 10.6019/S-BIAD1690

Competing interests

The authors declare that they have no competing interests.

Funding

The research was supported by the NSF CAREER Award No. 2329282 and by the USDOE ARPA-E ROOTS Award Number DE-AR0000821 to A.B. Any opinions, findings, and conclusions or recommendations expressed in this material are those of the authors and do not necessarily reflect the views of the National Science Foundation or the US Department of Energy.

Authors' contributions

P.P., S.L. and A.B. conceived the calibration pipeline, experiments, algorithms, and data analysis. P.P. and A.B. wrote the original manuscript. P.P. collected data, implemented algorithms and performed data analysis. All authors reviewed and edited the manuscript. AB conceived the project and acquired funding.

Acknowledgements

The work was conducted while transitioning institutions for AB and SL (University of Georgia to University of Arizona).

References

Bao, Y., Tang, L., Srinivasan, S., & Schnable, P. S. (2019). Field-based architectural traits characterisation of maize plant using time-of-flight 3D imaging. *BIOSYSTEMS ENGINEERING*, *178*, 86-101. https://doi.org/10.1016/j.biosystemseng.2018.11.005

Boogaard, F. P., van Henten, E. J., & Kootstra, G. (2023). The added value of 3D point clouds for digital plant phenotyping – A case study on internode length measurements in cucumber. *BIOSYSTEMS ENGINEERING*, *234*, 1-12. https://doi.org/10.1016/j.biosystemseng.2023.08.010

Bucchi, A., Luengo, J., Fuentes, R., Arellano-Villalón, M., & Lorenzo, C. (2020). Recommendations for Improving Photo Quality in Close Range Photogrammetry, Exemplified in Hand Bones of Chimpanzees and Gorillas. *International Journal of Morphology*, *38*(2), 348-355. <Go to ISI>://WOS:000511087000018

Bucksch, A., Atta-Boateng, A., Azihou, A. F., Battogtokh, D., Baumgartner, A., Binder, B. M., Braybrook, S. A., Chang, C., Coneva, V., DeWitt, T. J., Fletcher, A. G., Gehan, M. A., Diaz-Martinez, D. H., Hong, L. L., Iyer-Pascuzzi, A. S., Klein, L. L., Leiboff, S., Li, M., Lynch, J. P., . . . Chitwood, D. H. (2017). Morphological Plant Modeling: Unleashing Geometric and Topological Potential within the Plant Sciences. *Frontiers in Plant Science*, *8*, Article 900. https://doi.org/10.3389/fpls.2017.00900

Bucksch, A., Burridge, J., York, L. M., Das, A., Nord, E., Weitz, J. S., & Lynch, J. P. (2014). Image-based high-throughput field phenotyping of crop roots. *Plant Physiol*, *166*(2), 470-486. https://doi.org/10.1104/pp.114.243519

Chéné, Y., Rousseau, D., Lucidarme, P., Bertheloot, J., Caffier, V., Morel, P., Belin, É., & Chapeau-Blondeau, F. (2012). On the use of depth camera for 3D phenotyping of entire plants. *Computers and Electronics in Agriculture*, *82*, 122-127. https://doi.org/10.1016/j.compag.2011.12.007

Claussen, J., Wittenberg, T., Uhlmann, N., & Gerth, S. (2023). "Chamber #8" - a holistic approach of high-throughput non-destructive assessment of plant roots. *Front Plant Sci*, *14*, 1269005, Article 1269005. https://doi.org/10.3389/fpls.2023.1269005

CloudCompare. In. (2022). (Version 2.12.4) [GPL software]. https://www.danielgm.net/cc/

Daviet, B., Fernandez, R., Cabrera-Bosquet, L., Pradal, C., & Fournier, C. (2022). PhenoTrack3D: an automatic high-throughput phenotyping pipeline to track maize organs over time. *Plant Methods*, *18*(1), 130, Article 130. https://doi.org/10.1186/s13007-022-00961-4

de la Iglesia Castro, D., Mader, K., Hanchen, Sullivan, B., pandu-rao, Sebastian, Cole, J., Wallbaum, M., Mitchell, N., Movva, M., McCartney, P., Jadhav, S., Miguel, Y. B. d., Milan, A., Mitzkus, B., Bazazian, D., Gandenberger, G., Buchanan, J., Trevisani, M. D., . . . nokonoko1203. (2022). *daavoo/pyntcloud: v0.3.1*. In (Version v0.3.1) Zenodo. https://doi.org/10.5281/zenodo.6945370

Dhondt, S., Wuyts, N., & Inze, D. (2013). Cell to whole-plant phenotyping: the best is yet to come. *Trends Plant Sci*, *18*(8), 428-439. https://doi.org/10.1016/j.tplants.2013.04.008

Duncan, K. E., Czymmek, K. J., Jiang, N., Thies, A. C., & Topp, C. N. (2022). X-ray microscopy enables multiscale high-resolution 3D imaging of plant cells, tissues, and organs. *Plant Physiol*, *188*(2), 831-845. https://doi.org/10.1093/plphys/kiab405

Eltner, A., & Sofia, G. (2020). Structure from motion photogrammetric technique. In P. Tarolli & S. M. Mudd (Eds.), *Remote Sensing of Geomorphology* (Vol. 23, pp. 1-24). Elsevier. https://doi.org/10.1016/b978-0-444-64177-9.00001-1

Fiorani, F., & Schurr, U. (2013). Future scenarios for plant phenotyping. *Annu Rev Plant Biol*, *64*, 267-291. https://doi.org/10.1146/annurev-arplant-050312-120137

Frey, J., Kovach, K., Stemmler, S., & Koch, B. (2018). UAV Photogrammetry of Forests as a Vulnerable Process. A Sensitivity Analysis for a Structure from Motion RGB-Image Pipeline. *Remote Sensing*, *10*(6), Article 912. https://doi.org/10.3390/rs10060912

Gallo, A., Muzzupappa, M., & Bruno, F. (2014). 3D reconstruction of small sized objects from a sequence of multi-focused images. *Journal of Cultural Heritage*, *15*(2), 173-182. https://doi.org/10.1016/j.culher.2013.04.009

Li, M. H., Shamshiri, R. R., Schirrmann, M., & Weltzien, C. (2021). Impact of Camera Viewing Angle for Estimating Leaf Parameters of Wheat Plants from 3D Point Clouds. *Agriculture-Basel*, *11*(6), Article 563. https://doi.org/10.3390/agriculture11060563

Li, Z., Guo, R., Li, M., Chen, Y., & Li, G. (2020). A review of computer vision technologies for plant phenotyping. *Computers and Electronics in Agriculture*, *176*, Article 105672. https://doi.org/10.1016/j.compag.2020.105672

Liang, R., Xu, S. Y., & Soc, I. C. (2020, Nov 29-Dec 01). Three-Dimensional Reconstruction and Phenotype Nondestructive Measurement Technology for Rape Roots.*IEEE International Conference on Distributed Computing Systems* [2020 ieee 40th international conference on distributed computing systems (icdcs)]. 40th IEEE International Conference on Distributed Computing Systems (ICDCS), Electr Network.

Lin, Y. (2015). LiDAR: An important tool for next-generation phenotyping technology of high potential for plant phenomics? *Computers and Electronics in Agriculture*, *119*, 61-73. https://doi.org/10.1016/j.compag.2015.10.011

Liu, S., Acosta-Gamboa, L., Huang, X., & Lorence, A. (2017). Novel Low Cost 3D Surface Model Reconstruction System for Plant Phenotyping. *JOURNAL OF IMAGING*, *3*(3), Article 39. https://doi.org/10.3390/jimaging3030039

Liu, S., Bonelli, W. P., Pietrzyk, P., & Bucksch, A. (2023). Comparison of open-source three-dimensional reconstruction pipelines for maize-root phenotyping. *The Plant Phenome Journal*, *6*(1), e20068.

Liu, S. X., Barrow, C. S., Hanlon, M., Lynch, J. P., & Bucksch, A. (2021). DIRT/3D: 3D root phenotyping for field-grown maize (Zea mays). *Plant Physiology*, *187*(2), 739-757. https://doi.org/10.1093/plphys/kiab311

Lobet, G. (2017). Image Analysis in Plant Sciences: Publish Then Perish. *Trends Plant Sci*, *22*(7), 559-566. https://doi.org/10.1016/j.tplants.2017.05.002

Lu, X. T., Ono, E., Lu, S., Zhang, Y., Teng, P. C., Aono, M., Shimizu, Y., Hosoi, F., & Omasa, K. (2020). Reconstruction method and optimum range of camera-shooting angle for 3D plant modeling using a multi-camera photography system. *Plant Methods*, *16*(1), Article 118. https://doi.org/10.1186/s13007-020-00658-6

Luhmann, T., Fraser, C., & Maas, H.-G. (2016). Sensor modelling and camera calibration for close-range photogrammetry. *Isprs Journal of Photogrammetry and Remote Sensing*, *115*, 37-46. https://doi.org/10.1016/j.isprsjprs.2015.10.006

Lynch, J. P. (2019). Root phenotypes for improved nutrient capture: an underexploited opportunity for global agriculture. *New Phytologist*, *223*(2), 548-564. https://doi.org/10.1111/nph.15738

Martins, A. F., Bessant, M., Manukyan, L., & Milinkovitch, M. C. (2015). R2OBBIE-3D, a Fast Robotic High-Resolution System for Quantitative Phenotyping of Surface Geometry and Colour-Texture. *PLoS One*, *10*(6), Article e0126740. https://doi.org/10.1371/journal.pone.0126740

Menna, F., Nocerino, E., Morabito, D., Farella, E. M., Perini, M., & Remondino, F. (2017). An open source low-cost automatic system for image-based 3D digitization. *The International Archives of the Photogrammetry, Remote Sensing and Spatial Information Sciences*, *42*, 155-162.

Mosbrucker, A. R., Major, J. J., Spicer, K. R., & Pitlick, J. (2017). Camera system considerations for geomorphic applications of SfM photogrammetry. *Earth Surface Processes and Landforms*, *42*(6), 969-986. https://doi.org/10.1002/esp.4066

Nguyen, C. V., Fripp, J., Lovell, D. R., Furbank, R., Kuffner, P., Daily, H., & Sirault, X. (2016). 3D Scanning System for Automatic High-Resolution Plant Phenotyping. *2016 International Conference on Digital Image Computing: Techniques and Applications (Dicta)*, 148-155. <Go to ISI>://WOS:000391534900023

Nicolae, C., Nocerino, E., Menna, F., & Remondino, F. (2014). Photogrammetry applied to problematic artefacts. *The International Archives of the Photogrammetry, Remote Sensing and Spatial Information Sciences*, *40*, 451-456.

Novotny, A. C. (2019). Implementing Photogrammetry in Three Bioarchaeological Contexts: Steps for In-Field Documentation. *Advances in Archaeological Practice*, *7*(1), 87-96. https://doi.org/10.1017/aap.2018.45

O'Connor, J., Smith, M. J., & James, M. R. (2017). Cameras and settings for aerial surveys in the geosciences. *Progress in Physical Geography: Earth and Environment*, *41*(3), 325-344. https://doi.org/10.1177/0309133317703092

Paez-Garcia, A., Motes, C. M., Scheible, W. R., Chen, R., Blancaflor, E. B., & Monteros, M. J. (2015). Root Traits and Phenotyping Strategies for Plant Improvement [article]. *Plants (Basel)*, *4*(2), 334-355. https://doi.org/10.3390/plants4020334

Paulus, S. (2019). Measuring crops in 3D: using geometry for plant phenotyping. *Plant Methods*, *15*(1), Article 103. https://doi.org/10.1186/s13007-019-0490-0

Pietrzyk, P., Phan-Udom, N., Chutoe, C., Pingault, L., Roy, A., Libault, M., Saengwilai, P. J., & Bucksch, A. (2024). DIRT/µ: automated extraction of root hair traits using combinatorial optimization. *Journal of Experimental Botany*, *76*(2), 285-298. https://doi.org/10.1093/jxb/erae385

Pound, M. P., Atkinson, J. A., Townsend, A. J., Wilson, M. H., Griffiths, M., Jackson, A. S., Bulat, A., Tzimiropoulos, G., Wells, D. M., Murchie, E. H., Pridmore, T. P., & French, A. P. (2017). Deep machine learning provides state-of-the-art performance in image-based plant phenotyping. *Gigascience*, *6*(10), 1-10. https://doi.org/10.1093/gigascience/gix083

Remondino, F., & Fraser, C. (2006). Digital camera calibration methods: considerations and comparisons. *International Archives of the Photogrammetry, Remote Sensing and Spatial Information Sciences*, *36*(5), 266-272.

Rossi, R., Costafreda-Aumedes, S., Leolini, L., Leolini, C., Bindi, M., & Moriondo, M. (2022). Implementation of an algorithm for automated phenotyping through plant 3D-modeling: A practical application on the early detection of water stress. *Computers and Electronics in Agriculture*, *197*, Article 106937. https://doi.org/10.1016/j.compag.2022.106937

Rossi, R., Leolini, C., Costafreda-Aumedes, S., Leolini, L., Bindi, M., Zaldei, A., & Moriondo, M. (2020). Performances Evaluation of a Low-Cost Platform for High-Resolution Plant Phenotyping. *Sensors*, *20*(11), Article 3150. https://doi.org/10.3390/s20113150

Salter, W. T., Shrestha, A., & Barbour, M. M. (2021). Open source 3D phenotyping of chickpea plant architecture across plant development. *Plant Methods*, *17*(1), Article 95. https://doi.org/10.1186/s13007-021-00795-6

Schönberger, J., Frahm, J., & IEEE. (2016, 2016-01-01). Structure-from-Motion Revisited. 2016 IEEE Conference in Computer Vision and Pattern Recodgnition (CVPR),

Sun, S., Li, C., Paterson, A. H., Jiang, Y., Xu, R., Robertson, J. S., Snider, J. L., & Chee, P. W. (2018). In-field High Throughput Phenotyping and Cotton Plant Growth Analysis Using LiDAR. *Front Plant Sci*, *9*, 16, Article 16. https://doi.org/10.3389/fpls.2018.00016

Sunvittayakul, P., Kittipadakul, P., Wonnapinij, P., Chanchay, P., Wannitikul, P., Sathitnaitham, S., Phanthanong, P., Changwitchukarn, K., Suttangkakul, A., Ceballos, H., & Vuttipongchaikij, S. (2022). Cassava root crown phenotyping using three-dimension (3D) multi-view stereo reconstruction. *Scientific Reports*, *12*(1), Article 10030. https://doi.org/10.1038/s41598-022-14325-4

Topp, C. N., Iyer-Pascuzzi, A. S., Anderson, J. T., Lee, C. R., Zurek, P. R., Symonova, O., Zheng, Y., Bucksch, A., Mileyko, Y., Galkovskyi, T., Moore, B. T., Harer, J., Edelsbrunner, H., Mitchell-Olds, T., Weitz, J. S., & Benfey, P. N. (2013). 3D phenotyping and quantitative trait locus mapping identify core regions of the rice genome controlling root architecture. *Proc Natl Acad Sci U S A*, *110*(18), E1695-1704. https://doi.org/10.1073/pnas.1304354110

Tracy, S. R., Nagel, K. A., Postma, J. A., Fassbender, H., Wasson, A., & Watt, M. (2020). Crop Improvement from Phenotyping Roots: Highlights Reveal Expanding Opportunities. *Trends Plant Sci*, *25*(1), 105-118. https://doi.org/10.1016/j.tplants.2019.10.015

Uhrmann, F., Seifert, L., Scholz, O., Schmitt, P., & Greiner, G. (2011). Improving Sheet-of-light based Plant Phenotyping with Advanced 3D Simulation. In A. Heuberger, G. Elst, & R. Hanke (Eds.), *Microelectronic Systems* (pp. 253-263). Springer Berlin Heidelberg. https://doi.org/10.1007/978-3-642-23071-4_24

Walter, A., Liebisch, F., & Hund, A. (2015). Plant phenotyping: from bean weighing to image analysis. *Plant Methods*, *11*, 14, Article 14. https://doi.org/10.1186/s13007-015-0056-8

Wu, S., Wen, W., Wang, Y., Fan, J., Wang, C., Gou, W., & Guo, X. (2020). MVS-Pheno: A Portable and Low-Cost Phenotyping Platform for Maize Shoots Using Multiview Stereo 3D Reconstruction. *Plant Phenomics*, *2020*, 1848437, Article 1848437. https://doi.org/10.34133/2020/1848437

Zhang, Z., Sun, W., Min, X., Wang, T., Lu, W., & Zhai, G. (2022). No-Reference Quality Assessment for 3D Colored Point Cloud and Mesh Models. *Ieee Transactions on Circuits and Systems for Video Technology*, *32*(11), 7618-7631. https://doi.org/10.1109/tcsvt.2022.3186894

CHAPTER 4

RESOLVING INTERSECTING ROOTS IN 3D SKELETONS FOR ACCURATE ROOT TRAIT QUANTIFICATION

Introduction

Understanding root system architecture is fundamental to agricultural crops, as roots govern water and nutrient uptake and therefore resistance to drought and nutrient limited soils. Due to the increasing interest in breeding crops for improved root traits, accurate and precise root phenotyping has become crucial. Three-dimensional (3D) imaging methods such as Structure-from-Motion (SfM) and X-ray computed tomography (CT) have significantly advanced root phenotyping by enabling reconstruction of root systems (Claussen et al., 2023; Liu et al., 2021; Shao et al., 2021). These advances have allowed researchers to quantify 3D roots traits, including root length, root angles, diameter and number of roots. However, these methods often produce skeletons of the root system, which reduce the digital root models, often point clouds or voxels, into graph representations. These graphs, which consist of nodes with information of their 3D location and edges connecting these nodes, serve as simple models for the root system architecture (Bucksch, 2014). However, these skeletons often contain topological errors, often caused by the proximity of intersecting or overlapping roots, which cannot be resolved into individual structures during skeletonization and therefore form cycles, which are closed loops in the skeleton graph where there is more than one path between certain nodes (Bucksch, 2014; Zeng et al., 2021).

Therefore, a particularly difficult aspect in extracting topological information from 3D root skeletons for root system architecture phenotyping is the accurate inference of the branching topology. In this context, the branching topology is the hierarchical tree-like structure through which the root system develops roots into the soil. An accurate root skeleton is therefore an acyclic graph (i.e. a tree), such that each root segment can be traced along a unique path from the origin of the skeleton, which is the transition from stem to the root. This assumption, however, is violated when roots intersect and therefore form cycles in the data. As a result, the physical connectivity between roots is misinterpreted, which leads to wrong assignment of root connectivity and root hierarchy. For example, two intersecting lateral roots form a single merged structure in the imperfect skeleton of the root system, making measurements of their root length, angle, and density impossible. Because traits such as lateral root length and density are related to important root functions, such as drought tolerance and nitrogen and phosphorus acquisition (Lynch, 2013; Postma et al., 2014; Zhan et al., 2015), errors in root topology measurements might lead to wrong conclusions in studies. Therefore, it is essential to resolve topological ambiguities due to intersecting roots to link root system architecture traits to environmental and genotypic factors.

In this study, we present an algorithm to resolve intersecting roots in 3D root skeletons, which builds upon the heuristic of the DIRT/µ algorithm (Pietrzyk et al., 2024), which we previous applied to resolve intersecting root hairs in 2D images. Our method uses skeletons extracted from point clouds and applies a combinatorial optimization procedure that identifies individual roots and resolves intersections. By dividing the skeleton into smaller segments and fitting splines that span multiple segments, we create potential candidates for roots. Based on a priori rules we select the candidates that adhere best to structurally plausible configurations. This step enables us to assemble skeletons that closely resemble the hierarchical topology of the root system. We test our algorithm on eight skeletons of soybean roots, present examples of resolved roots as well as a first statistical analysis on the number of roots.

Materials and Methods

The presented algorithm works through sequential steps that start with the segmentation of a 3D root skeleton and results in the detection of individual roots within the root system, resolving any intersections between two or more roots. The method is built on the algorithm used in DIRT/μ, with modifications to work on 3D skeletons and to reassemble the structure of a root. First, a 3D skeleton with root diameter information (Figure 4.1) of a root system is divided into small segments representing root segments between root junction points (Figure 4.2A,B). Next, we fit splines to the skeleton spanning one or more segments, where each point of the spline has an associated weight influencing the curve's shape (Figure 4.2C). Similar to the idea of DIRT/μ, the algorithm tests whether combinations of these splines adhere to a priori criteria of the root system architecture to compute iteratively a set of roots. The selected solution is the set of roots that best resemble the complete root system architecture.

The algorithm starts with a 3D skeleton of a root as input. Each point in the skeleton has a 3D coordinate and a value for the local radius of the skeleton, approximating half the diameter of the root (Figure 4.1B). Points are connected to their neighboring points and belong to one of the same three types as in DIRT/μ: (i) termination points with only one neighbor; (ii) axis segments, if points with exactly two neighbors form continuous lines; and (iii) junction points with more than two neighbors forming branching points. A relational graph of skeleton segments is then computed in the same way as in DIRT/μ, where nodes are embedded at the locations of the termination and junction points (Figure 4.2A). The origin of the skeleton is the node that marks the transition from the stem to the root and has index zero. Each individual tip, junction and axis segment represents an individual component in the skeleton containing the locations of points (Figure 4.2B).

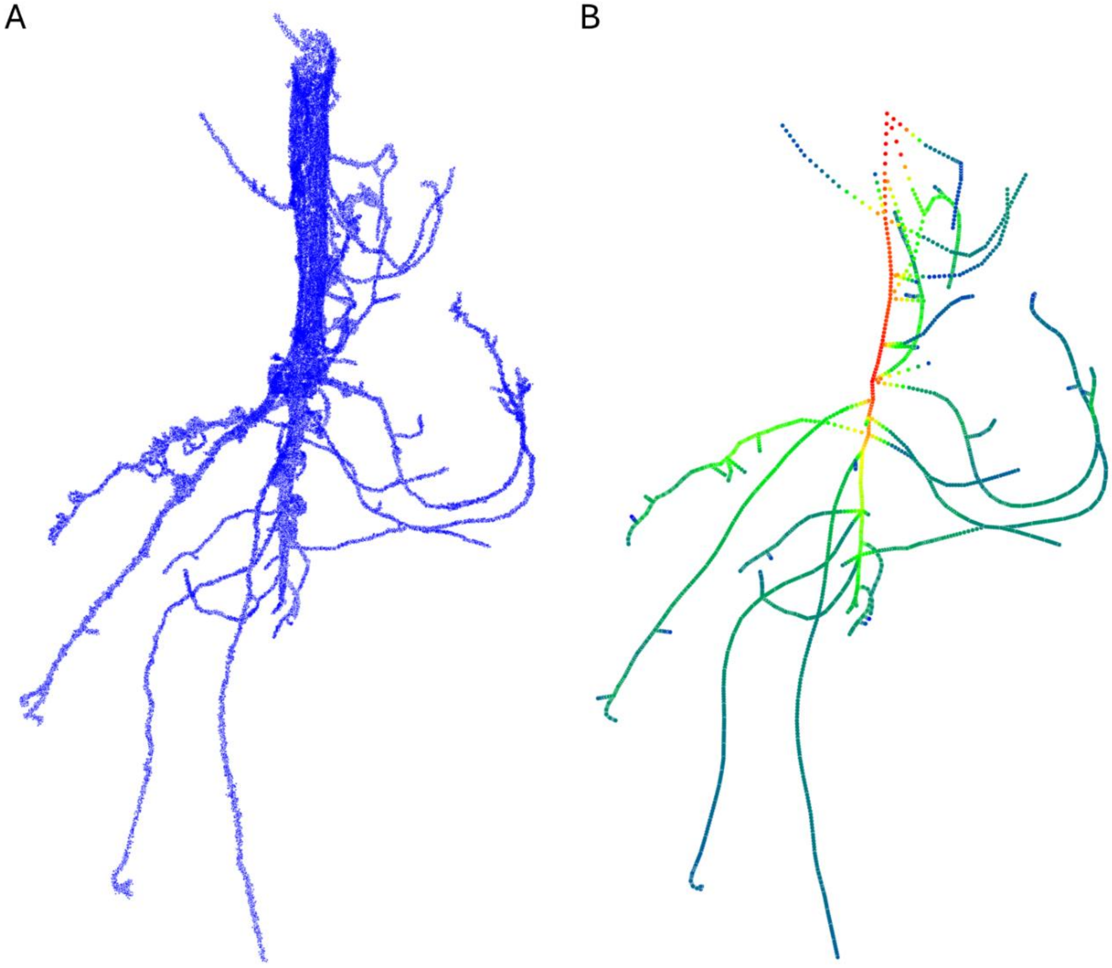

Figure 4.1: Image of raw point cloud and skeleton with radius of root. (A) The image of the raw point cloud of root 1. (B) Image of the skeleton corresponding to the point cloud of root 1. Red colors indicate a larger radius, while blue indicates a smaller radius.

Based on the skeleton and relational graph, we create candidates for individual roots (Figure 4.2C). Each candidate is created by traversing a path from one node to another along the relational graph. By traversing multiple paths, we obtain a set of candidates that span the whole

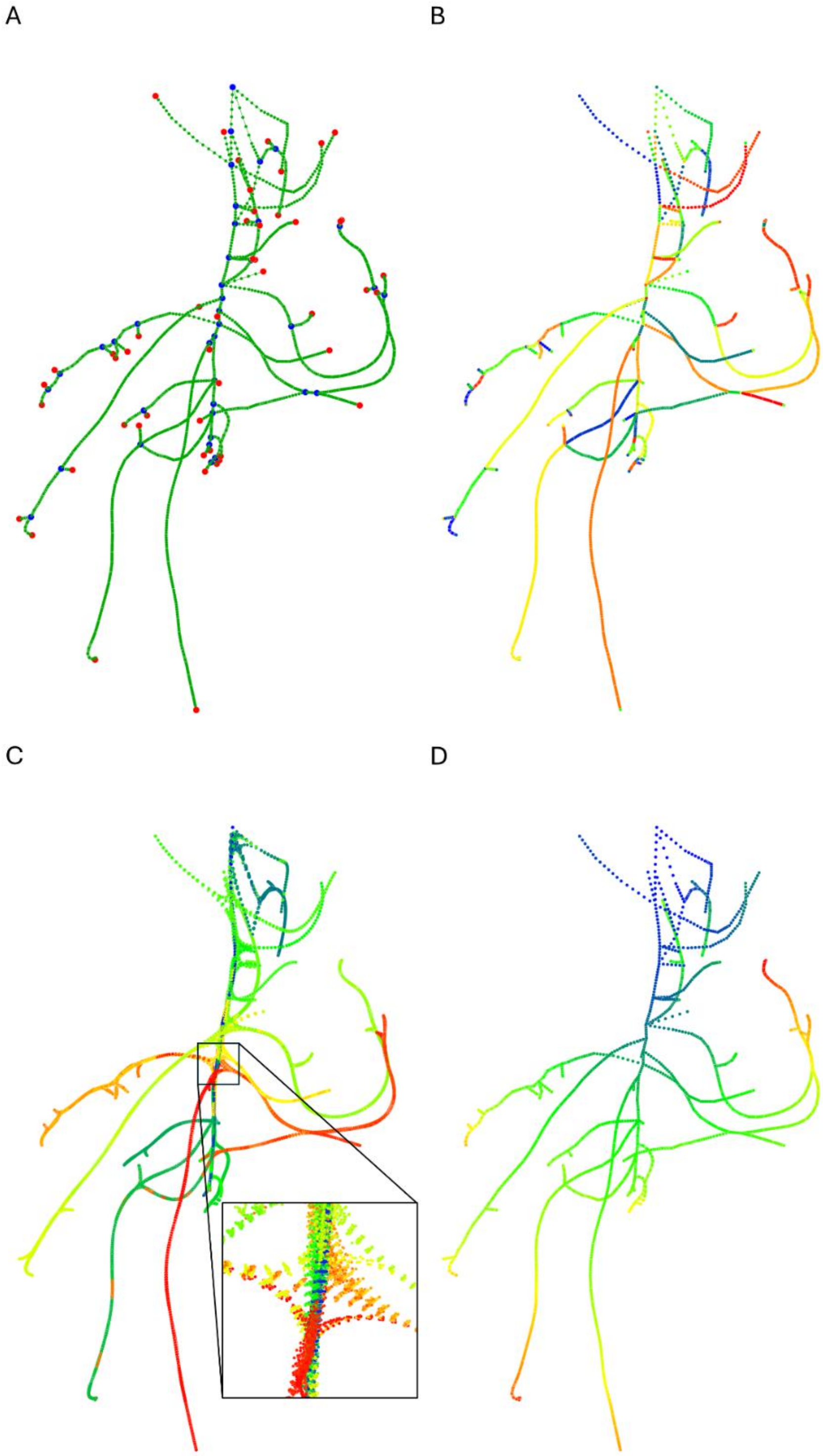

Figure 4.2: Overview of steps in algorithm to resolve roots. (A) Skeleton highlighting different types of nodes. Tips are shown in red, junctions in blue and axis segments in green. (B) Segmented components of the skeleton. Each segment is indicated by a different color. (C) Pool of root candidates that is used during optimization. (D) Geodesic distance from the origin node at the top. Blue indicates small distance, while nodes further away from the origin are red.

skeletons. A smooth line is then fitted to the 3D points on each path. We use a weighted spline fitting method, adapted from DIRT/µ, to remove artifacts at junctions of the skeleton and represent the root more accurately. As such we base the weights of the spline on the radius of the skeleton using the equation:

$$w = 5/r_{skeleton}$$

in which $r_{skeleton}$ is the local radius of skeleton. The inverse of the weight function is the standard deviation of the error we expect in the coordinates of the skeleton points, where the factor of five was selected after visual inspection to provide a good amount of smoothing for all radii. The algorithm then reduces the number of candidates, in the same way as in DIRT/µ, by removing candidates that have excessive curvature.

The remaining 3D splines will touch one another or overlap partially in the same way they do in 2D images. Therefore, we adopted the relationships between splines from DIRT/µ. In summary, (i) splines that overlap or intersect in an invalid manner result in conflicting relationships, (ii) all remaining splines either do not touch, or they intersect or overlap in a valid manner, and (iii) splines that overlap at one end are merged.

We further applied the same combinatorial optimization method from DIRT/µ, which is based on simulated annealing with restored feasibility at each move and automated parametrization to determine an optimal solution (Abramson et al., 1996; Kirkpatrick et al., 1983; Orsila et al., 2008). This is accomplished by iteratively selecting different configurations of splines that best reconstruct the complete root system architecture. We quantify the cost of each such configuration as a function of four parameters that were adapted from DIRT/µ (see Table 4.1).

1. *Residual total curvature* $K_{residual}$ (adopted from DIRT/μ): We minimize the residual spline curvature of all candidates in a least squares sense to avoid candidates with excessive curvature.
2. *Incompleteness* $R_{incomplete}$ (adopted from DIRT/μ): We minimize the ratio between the length of all unresolved skeleton axis segments ($l_{unresolved\ skeleton}$) and the total length of all skeleton axis segments ($l_{skeleton}$) to quantify the degree of identified roots.
3. *Minimum geodesic distance* $D_{geodesic}$: We minimize the difference of the smallest geodesic distance from both tips of the root axis and from the whole root axis to ensure that branching points occur near the minimum geodesic distance of the root.
4. *Topology index* $I_{topology}$: We ensure that each root's topology is correct. Thus one end of the root must correspond to a branching point and the other to a tip in the skeleton. Additionally, the number of found roots must equal the number of tips in the skeleton to avoid over-segmentation. Thus, we minimize the difference between the number of roots with correct topology and the number of tips. Further, we minimize the difference between the number of tips in the skeleton and the number of detected roots.

The total cost of each state is computed as the root-mean-square of all four metrics (Table 4.1). Using simulated annealing this cost is minimized, such that intersecting roots are resolved and the topology of the resulting roots closely resembles that of the root system architecture.

Table 4.1: Overview of optimization metrics.

	Values	Normalized values	Explanations
Residual total curvature	$\mathrm{K}_{\mathrm{residual}} = \sqrt{\frac{1}{\mathrm{n}}\sum_{\mathrm{i}=1}^{\mathrm{n}} \kappa_{\mathrm{i}}^{2}}$	$\widetilde{\mathrm{K}}_{\mathrm{residual}} = \frac{\mathrm{K}_{\mathrm{residual}}}{\mathrm{K}_{\mathrm{max}}}$	*n* is number of candidates; κ_i is residual spline curvature of candidate *i*; K_{max} equals avg. of all residual total curvatures.
Incompleteness	$\mathrm{R}_{\mathrm{incomplete}} = 1 - \frac{\mathrm{l}_{\mathrm{unresolved\ MA}}}{\mathrm{l}_{\mathrm{MA}}}$	$\widetilde{\mathrm{R}}_{\mathrm{incomplete}} = \mathrm{R}_{\mathrm{incomplete}}$	l_{MA} is length of all medial axis segments; $l_{unresolved\ MA}$ is the length of medial axis segments that are unresolved.
Minimum geodesic distance	$\mathrm{D}_{\mathrm{geodesic}} = \frac{1}{\mathrm{n}}\sum_{\mathrm{i}=1}^{\mathrm{n}} \max(0, \mathrm{D}_{\mathrm{tip\ i}} - \mathrm{D}_{\mathrm{candidate\ i}})$	$\widetilde{\mathrm{D}}_{\mathrm{geodesic}} = \frac{\mathrm{D}_{\mathrm{geodesic}}}{\mathrm{D}_{\mathrm{mean}}}$	*n* is number of candidates; $D_{tip\ i}$ is smallest geodesic distance of tips of candidate *i*; $D_{candidate\ i}$ is smallest geodesic distance in candidate *i*; D_{mean} is the average value of $D_{geodesic}$ in random states
Topology index	$I_{topology} = \frac{1}{2\sqrt{n_{tips}}}\left(\left\|n_{tips} - n_{tip+junction}\right\| + \left\|n_{tips} - n\right\|\right)$	$\tilde{I}_{topology} = I_{topology}$	n_{tips} is the number of tips in the skeleton; $n_{tip+junction}$ is the number of roots, whose endpoints correspond to a tip and a junction in skeleton; *n* is number of detected roots
Total cost	$\mathrm{cost} = \sqrt{\widetilde{\mathrm{K}}_{\mathrm{resisual}}^{2} + \widetilde{\mathrm{R}}_{\mathrm{incomplete}}^{2} + \widetilde{\mathrm{D}}_{\mathrm{geodesic}}^{2} + \tilde{\mathrm{I}}_{\mathrm{topology}}^{2}}$		

We then used 3D skeletons of eight soybean roots with various levels of complexity to test the algorithm (Figure 4.3) from a study by Carpenter et al. (2023). Because root segments in the original skeletons were cut at locations where cycles occurred due to intersecting roots, we manually added points to the skeletons to close these cycles. We further interpolated five additional points between the original points of the skeleton to aid the spline fitting. As such, all skeletons in the dataset have at least one intersection that had to be resolved.

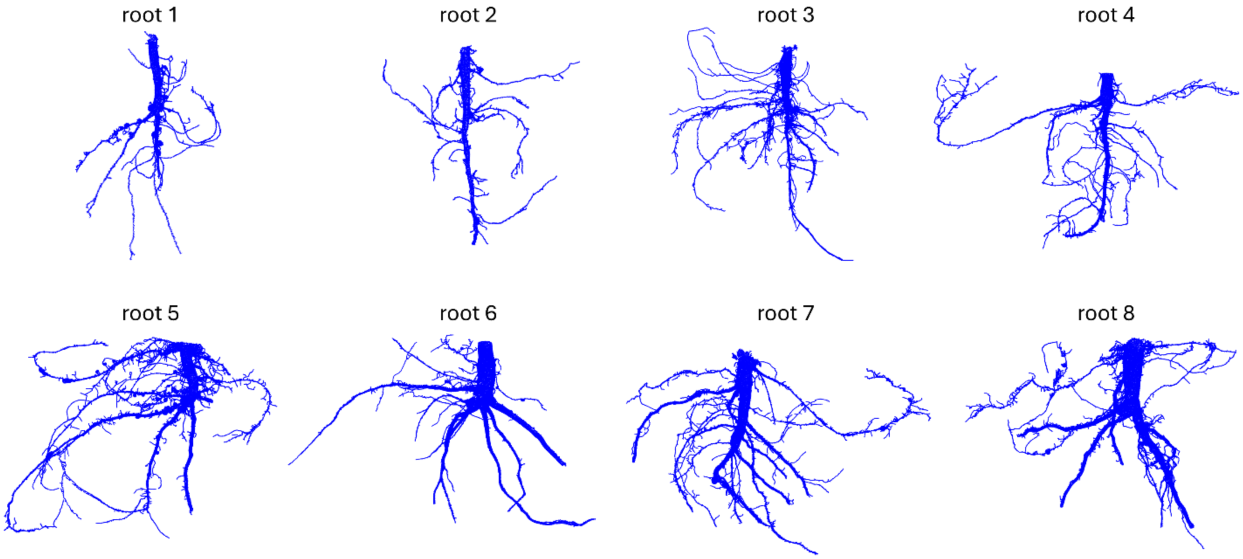

Figure 4.3: Images of point clouds of eight soybean roots.

Results

The roots, that were exported after processing the root skeletons, revealed that intersections between roots have been resolved in most cases. In root 1, as shown in Figure 4.4, we were able to resolve both intersections. Here the roots that cause cycle 1 intersect in a nearly perpendicular manner, such that only one node in the skeleton is shared by both roots Figure 4.4B. In contrast, the intersecting roots that form cycle 2 share a longer segment of the skeleton, resembling a more challenging intersection to resolve. While both intersections have been resolved correctly, we noticed that a few roots in the results were over-segmented, and a few root segments were excluded completely from the solution.

We further assessed results related to our topology index $I_{topology}$ and the completeness of the solution (Table 4.2). First, we noticed that the number of roots were detected, that have one end corresponding to a junction in the skeleton and the other end corresponding to a tip in the skeleton, matches the number of tips in six out of eight skeletons. However, in all skeletons we detected overall slightly more roots, which can have junction-junction, junction-tip or tip-tip correspondence to the skeleton, than there were tips in the skeletons, indicating that our results are slightly over-segmented (Figure 4.4). Finally, we observed that all skeletons were not completely resolved, with an average of 1.1% remaining unresolved.

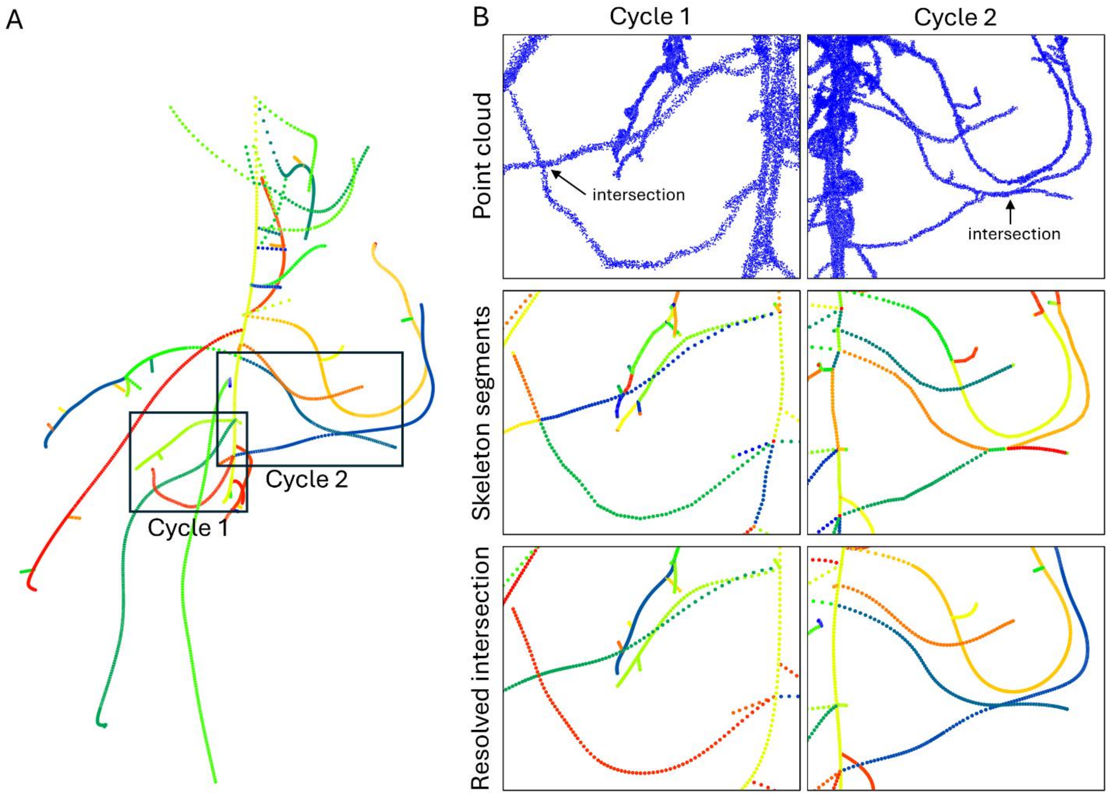

Figure 4.4: Resolved intersections in root 1. (A) Skeleton after processing with our algorithm. The image shows that both intersections that formed cycles 1 and 2 have been resolved. (B) Close-up of the point cloud, skeleton segments and resolved roots for cycles 1 and 2.

Table 4.2: Results of topological analysis.

Root	Num. of skeleton segments			Num. of detected roots	Num of junction-tip roots	Resolved segment length
	Axis segments	Junctions	Tips (excluding origin)			
root 1	90	38	50	51	49	99.41%
root 2	82	36	46	48	46	98.45%
root 3	481	197	281	287	281	99.26%
root 4	314	138	174	179	173	98.82%
root 5	574	244	322	337	322	98.56%
root 6	234	97	136	141	136	99.17%
root 7	455	200	249	261	249	98.91%
root 8	445	186	257	269	257	98.58%

Discussion

Our results demonstrate that resolving intersections in 3D root skeletons is a necessary step for recovering the branching topology of root systems and improving trait quantification. By applying a heuristic optimization approach adapted from DIRT/μ, we successfully resolved intersecting roots and reconstructed tree-like skeletons in soybean root systems. The algorithm correctly identified roots that begin and end at plausible locations (i.e., junctions and tips), while maintaining high structural completeness. Although some over-segmentation occurred, as seen by a slight excess in detected roots compared to the number of overall tips in the skeleton, most root systems were resolved with over 98% of skeleton segment length assigned to a root. These results confirm the effectiveness of our method in producing plausible root structures even in the presence of complex intersections.

Future work will aim to address these limitations and improve the robustness of the pipeline. One direction is to incorporate additional information or constraints into the optimization process. For example, integrating root diameter information into the cost function could enforce the biologically realistic pattern of monotonically decreasing diameter from the branching point toward the root tips. Another improvement would be to constrain the optimization such that all selected root paths remain connected to a single, acyclic component composed of linear root segments. This mirrors the feasibility restoration strategy used in DIRT/μ, following Abramson et al. (1996). In this case it would mean that each newly added root must be connected to its parent at a branching point. Technically, this could be achieved by adding a linking edge between the junction node of a candidate root and the connecting node of its parent root. Extending this logic further, additional constraints could be imposed to ensure that the entire reconstructed root system always forms a connected, tree-like and thus cycle-free graph.

Finally, although the algorithm improves the topological accuracy of root skeletons, it remains to be determined how this improvement influences the calculation of root traits. We have not yet quantified the differences in traits, such as lateral root length, branching angles, or lateral root density, when using a corrected skeleton versus the original skeleton with intersecting roots. Resolving intersections should prevent measurement errors, such as a lower order root being counted as a higher order lateral root. However, evaluating these differences rigorously would require further studies with manual measurements for validation, and that analysis lies beyond the scope of this chapter. Such validation will be an important future step to confirm that this method indeed leads to more accurate and biologically meaningful trait quantification.

In this study, we used eight soybean roots as representative examples for the root architecture of legumes. Soybean roots offer a relatively straightforward branching structure, making them well-suited for testing our algorithm under controlled conditions. Future applications should extend this method to more complex and densely branched architectures, such as those observed in maize. These root systems present greater challenges due to overlapping branches and higher root density and would therefore require particularly high-quality point clouds and skeletons to enable accurate reconstruction. We further anticipate that the algorithm will perform independently of applied treatments, such as drought stress, and could be used to evaluate the effect of such conditions on derived root traits.

Finally, resolving topological ambiguities in root skeletons enables more accurate quantification of traits such as lateral root length, density, and branching patterns, which are critical for understanding nutrient acquisition and drought resilience. As a result, this work represents a meaningful step toward increasing the precision of 3D root phenotyping and reinforces the role of computational tools in extracting biologically relevant traits for use in crop breeding and root system biology.

Acknowledgements

We would like to thank Joshua Carpenter for sharing data that made this final project on refining 3D root skeletons possible.

References

Abramson, D., Dang, H., & Krishnamoorthy, M. (1996). A comparison of two methods for solving 0–1 integer programs using a general purpose simulated annealing algorithm. *Annals of Operations Research*, *63*(1), 129-150. https://doi.org/10.1007/bf02601642

Bucksch, A. (2014). A practical introduction to skeletons for the plant sciences. *Applications in Plant Sciences*, *2*(8), Article 1400005. https://doi.org/10.3732/apps.1400005

Carpenter, J., Bogati, S., Jung, J., & Wang, D. (2023). 3D Root Structure Modeling and Analysis Using Close-Range Photo Scanning. https://doi.org/10.22541/essoar.169868823.31385752/v1

Claussen, J., Wittenberg, T., Uhlmann, N., & Gerth, S. (2023). "Chamber #8" - a holistic approach of high-throughput non-destructive assessment of plant roots. *Front Plant Sci*, *14*, 1269005, Article 1269005. https://doi.org/10.3389/fpls.2023.1269005

Kirkpatrick, S., Gelatt, C. D., & Vecchi, M. P. (1983). Optimization by simulated annealing. *Science*, *220*(4598), 671-680. https://doi.org/10.1126/science.220.4598.671

Liu, S. X., Barrow, C. S., Hanlon, M., Lynch, J. P., & Bucksch, A. (2021). DIRT/3D: 3D root phenotyping for field-grown maize (Zea mays). *Plant Physiology*, *187*(2), 739-757. https://doi.org/10.1093/plphys/kiab311

Lynch, J. P. (2013). Steep, cheap and deep: an ideotype to optimize water and N acquisition by maize root systems. *Ann Bot*, *112*(2), 347-357. https://doi.org/10.1093/aob/mcs293

Orsila, H., Salminen, E., & Hämäläinen, T. D. (2008). *Best practices for simulated annealing in multiprocessor task distribution problems* (Vol. 16).

Pietrzyk, P., Phan-Udom, N., Chutoe, C., Pingault, L., Roy, A., Libault, M., Saengwilai, P. J., & Bucksch, A. (2024). DIRT/µ: automated extraction of root hair traits using combinatorial optimization. *Journal of Experimental Botany*, *76*(2), 285-298. https://doi.org/10.1093/jxb/erae385

Postma, J. A., Dathe, A., & Lynch, J. P. (2014). The Optimal Lateral Root Branching Density for Maize Depends on Nitrogen and Phosphorus Availability. *Plant Physiology*, *166*(2), 590-U948. https://doi.org/10.1104/pp.113.233916

Shao, M. R., Jiang, N., Li, M., Howard, A., Lehner, K., Mullen, J. L., Gunn, S. L., McKay, J. K., & Topp, C. N. (2021). Complementary Phenotyping of Maize Root System Architecture by Root Pulling Force and X-Ray Imaging. *Plant Phenomics, 2021*. https://doi.org/doi:10.34133/2021/9859254

Zeng, D., Li, M., Jiang, N., Ju, Y., Schreiber, H., Chambers, E., Letscher, D., Ju, T., & Topp, C. N. (2021). TopoRoot: a method for computing hierarchy and fine-grained traits of maize roots from 3D imaging. *Plant Methods, 17*(1), 127. https://doi.org/10.1186/s13007-021-00829-z

Zhan, A., Schneider, H., & Lynch, J. P. (2015). Reduced Lateral Root Branching Density Improves Drought Tolerance in Maize. *Plant Physiology*, *168*(4), 1603-U1885. https://doi.org/10.1104/pp.15.00187

CHAPTER 5

CONCLUSIONS

Roots play a crucial role in plant productivity, stress adaptation, and water and nutrient acquisition from the soil (Herder et al., 2010; Paez-Garcia et al., 2015). However, despite of their importance, studying roots remains challenging due to the difficulty of accurately measuring their complex and hierarchical structures. Traditionally, many root phenotyping methods have relied on aggregated traits, such as root biomass, average diameter, or total length, which summarize the root system without fully capturing the detailed architecture. These metrics do not reflect variations in branching and root hierarchy that govern the function of roots (Fitter, 1987; York et al., 2013). Over the past two decades, improvements in high-resolution imaging and high-throughput image analysis made it possible to digitize and analyze root systems in both two and three dimensions (Atkinson et al., 2019; Bucksch et al., 2014; Li et al., 2022). However, the acquired imaging data is often noisy, incomplete, or occluded, leading to ambiguous structures such as intersecting root hairs in 2D or cycles in 3D skeletons (Bucksch, 2014; Zeng et al., 2021). These structural ambiguities distort the representation of the root system, which results in inaccurate trait measurements and potentially misleading biological interpretations. In this dissertation I address this challenge by developing and applying computational algorithms that resolve such ambiguities. Specifically, I introduce a heuristic framework that untangles intersecting structures, both in 2D images of root hairs and in 3D skeletons of whole root systems, which allows the extraction of detailed and biologically relevant traits. The goal of this work is to improve the accuracy and interpretability of root phenotyping, ultimately enabling better insight into the genetic and physiological basis of roots.

This dissertation presented three interrelated projects, which address specific technical hurdles to overcome limitations in root phenotyping. As such, the outcome enables more precise and comprehensive analysis of root traits. The main contributions of these projects are summarized below.

In Chapter 2 we developed a new image analysis algorithm, DIRT/μ, to extract individual root hairs from microscopy images (Pietrzyk et al., 2024). Phenotyping root hairs in 2D is challenging because root hairs overlap and intersect, which complicates their automated segmentation and measurements. Our solution to address this issue uses a rigorously defined set of heuristic rules that are based on biologically plausible configurations and combinatorial optimization to untangle intersecting root hairs from a skeletonized network. This approach makes it possible to measure root hair length distributions and root hair density based on all root hairs in the image, which are impractical to measure manually. Our approach goes beyond previous methods that rely on indirect measurements of traits (Lu et al., 2022; Vincent et al., 2017), and provide a finer resolution to understand root hair phenotypes. By eliminating subjective user bias from the user and increasing the throughput of measurements, our method accelerates root hair phenotyping and allows quantification of variability at the root hair level within and between plants.

Chapter 3 addresses image acquisition and 3D model reconstruction as a fundamental step for 3D root phenotyping (Pietrzyk et al., 2025). Precise camera calibration is critical to generate high-quality models of roots. Therefore, we designed and implemented a camera calibration procedure for our 3D root scanning system (Liu et al., 2021). This project systematically assessed the impact of camera settings, such as focus, aperture, and exposure time, on 3D models of excavated roots and provided practical guidelines to enhance accuracy and repeatability. We demonstrated that small improvements in camera settings lead to significantly better 3D reconstructions, which downstream enhance skeletonization and subsequent trait extraction. As such, our calibration guideline increases the confidence that differences in measured root traits reflect biological differences rather than imaging artifacts. While this chapter is more technical in nature, it provides the necessary foundation for more detailed structural analysis in later stages of root phenotyping pipelines.

Chapter 4 summarized an experimental project, which extends the core heuristic of DIRT/μ to 3D root skeletons. Skeletons of the root system architecture generated from 3D models often contain cycles that do not reflect the correct topology of the root system architecture (Zeng et al., 2021). These cycles typically result from real physical intersections of roots or intersections of roots in the point cloud due to insufficient resolution in the data. These intersections are then interpreted as junctions during skeletonization. We developed an algorithm to detect individual roots and thus resolve such intersections, restoring an acyclic tree-like topology. By correcting the skeleton topology, we enable measurements of traits such as lateral root density, individual branch lengths, and branching order. While still at an experimental stage, this contribution fills a crucial gap in root phenotyping pipelines by moving from an initially topologically incorrect skeleton with cycles to a topologically correct skeleton. In our approach, this is accomplished by detection of the physical roots, rather than cutting cycles to correct for topological errors. This project demonstrates the robustness and versatility of our heuristic. The same underlying logic is applied in both 2D and 3D data, highlighting its potential as a general-purpose tool in plant phenotyping.

These contributions provide a framework for improving root phenotyping by resolving structural ambiguity, whether at the level of microscopic root hairs or at the macroscopic scale of the whole root system. All three projects share the goal of moving from aggregated and proxy-based metrics toward trait measurements that reflect actual biological structures. In the case of root hairs, untangling individual root hairs enabled measurement of traits like length and density at single-hair resolution. In 3D root systems, resolving false intersections made it possible to detect individual lateral roots, such that meaningful topological features can be computed. This can be supported by higher accuracy in 3D models accomplished by calibration of the 3D root scanner. Another common theme is the shared heuristic, which has proven to be effective in both 2D images of root hairs and 3D skeletons of the root system, suggesting that it could serve as a versatile framework in a broader phenotyping pipeline. As such, these methods contribute to a shift in root phenotyping from measuring what can be easily extracted (e.g. total length or pixel counts), to measuring what is biologically meaningful, which is each individual root hair, each root, and each connection in the root system.

Further, the results of this dissertation are complementary in their scope, spanning a wide range of biological scales. Chapter 2 focuses on root hairs, which are single-cell appendages on the epidermis, while the other two chapters cover the whole root system. In studies where measurements are performed across scales (Bailey et al., 2002; Lippold et al., 2021; Vetterlein et al., 2022), integrating these methods into their experiments would enable researchers to have more comprehensive measurements of the entire root system. Therefore, this capability allows for the full digitization of the root system to support studies in the plant sciences and for crop improvement (Lynch, 2022).

While we achieved significant improvements for root phenotyping, several limitations and challenges of the methods must be acknowledged. First, the accuracy of both 2D and 3D methods depends on the quality of the data input. In microscopy images, poor contrast, excessive noise, or mycorrhizal fungi can impair the accuracy of root hair classification and therefore their extraction. 3D reconstructions generated via SfM are susceptible to occlusions in very dense root systems, low point density in fine roots, and remaining noise that may cause incorrect skeleton topology. Similarly, our experiments involved controlled settings (root hairs from seedling grown in hydroponic culture and excavated roots that were cleaned before imaging). Adapting our methods to work on noisier data, e.g., with soil particles, would require further testing and development.

A second challenge is that from a computational perspective, the used heuristics (in DIRT/μ and in the 3D topology correction) may struggle if image noise or root complexity violates their underlying assumptions. Though the heuristics are robust and flexible, they rely on assumptions about the geometry and connectivity of root hairs or root system architecture. These assumptions may not hold for all root types, growth stages, or imaging conditions. For example, dense and fibrous root systems with many fine lateral roots may present patterns that violate the typical branching rules built into the algorithm, potentially leading to errors.

Third, the computational complexity of resolving large numbers of intersections may result in long computation times and decrease throughput. To enable large-scale deployment in high-throughput phenotyping settings, further optimization may be necessary, e.g., by narrowing the pool of candidate root hairs or roots to reduce the size of the combinatorial search space. Finally, while the heuristic resolves local ambiguities effectively, it does not yet incorporate global structural consistency checks, such as a maximum root hair length or enforcing tree-like skeletons in roots. Future extensions could involve boundary conditions to improve both precision and robustness.

The challenges above point to several promising directions for future research. One important direction is to extend and validate these methods under different growth conditions and other species. One step would be to use DIRT/μ with images of root hairs from plants grown in soil to bridge the gap between lab and field conditions. Further, integrating our algorithm from Chapter 4 with noninvasive imaging technologies could allow phenotyping of roots in situ, such as from X-ray CT models.

One major next step is to integrate these tools into automated, high-throughput pipelines. This would enable large-scale screening of genotypes under different environmental conditions, supporting quantitative trait locus (QTL) mapping and genome-wide association studies (GWAS). Paired with robust imaging and skeletonization, our algorithms could enable the extraction of architectural traits at scale across thousands of samples. From a phenotyping pipeline perspective, future work could focus on integrating measurements across scales. A possibility would be to link the effect of root hair traits in conjunction with root architecture traits on the performance of the whole plant. This could involve experiments that phenotype root hairs (by sampling small sections of the root) and the root system architecture of the same plant.

The adaptability of the heuristic framework developed in this dissertation suggests opportunities for broader application. One promising direction is to generalize this method for analyzing other biological branching structures: tree crowns, where overlapping branches and occlusions present challenges similar to root systems; leaf venation networks, which often include intersecting paths and ambiguous junctions; and shoot architecture, where internode relationships and lateral branches define morphological variation.

In conclusion, this dissertation advances root phenotyping by addressing structural ambiguity that arises in both 2D and 3D root imaging data. By developing a heuristic framework to untangle intersecting root hairs and roots, this work enables accurate measurement of fine-scale and biologically meaningful traits, such as individual root hair length or root topology, that are often lost in aggregated metrics. The methods are grounded in the biological structures, interpretable, and applicable across spatial scales. Together, these contributions help bridge the gap between image data and functional root traits, supporting more precise studies of root development and more informed selection of root phenotypes for crop improvement.

References

Atkinson, J. A., Pound, M. P., Bennett, M. J., & Wells, D. M. (2019). Uncovering the hidden half of plants using new advances in root phenotyping. *Current Opinion in Biotechnology*, *55*, 1-8. https://doi.org/https://doi.org/10.1016/j.copbio.2018.06.002

Bailey, P. H. J., Currey, J. D., & Fitter, A. H. (2002). The role of root system architecture and root hairs in promoting anchorage against uprooting forces in Allium cepa and root mutants of Arabidopsis thaliana. *Journal of Experimental Botany*, *53*(367), 333-340. https://doi.org/10.1093/jexbot/53.367.333

Bucksch, A. (2014). A practical introduction to skeletons for the plant sciences. *Applications in Plant Sciences*, *2*(8), Article 1400005. https://doi.org/10.3732/apps.1400005

Bucksch, A., Burridge, J., York, L. M., Das, A., Nord, E., Weitz, J. S., & Lynch, J. P. (2014). Image-based high-throughput field phenotyping of crop roots. *Plant Physiol*, *166*(2), 470-486. https://doi.org/10.1104/pp.114.243519

Fitter, A. H. (1987). An Architectural Approach to the Comparative Ecology of Plant-Root Systems. *New Phytologist*, *106*(1), 61-77. https://doi.org/DOI 10.1111/j.1469-8137.1987.tb04683.x

Herder, G. D., Van Isterdael, G., Beeckman, T., & De Smet, I. (2010). The roots of a new green revolution. *Trends in plant science*, *15*(11), 600-607. https://doi.org/10.1016/j.tplants.2010.08.009

Li, A., Zhu, L., Xu, W., Liu, L., & Teng, G. (2022). Recent advances in methods for in situ root phenotyping. *PEERJ*, *10*, e13638, Article e13638. https://doi.org/10.7717/peerj.13638

Lippold, E., Phalempin, M., Schlüter, S., & Vetterlein, D. (2021). Does the lack of root hairs alter root system architecture of Zea mays? *Plant and Soil*, *467*(1), 267-286. https://doi.org/10.1007/s11104-021-05084-8

Liu, S. X., Barrow, C. S., Hanlon, M., Lynch, J. P., & Bucksch, A. (2021). DIRT/3D: 3D root phenotyping for field-grown maize (Zea mays). *Plant Physiology*, *187*(2), 739-757. https://doi.org/10.1093/plphys/kiab311

Lu, W., Wang, X., & Jia, W. (2022). Root hair image processing based on deep learning and prior knowledge. *Computers and Electronics in Agriculture*, *202*, Article 107397. https://doi.org/10.1016/j.compag.2022.107397

Lynch, J. P. (2022). Harnessing root architecture to address global challenges. *Plant J*, *109*(2), 415-431. https://doi.org/10.1111/tpj.15560

Paez-Garcia, A., Motes, C. M., Scheible, W. R., Chen, R., Blancaflor, E. B., & Monteros, M. J. (2015). Root Traits and Phenotyping Strategies for Plant Improvement [article]. *Plants (Basel)*, *4*(2), 334-355. https://doi.org/10.3390/plants4020334

Pietrzyk, P., Liu, S., & Bucksch, A. (2025). Optimizing root phenotyping: Assessing the impact of camera calibration on 3D root reconstruction. *bioRxiv*, 2025.2003.2009.642238. https://doi.org/10.1101/2025.03.09.642238

Pietrzyk, P., Phan-Udom, N., Chutoe, C., Pingault, L., Roy, A., Libault, M., Saengwilai, P. J., & Bucksch, A. (2024). DIRT/μ: automated extraction of root hair traits using combinatorial optimization. *Journal of Experimental Botany*, *76*(2), 285-298. https://doi.org/10.1093/jxb/erae385

Vetterlein, D., Phalempin, M., Lippold, E., Schluter, S., Schreiter, S., Ahmed, M. A., Carminati, A., Duddek, P., Jorda, H., Bienert, G. P., Bienert, M. D., Tarkka, M., Ganther, M., Oburger, E., Santangeli, M., Javaux, M., & Vanderborght, J. (2022). Root hairs matter at field scale for maize shoot growth and nutrient uptake, but root trait plasticity is primarily triggered by texture and drought. *Plant and Soil*, *478*(1-2), 119-141. https://doi.org/10.1007/s11104-022-05434-0

Vincent, C., Rowland, D., Na, C., & Schaffer, B. (2017). A high-throughput method to quantify root hair area in digital images taken in situ. *Plant and Soil*, *412*(1-2), 61-80. https://doi.org/10.1007/s11104-016-3016-9

York, L. M., Nord, E. A., & Lynch, J. P. (2013). Integration of root phenes for soil resource acquisition. *Frontiers in Plant Science*, *4*, Article 355. https://doi.org/10.3389/fpls.2013.00355

Zeng, D., Li, M., Jiang, N., Ju, Y., Schreiber, H., Chambers, E., Letscher, D., Ju, T., & Topp, C. N. (2021). TopoRoot: a method for computing hierarchy and fine-grained traits of maize roots from 3D imaging. *Plant Methods*, *17*(1), 127. https://doi.org/10.1186/s13007-021-00829-z

APPENDIX A

SUPPLEMENTARY MATERIAL FOR CHAPTER 2

Supplementary Protocols

Protocol S1: Plant material and growth conditions (Mahidol I and Mahidol II). The plants used in the Mahidol I dataset were Kaw Dawk Mali 105 rice (KDML105), maize (commercial super sweet corn #00252), and common bean (DOR364). For the Mahidol II dataset, the rice genotypes were KDML105, Phitsanulok 2, and Sungyod, which are all Thai rice varieties. KDML105, commonly known as jasmine rice, is lowland, photoperiod-sensitive, and the most important commercial rice variety in Thailand. Phitsanulok 2 is an upland rice variety that is photoperiod-insensitive. Sungyod is a variety local to Phattalung Province in the south of Thailand that produces distinct red-colored grains. The maize genotypes used were Takfa 1, Takfa 2, and Takfa 3, all of which are inbred lines from the Nakhon Sawan Field Crops Research Center, Thailand. For common bean, the genotypes used were the high-yielding variety DOR364, the recombinant inbred line L8857 (a cross of phosphorous deficiency and drought-tolerant parents), and the drought-tolerant variety SEQ7. The rice, maize, and common bean seeds were surface-sterilized using 0.5% NaOCl for 5 mins, 6% NaOCl for 15 mins, and 50% NaOCl for 1 min, respectively. The seeds were germinated using a roll-up system, and the rolls were soaked in 0.5 mM $CaSO_4$ to promote root growth. The seeds were left to germinate in complete darkness until the first shoot appeared over the roll (approximately four to seven days). The seedlings were moved to light three days before transplanting them to hydroponics culture.

The plants were grown in mason jars wrapped with tinfoil and filled with nutrient solution in 2/3 of the jar (approximately 130 mL). The full-strength (X1) control nutrient solution contained 6 mM KNO_3, 4 mM $Ca(NO_3)_2 \cdot 10H_2O$, 2 mM $NH_4H_2PO_4$, 1 mM $MgSO_4 \cdot 7\ H_2O$, and 1 mM of micronutrient stock solution. The micronutrient stock solution contained 50 µmol KCl, 25 µmol H_3Bo_3, 2 µmol $MnSO_4 \cdot H_2O$, 2 µmol $ZnSO4 \cdot 7\ H_2O$, 0.5 µmol $CuSO4 \cdot 5\ H_2O$, 0.5 µmol

$(NH_4)_6Mo_7O_{24}$, and 50 µmol Fe-EDTA. The nutrient solution for each nutrient deficiency treatment was made by omitting the salts containing the nutrient in the control solution. Supplementary salts were added to maintain the concentration of other elements. The pH was adjusted to 6.5, and the nutrient solution was sterilized by autoclaving. To acclimate the plants, a quarter-strength (X1/4) nutrient solution was used in the first week and increased to half-strength (X1/2) in the second week and until the end of the experiment. The nutrient solutions were changed every three days. The maize and rice were grown in the greenhouse at Mahidol University, Salaya Campus (13°47’34.2”N 100°19’23.5”E) for 14 days after transplanting (DAP) in July and November 2019, with an average temperature of 32±3°C and 28±2°C, respectively. Common bean plants were grown for 30 DAP on a hydroponic shelf at 27±2°C with a photoperiod of 12 hours.

The shoot was cut and oven-dried at 60°C for 72 hours to obtain the shoot dry weight. The root was washed using distilled water and preserved in 70% ethanol before root hair imaging.

Protocol S2: Collection of ground truth (Mahidol I and II). For the Mahidol I dataset, root segments were collected from different root classes, including primary roots from all plant species, basal roots from beans, seminal roots from maize, and crown roots from rice. Only the primary root was selected for the Mahidol II dataset. The root segment was cut from the whole root and washed with distilled water. The root was stained by dipping it in 0.5% (w/v) toluidine blue for approximately 10 sec and floating it in a Petri dish filled with water. The root hairs were observed and photographed at 0.25x to 6.3x magnification using an Olympus MVX10 microscope mounted with a camera (Olympus, Tokyo, Japan). In most samples between four and six images of root hairs were taken in the zone of maturation (starting approximately 1 cm below the base of the root). Small, soft brushes were used to untangle and straighten root hairs that clumped together and to brush off any debris that blocked the view of the root hairs. Root hair lengths and RHD were manually measured using the software ImageJ (1.52a). In Dataset Mahidol I the RHL of all root hairs was measured and all root hairs were counted. Regarding RHL in Dataset Mahidol II, only five representative root hairs were measured per image and RHD was measured as the number of root hairs per 1 mm section.

Protocol S3: Plant material and growth conditions (UNL). Sorghum recombinant inbred lines (RILs) derived from parental lines RTx7000 and BTx642 were used in this experiment. Eighteen seeds of each sorghum RIL were surface-sterilized and grown in a pot containing an autoclaved mix of Vermiculite:Perlite (ratio 3:1) for five days, as described by Pingault et al. (2018). The seedlings for each RIL with good germination were then divided into two groups with the same number of plants. Each group was transferred into an ultrasound aeroponic system (UAS) and grown under well-water (WW) control or treatment (drought; DR) conditions at a 16 hr light : 8 hr dark cycle(Pingault et al., 2018; Qiao & Libault, 2013). After transfer into the UASs, the plants were grown for four weeks with the same settings as the nutritive solution and delivered using a timer with the settings: 30sec ON/30sec OFF(Broughton & Dilworth, 1971; Pingault et al., 2018). Then, the plants were grown for an additional two weeks under control conditions (no change in the growing settings, timer: 30sec ON/30sec OFF) for one UAS, or under drought conditions (decrease of the solution delivery, 30sec ON, and decrease the OFF time by 10sec/day until 130sec) for the other UAS. After growing for six weeks in the UASs, the root system of each plant was collected, and the lateral roots were separated from the primary root, kept in 70% ethanol on Petri dishes, and stored at -20 °C for microscopic analysis. For this analysis, the lateral roots were stained with 0.01% trypan blue for 5 min. Then, the stained roots were placed in a clean Petri dish under a microscope to locate the root hairs' location and remove the "top" and "bottom" portions of the root that contained no visible root hairs with a scalpel. The remaining sections of roots were cut into three segments (Section 1 was the topmost portion of the root, and Section 3 was the lowermost section of the root) of equal length and placed into Petri dishes containing pure water for 15 min. Once the 15-min period had elapsed, each section was placed into the 0.01% Trypan blue staining solution for 10 min, rinsed with deionized water for 3 min, and the root section was dried with a paper towel until all visible liquid was removed. The root section was fixed on a microscope slide and placed under a Leica MZ10 F stereomicroscope with a QIMaging camera to record a 20-sec film by moving the coarse focus knob ¼ clockwise. Each film was converted into an image file using a macro in ImageJ, and the image file was used to measure the RHL using ImageJ.

Protocol S4: Image preparation. We used the *Enhance Contrast* function in ImageJ (Version 1.52p) to increase homogeneity in brightness between all images in Datasets Mahidol II and UNL. For all images, we enhanced the contrast by normalizing the histogram with 2.5% of all pixels being saturated.

Protocol S5: Training and classification of images. We used ilastik (Version 1.3.2) to create the training data manually and used its random forest classifier for pixel classification. All six features available in ilastik were used: Gaussian smoothing was used to discern color and brightness; Laplacian of Gaussian, Gaussian Gradient Magnitude, Difference of Gaussians to distinguish edges; and Structure Tensor Eigenvalues and Hessian of Gaussian Eigenvalues to distinguish texture. For Mahidol I, we used 0.7, 1.0, 1.6, 3.5, 5.0, 10.0 as the values for sigma at each red, green, and blue (RGB) channel to account for features at multiple scales. For Gaussian smoothing, we used an additional sigma of 0.3. For Mahidol II, we used 0.7, 1.0, 1.6, 3.5, 5.0, 10.0, 15.0, 20.0, and 50.0 for sigma and an additional sigma of 0.3 for Gaussian smoothing at each

RGB channel. For the UNL dataset, we used the same settings as for Mahidol I, with the exception that we used only the available monochrome channel.

The 15 images in Dataset Mahidol I were trained and classified individually. Classes were exported into .tiff files. For Mahidol II, each genotype was trained and classified individually. Here, we used a set of 10 images for each genotype. After classification, we exported the classification probability of each class into a .tiff file and applied a Gaussian smoothing filter with a sigma equal to 1.5 to each classification probability using a Python script. Subsequently, the class with the highest probability was selected for each pixel and exported into a .tiff file with the resulting classes. This additional step resulted in more spatially homogenous classifications and a reduction of noise in the downstream process, such as the closing of tiny gaps, and improved extraction of the medial axis. For UNL, we proceeded similarly to Mahidol I and created a single training set from 47 images and extracted class probabilities for all images in a single batch process.

Protocol S6: Preprocessing classified images. The DIRT/μ algorithm retains only the largest connected component of the root, removes small root hair clusters (number of pixels < square of median root hair diameter) and root hair clusters that are >10 pixels from the root, closes small gaps with morphological closing, and removes small, isolated clusters with morphological opening in root hair, root, and background.

Protocol S7: Medial axis extraction. Extracting the medial axis from root hair pixels frequently results in artifacts at the transitions from root hairs to the root. Therefore, the medial axis is extracted from the union of root hair and root pixels and then clipped at the transition from root hair to root. Small branches of the medial axis are pruned if they only marginally contribute to the shape of the root hair.

Protocol S8: Creating candidate root hairs. It is unfeasible to create an exhaustive set of candidate root hairs by considering all topologically possible paths on the graph. We limit the set to paths between pairs of nodes that satisfy certain criteria. The start node *s* and the end node *e* must be in the same connected graph, and the shortest distance from *s* to *e* must be 10 nodes at most. Then, all paths between *s* and *e* are determined whose length is smaller than or equal to the shortest distance plus one node.

Protocol S9: Spline fitting and evaluation. The splines are fitted using the *splprep* function in SciPy(Virtanen et al., 2020), such that the condition in Equation 2 is satisfied, in which *w* are the weights, *y* contains the locations of the medial axis pixels, and *g* is the corresponding location of the fitted spline. The smoothing factor *s* is set equal to the total number of points on the spline (equaling the number of points of the medial axis).

$$\sum(\mathrm{w} \cdot (\mathrm{y} - \mathrm{g}))^2 \leq \mathrm{s} \qquad \text{(Eq. 2)}$$

Protocol S10: Calculation of total curvature. The local curvature of splines is approximated numerically using Equation 3.

$$\kappa = \frac{|\mathrm{x}'\mathrm{y}'' - \mathrm{y}'\mathrm{x}''|}{(\mathrm{x}'\mathrm{x}' + \mathrm{y}'\mathrm{y}')^{3/2}} \qquad \text{(Eq. 3)}$$

The total curvature of the spline or segment is calculated by integrating Equation 3 over the *lengths* of the spline or segment, respectively (Equation 4).

$$\kappa_{\mathrm{total}} = \int \kappa \mathrm{ds} \qquad \text{(Eq. 4)}$$

Protocol S11: Conflicting root hairs. Two splines intersect in an invalid manner if, at the intersecting segments, more than 50 points of a spline are closer than √2 pixels from the other spline.

Protocol S12: Simulated annealing. We use a *geometric temperature schedule* and a *normalized exponential form* for the *acceptance function*. The targeted *number of temperature* *levels* is user-defined, and the *number of iterations at each level* equals the number of candidate splines. As a normalization factor for the *acceptance function,* we use the *initial cost*, which is calculated as the mean cost during a simulation with a predefined number of random iterations (0.2 × *number of temperature levels* × *number of iterations at each level*). The *initial temperature* is determined through heating. Here, we use an acceptance probability of 0.95 and compute the average increase in cost from all moves of the simulation, in which the *total cost* increases. For our *final temperature*, we use an acceptance probability of 0.01 at each move, such that at each *temperature level* the acceptance probability is approximated by 0.01/*number of iterations at each level*. Based on the *initial* and *final temperatures* and the user-defined *number of temperature levels,* we can determine the *geometric temperature scaling factor* for the *geometric temperature schedule*.

Moves are defined as selecting a single random spline and either adding it to or removing it from the current state. If the spline does not exist in the current state, we try to add it based on the acceptance function, and vice versa, if the spline exists already in the current state, we try to remove it based on the acceptance function. If the move is rejected, we reestablish the previous state and attempt a new random move. The optimization process is terminated when the temperature is below the *final temperature* and sufficient consecutive moves, equaling the *number of iterations at each level*, have been rejected.

Figures

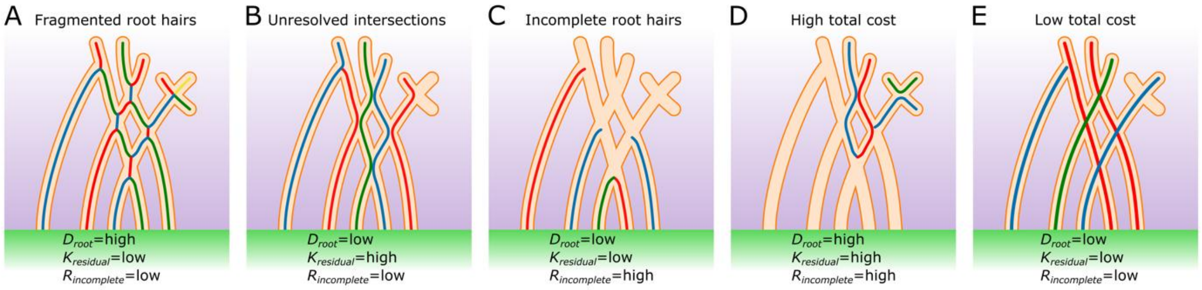

Figure S1: Combinations of root hairs are optimized by minimizing the three metrics of distance to the root, curvature, and incompleteness. Fragmented root hairs result in a high distance to the root (A), incorrectly resolved root hairs result in high curvatures (B), and incomplete root hairs result in a high cost for incompleteness (C). (D) Combinations of these cases result in high total cost. (E) In the optimized solution all three metrics have low values, resulting in low total cost.

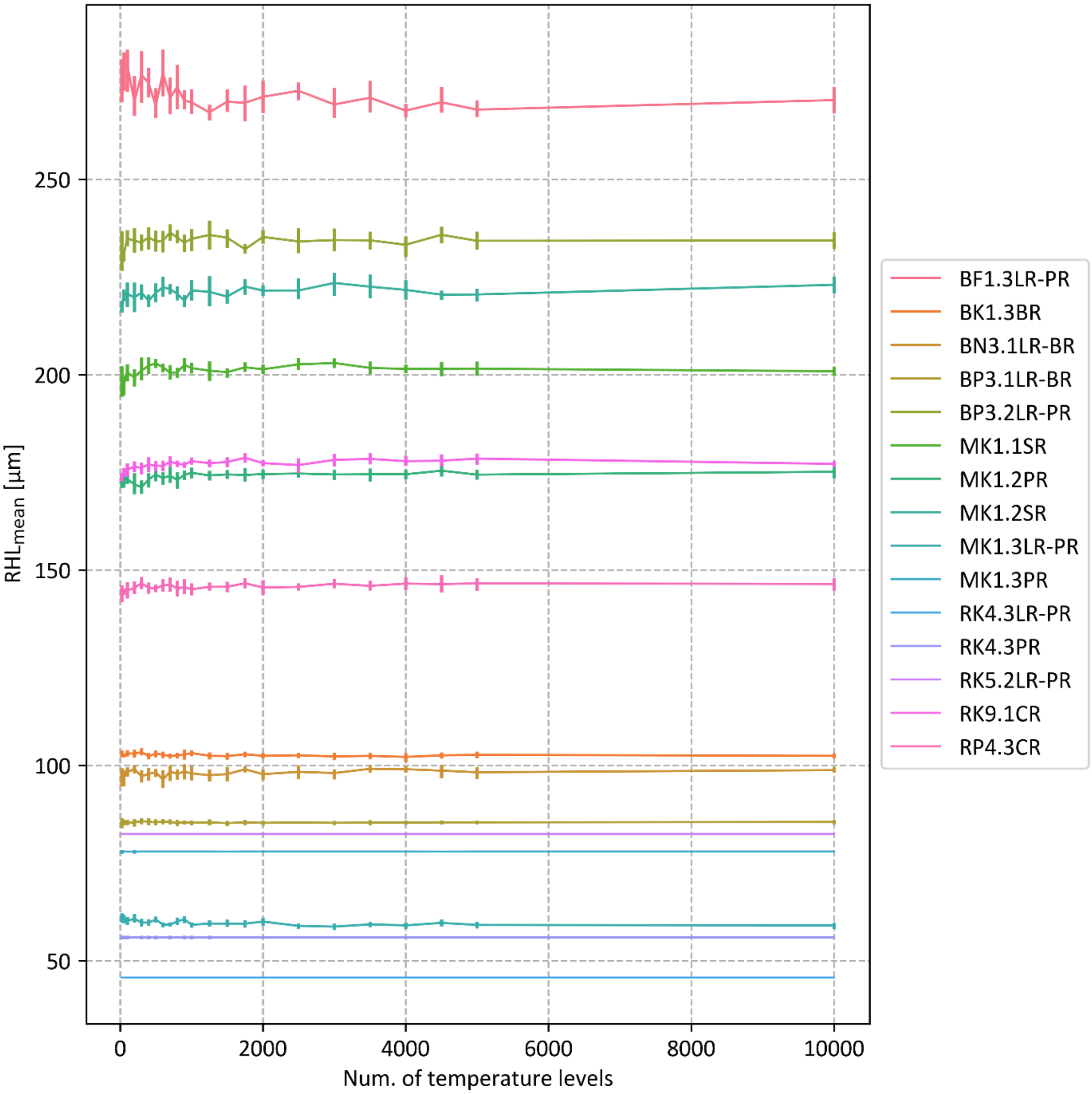

Figure S2: RHL$_{mean}$ as a function of temperature levels for all fifteen images in Dataset Mahidol I. Each colored line represents results for one image. Measurements were taken for 25, 50, 100, 200, 300, 400, 500, 600, 700, 800, 900, 1000, 1250, 1500, 1750, 2000, 2500, 3000, 3500, 4000, 4500, 5000, and 10000 temperature levels. Results were computed five times for each image and at each level. The line indicates the corresponding mean values and the vertical bars the 95% confidence interval.

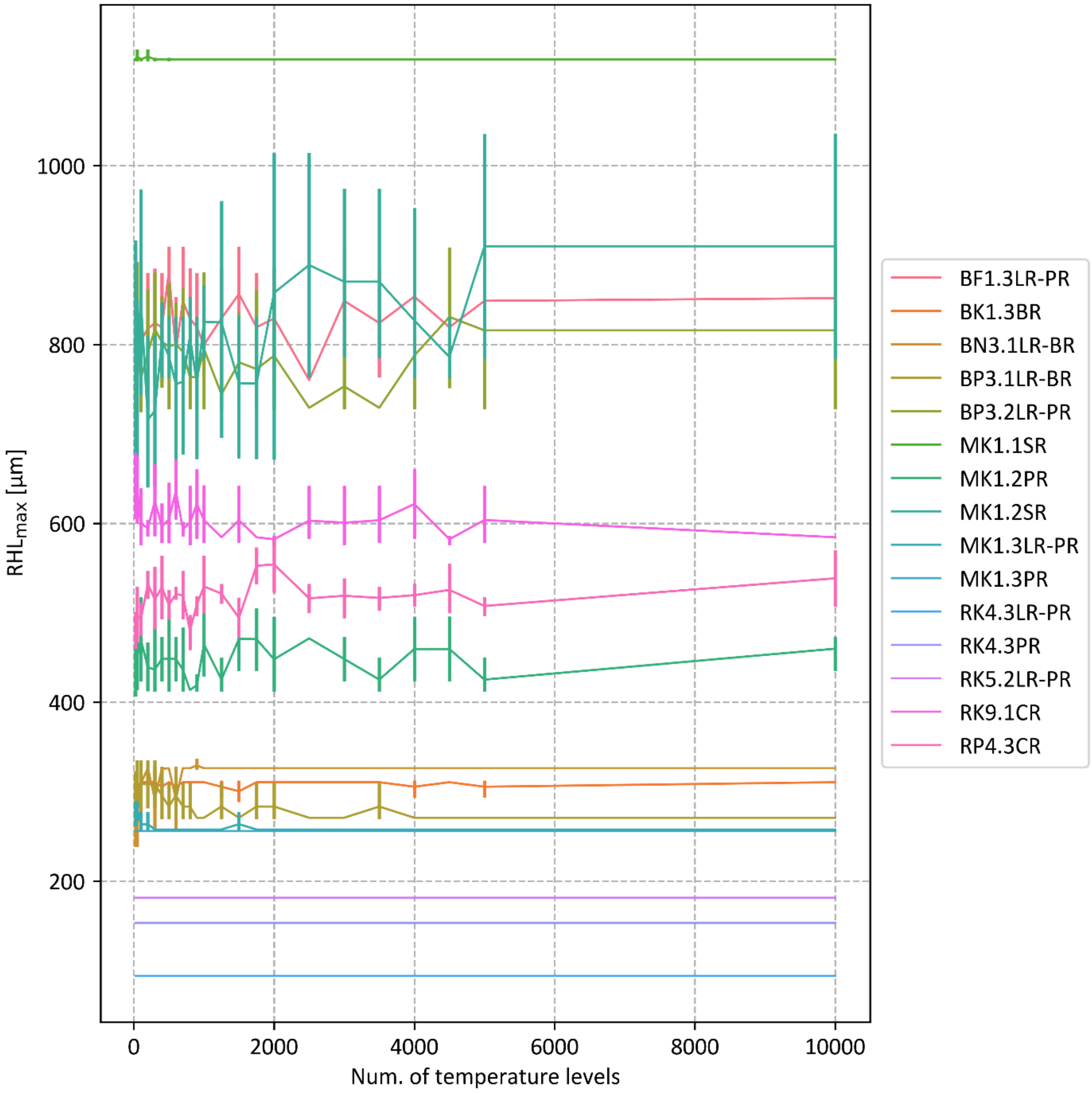

Figure S3: RHL$_{max}$ as a function of temperature levels for all fifteen images in Dataset Mahidol I. Each colored line represents results for one image. Measurements were taken for 25, 50, 100, 200, 300, 400, 500, 600, 700, 800, 900, 1000, 1250, 1500, 1750, 2000, 2500, 3000, 3500, 4000, 4500, 5000, and 10000 temperature levels. Results were computed five times for each image and at each level. The line indicates the corresponding mean values and the vertical bars the 95% confidence interval.

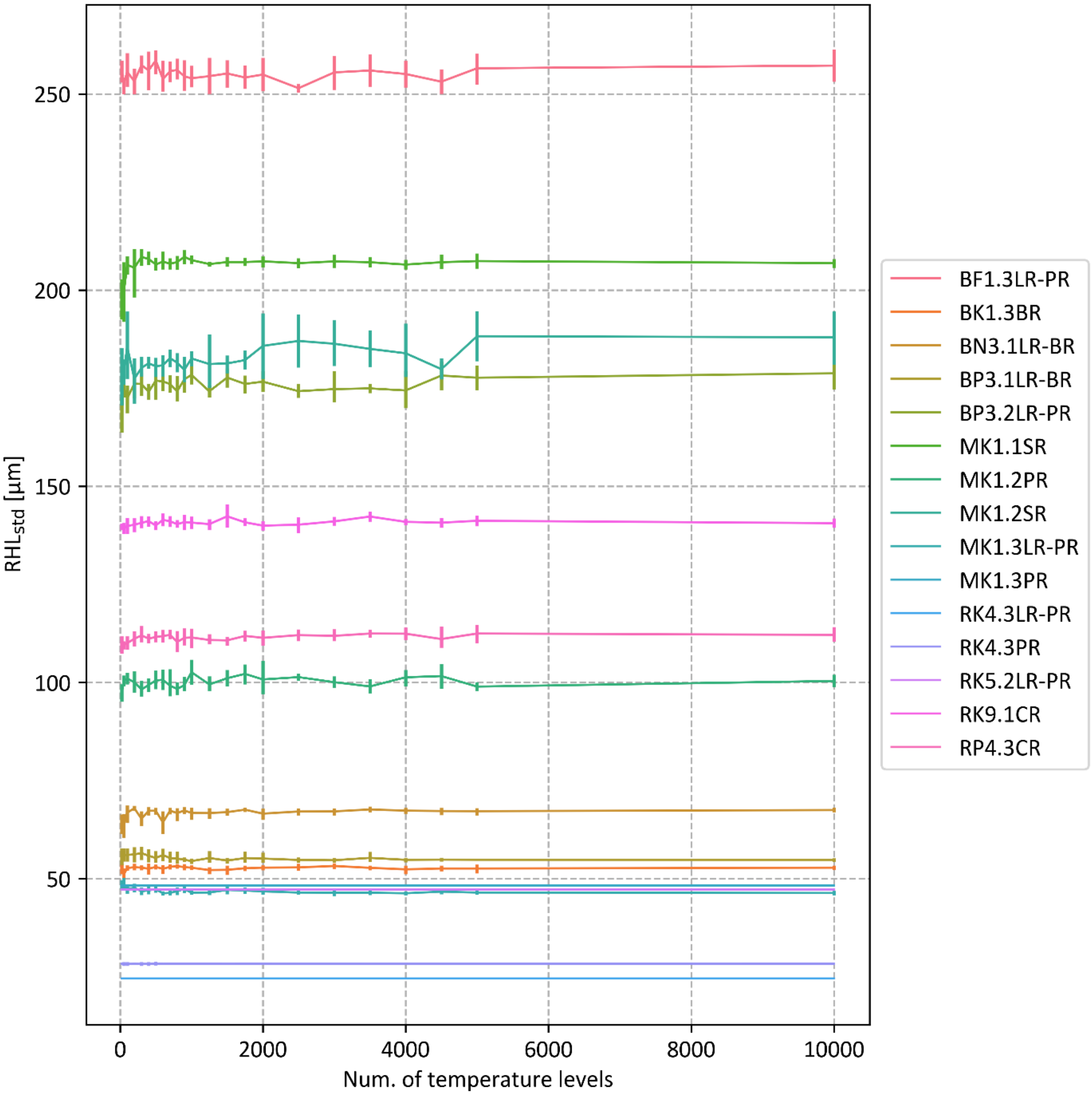

Figure S4: RHL$_{std}$ as a function of temperature levels for all fifteen images in Dataset Mahidol I. Each colored line represents results for one image. Measurements were taken for 25, 50, 100, 200, 300, 400, 500, 600, 700, 800, 900, 1000, 1250, 1500, 1750, 2000, 2500, 3000, 3500, 4000, 4500, 5000, and 10000 temperature levels. Results were computed five times for each image and at each level. The line indicates the corresponding mean values and the vertical bars the 95% confidence interval.

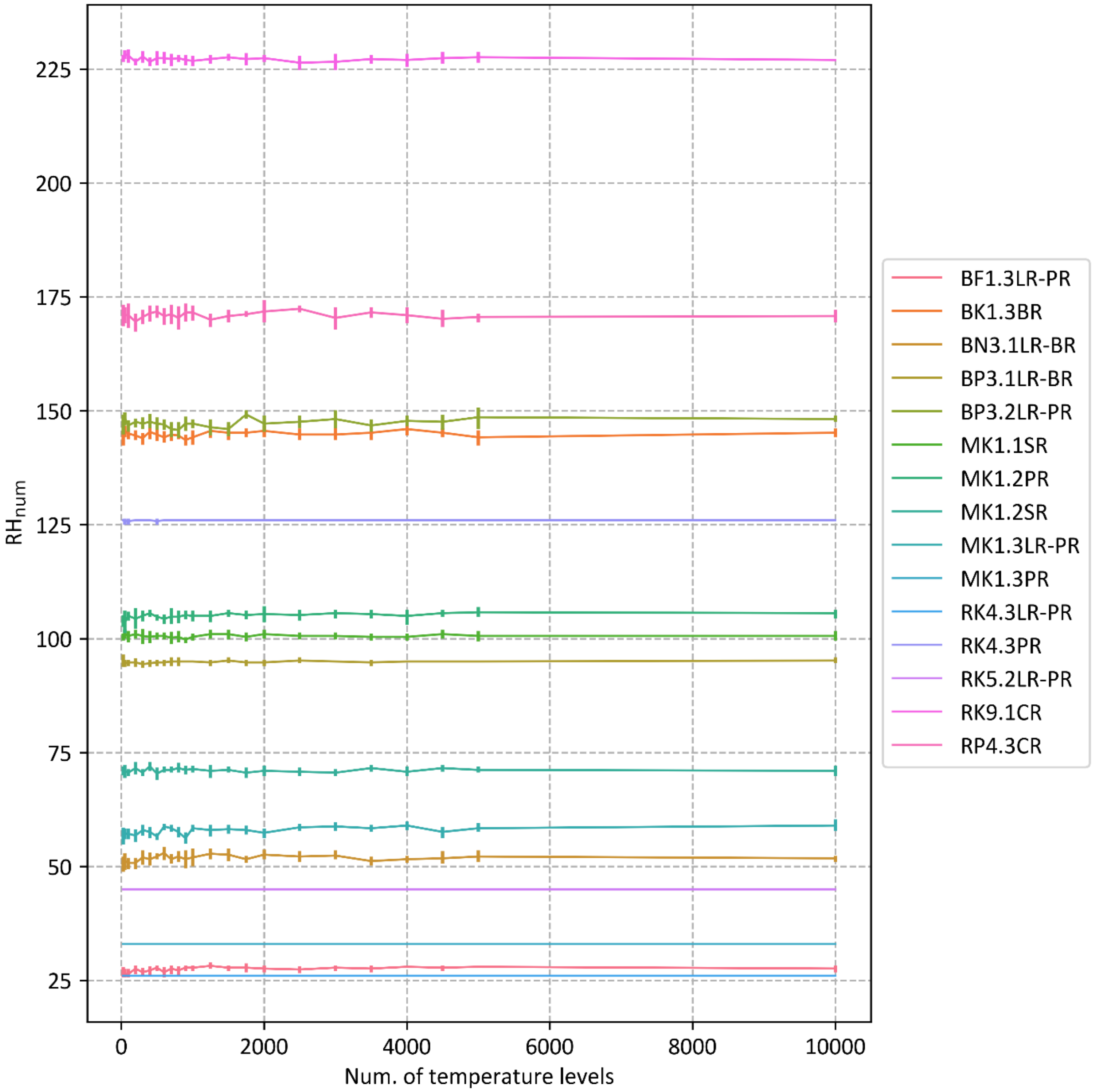

Figure S5: RH$_{num}$ as a function of temperature levels for all fifteen images in Dataset Mahidol I. Each colored line represents results for one image. Measurements were taken for 25, 50, 100, 200, 300, 400, 500, 600, 700, 800, 900, 1000, 1250, 1500, 1750, 2000, 2500, 3000, 3500, 4000, 4500, 5000, and 10000 temperature levels. Results were computed five times for each image and at each level. The line indicates the corresponding mean values and the vertical bars the 95% confidence interval.

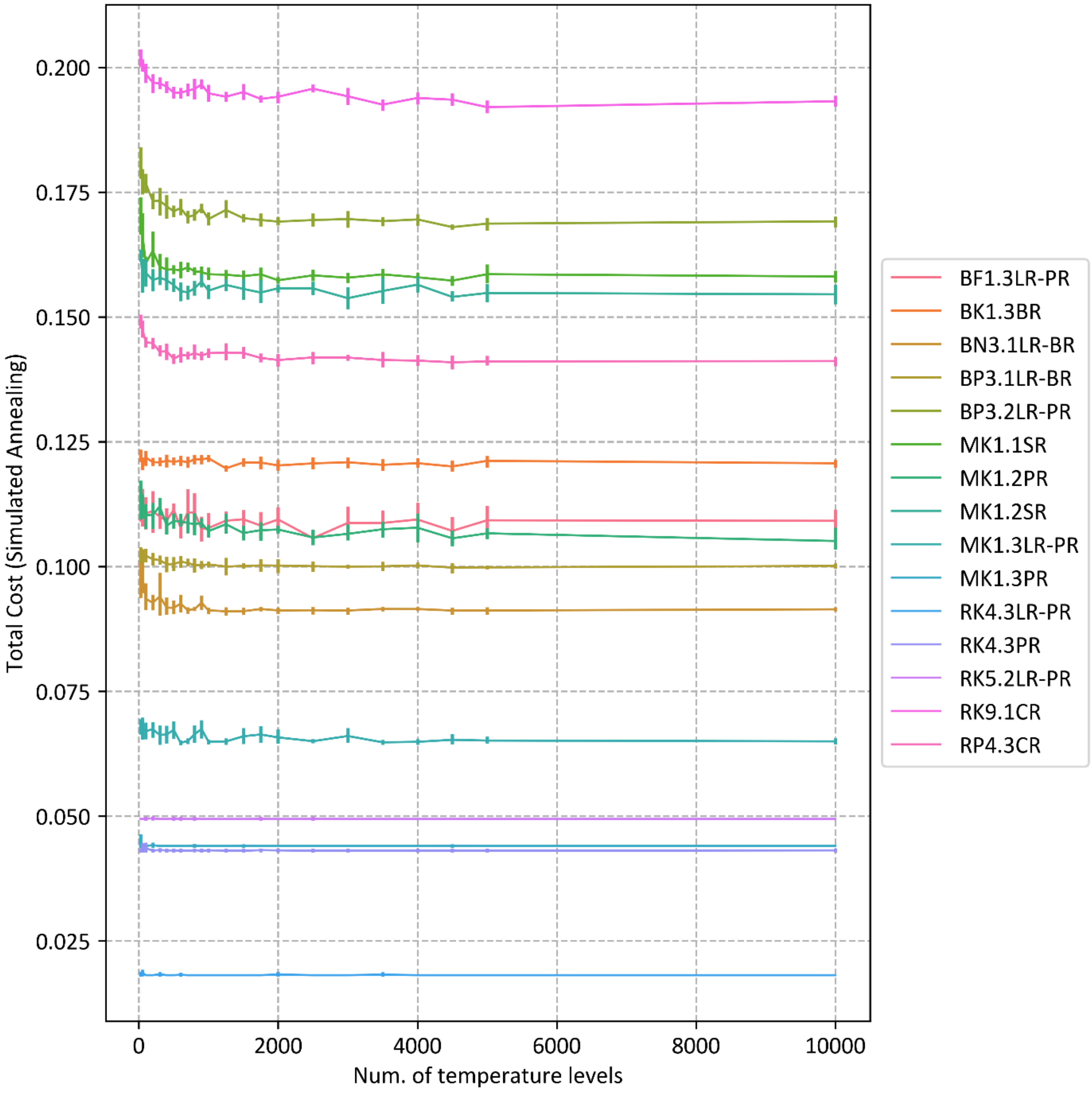

Figure S6: Total cost as a function of temperature levels for all fifteen images in Dataset Mahidol I. Each colored line represents results for one image. Measurements were taken for 25, 50, 100, 200, 300, 400, 500, 600, 700, 800, 900, 1000, 1250, 1500, 1750, 2000, 2500, 3000, 3500, 4000, 4500, 5000, and 10000 temperature levels. Results were computed five times for each image and at each level. The line indicates the corresponding mean values and the vertical bars the 95% confidence interval.

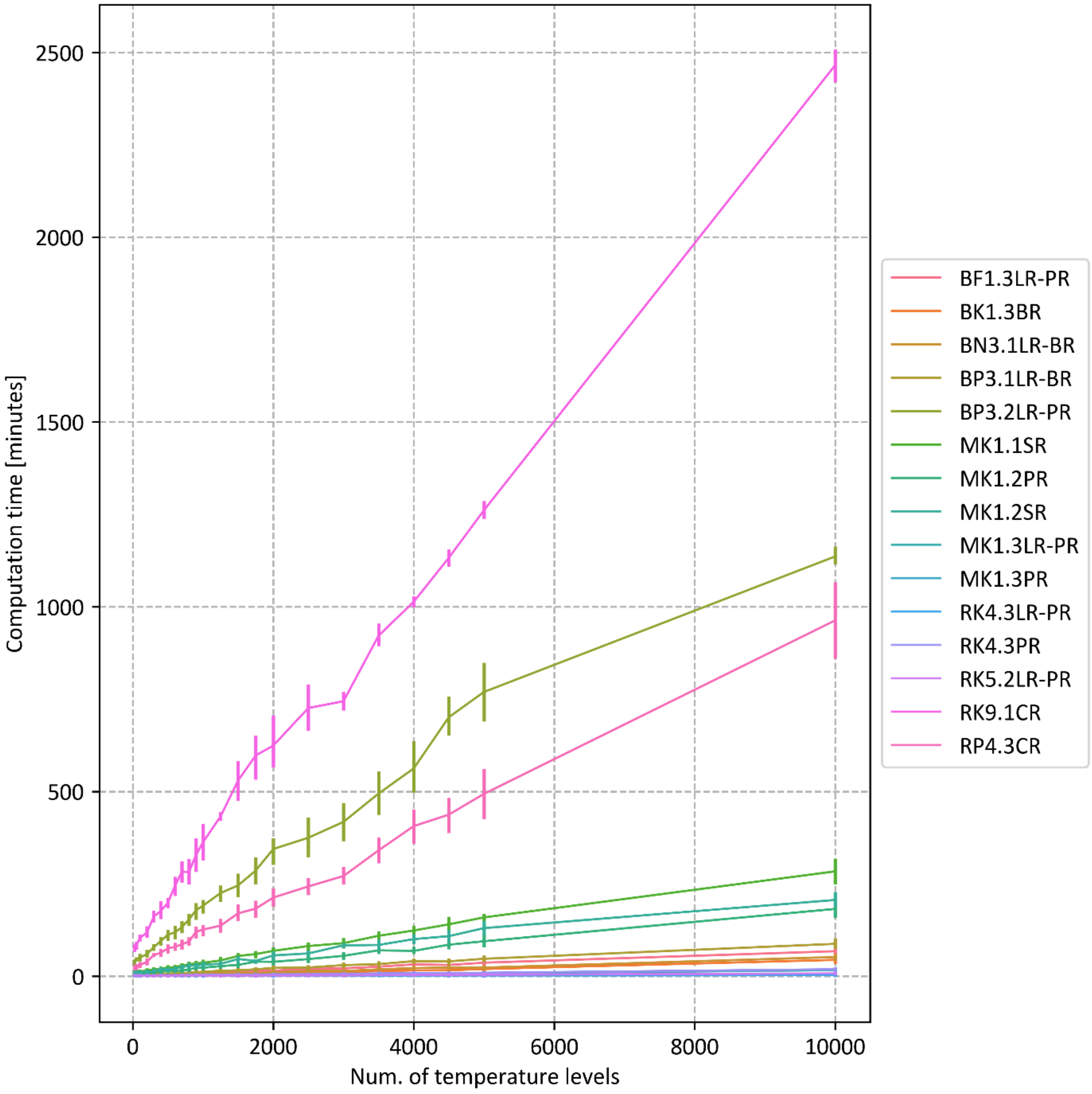

Figure S7: Computation time as a function of temperature levels for all fifteen images in Dataset Mahidol I. Each colored line represents results for one image. Measurements were taken for 25, 50, 100, 200, 300, 400, 500, 600, 700, 800, 900, 1000, 1250, 1500, 1750, 2000, 2500, 3000, 3500, 4000, 4500, 5000, and 10000 temperature levels. Results were computed five times for each image and at each level. The line indicates the corresponding mean values and the vertical bars the 95% confidence interval.

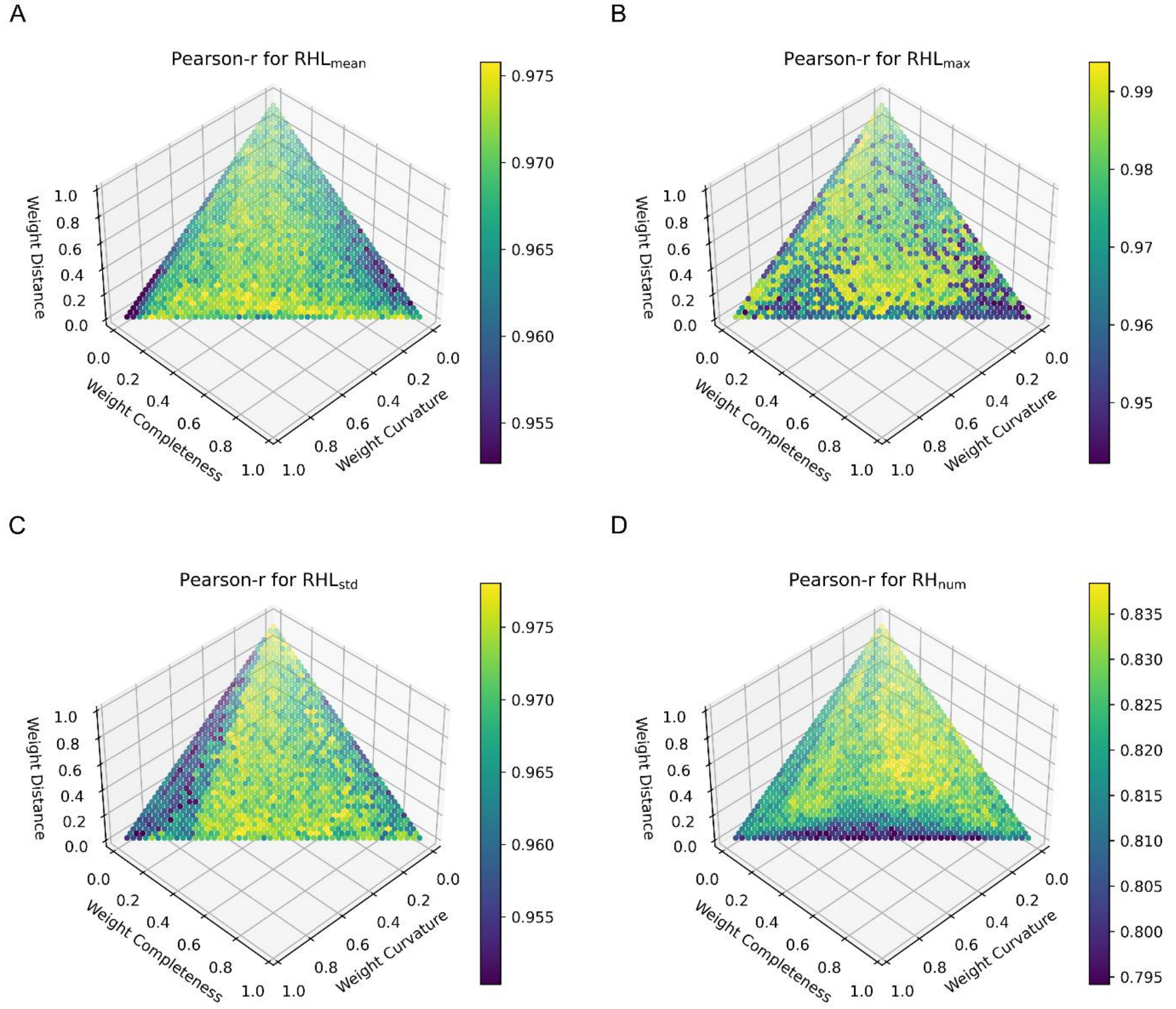

Figure S8: Pearson correlation coefficients indicated by color between manual and automatic measurements for different values of simulated annealing weights. Correlations are shown for four measured variables: (A) Correlation coefficient for $\mathrm{RHL}_{\mathrm{mean}}$, (B) correlation coefficient for $\mathrm{RHL}_{\mathrm{max}}$, (C) correlation coefficient for $\mathrm{RHL}_{\mathrm{std}}$, and (D) correlation coefficient for $\mathrm{RH}_{\mathrm{num}}$.

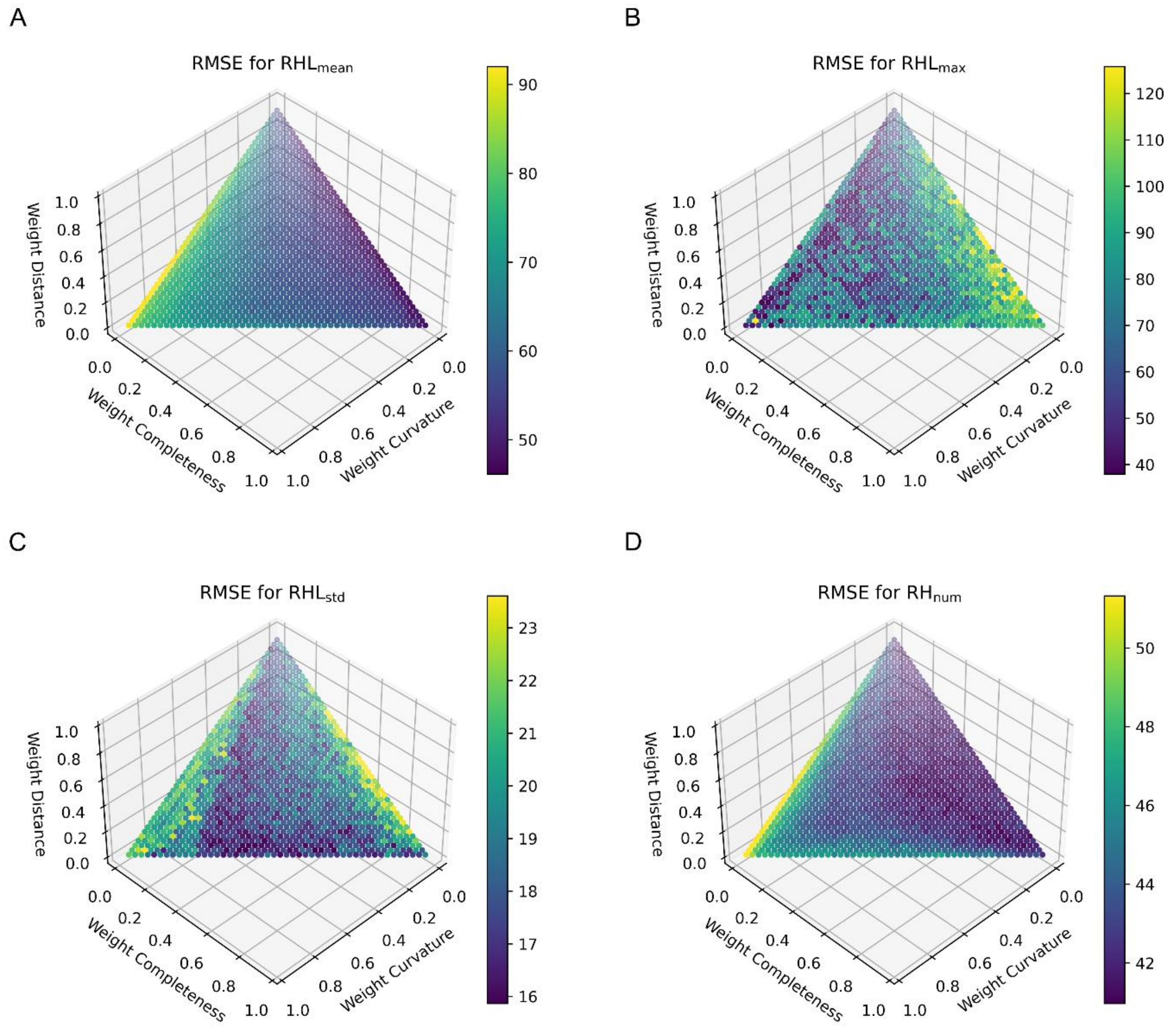

Figure S9: RMSE between manual and automatic measurements for different values of SA weights as indicated by color. Correlations are shown for four measured variables: (A) RMSE for RHL_{mean}, (B) RMSE for RHL_{max}, (C) RMSE for RHL_{std}, and (D) RMSE for RH_{num}.

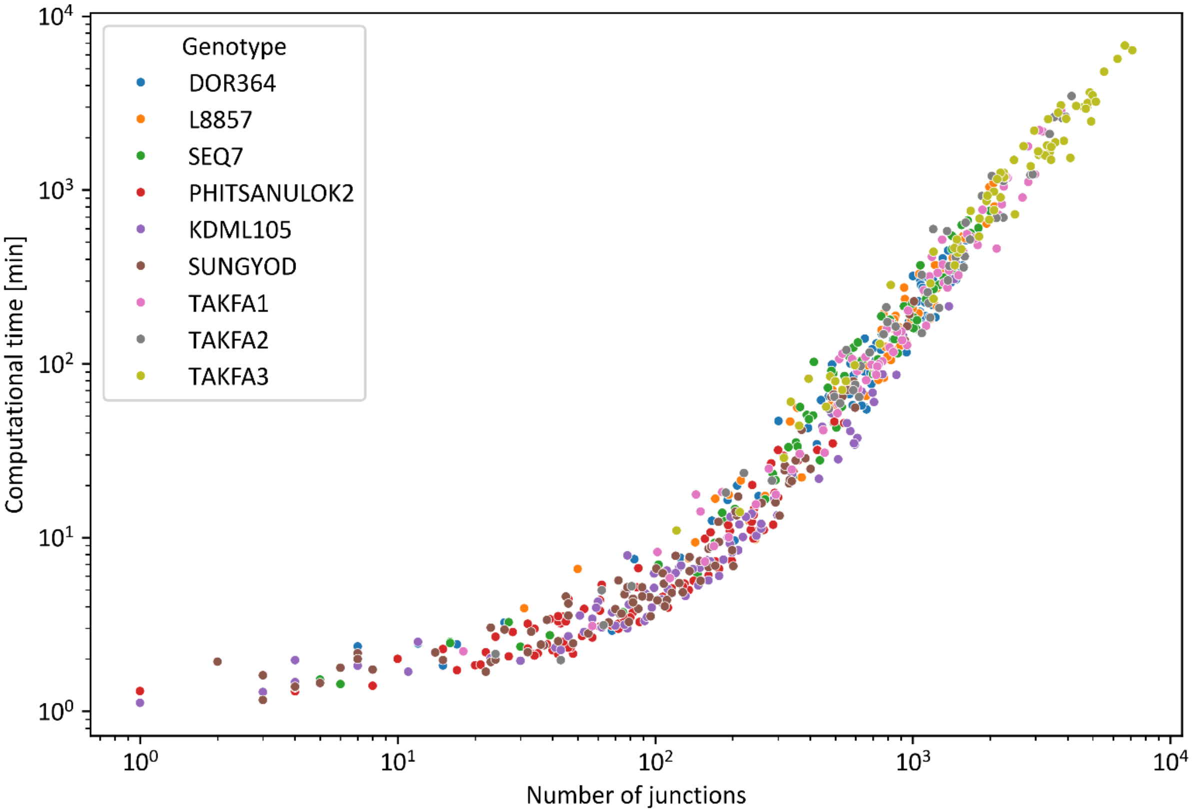

Figure S10: Computation time as function of junctions for images in Dataset Mahidol II. Each measurement point represents one image and shows the number of junctions on the medial axis and the time required to process the image in log10 scale. The color depicts the genotype.

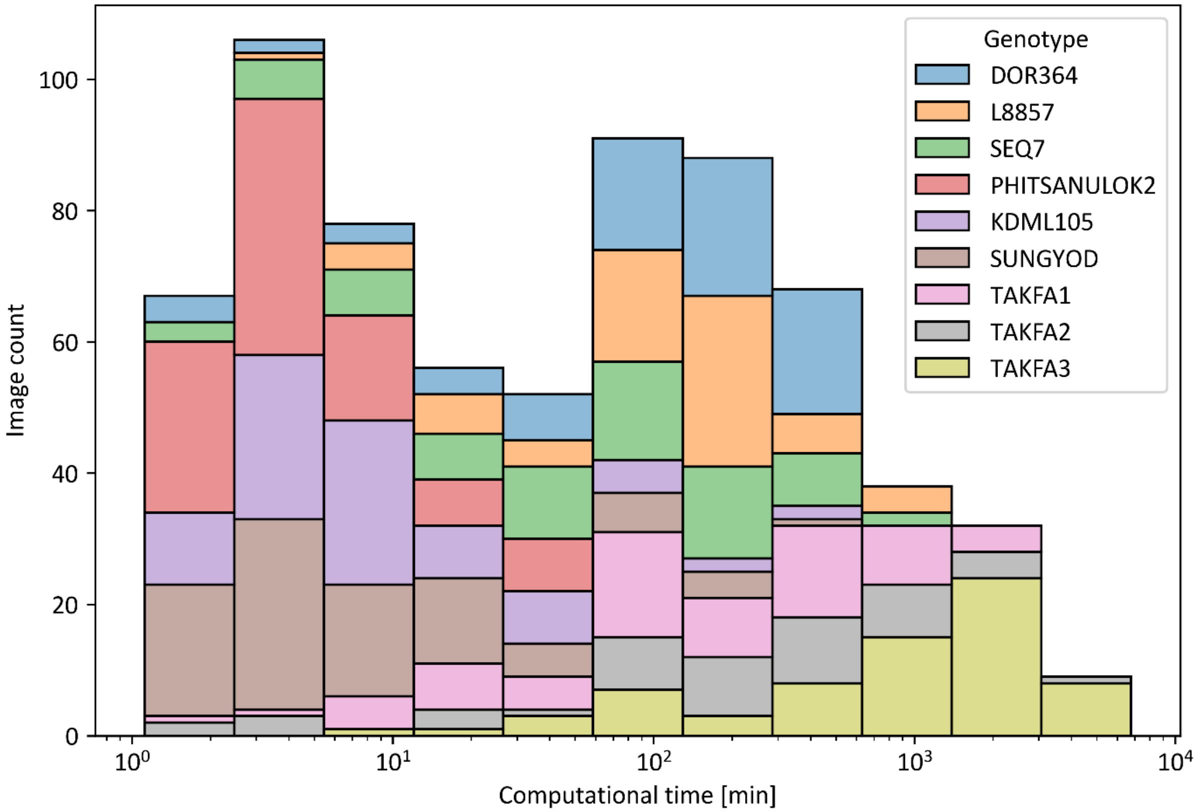

Figure S11: Histogram of computational time to process images in Dataset Mahidol I colored by genotype. The horizontal axis depicts the required computation time required to process an image and the vertical axis depicts the number of images falling into each time bin.

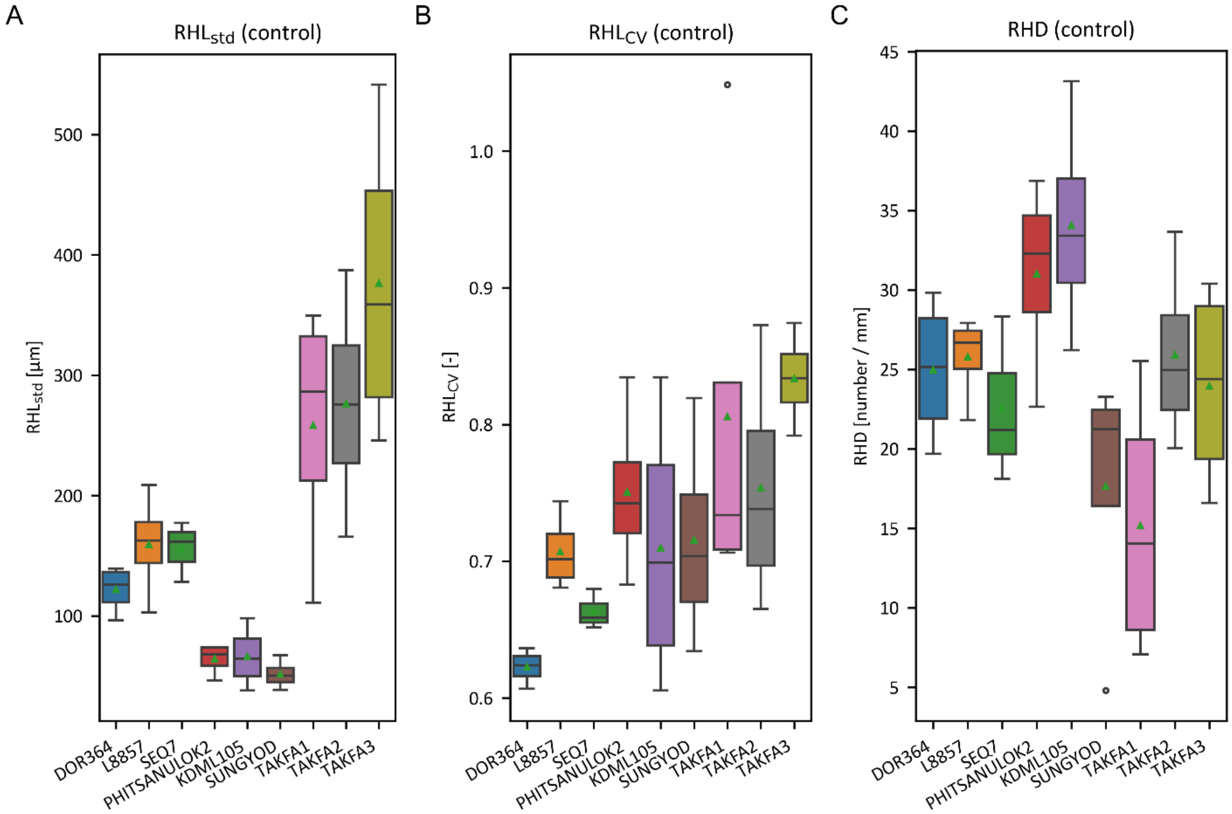

Figure S12: Measurements of root hair traits in the control groups of Dataset Mahidol II. The box displays the quartiles of the distribution, the middle horizontal line represents the median, and the whiskers extend to 1.5 times the IQR from the lower and upper quartiles. Outliers outside the whiskers are represented as circles. The mean of the distribution is displayed as a green triangle. (A) Distribution of RHL_{std} computed in individual plants. (B) Distribution of RHL_{CV} computed in individual plants. (C) Distribution of RHD computed for individual plants.

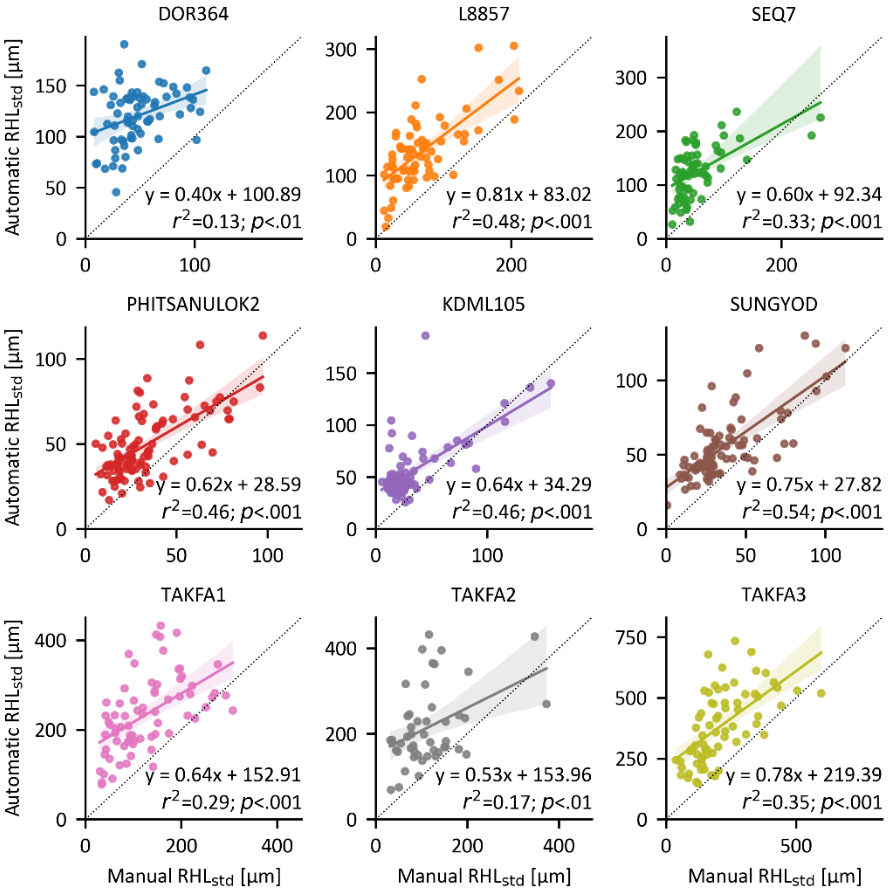

Figure S13: Correlation for automatic and manual measurements of $\mathrm{RHL}_{\mathrm{std}}$. Each plot includes the results of a single genotype. Each circle represents $\mathrm{RHL}_{\mathrm{std}}$ per image. The lines represent the linear regression models with 95% confidence intervals.

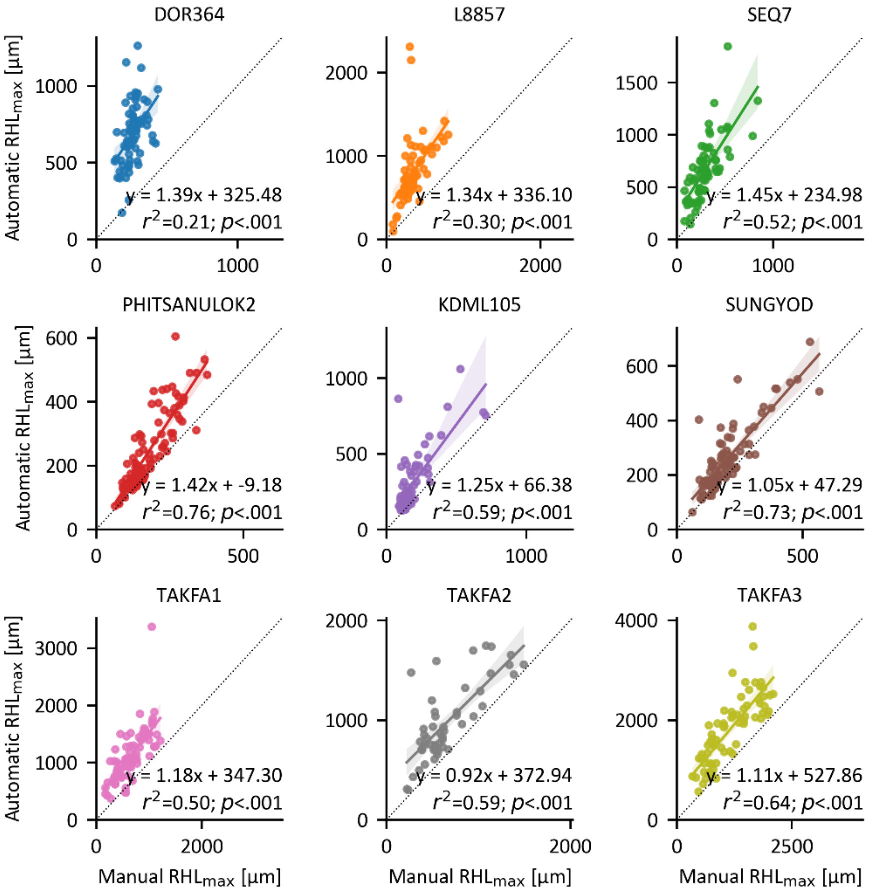

Figure S14: Correlation for automatic and manual measurements of RHL_{max}. Each plot includes the results of a single genotype. Each circle represents RHL_{max} per image. The lines represent the linear regression models with 95% confidence intervals.

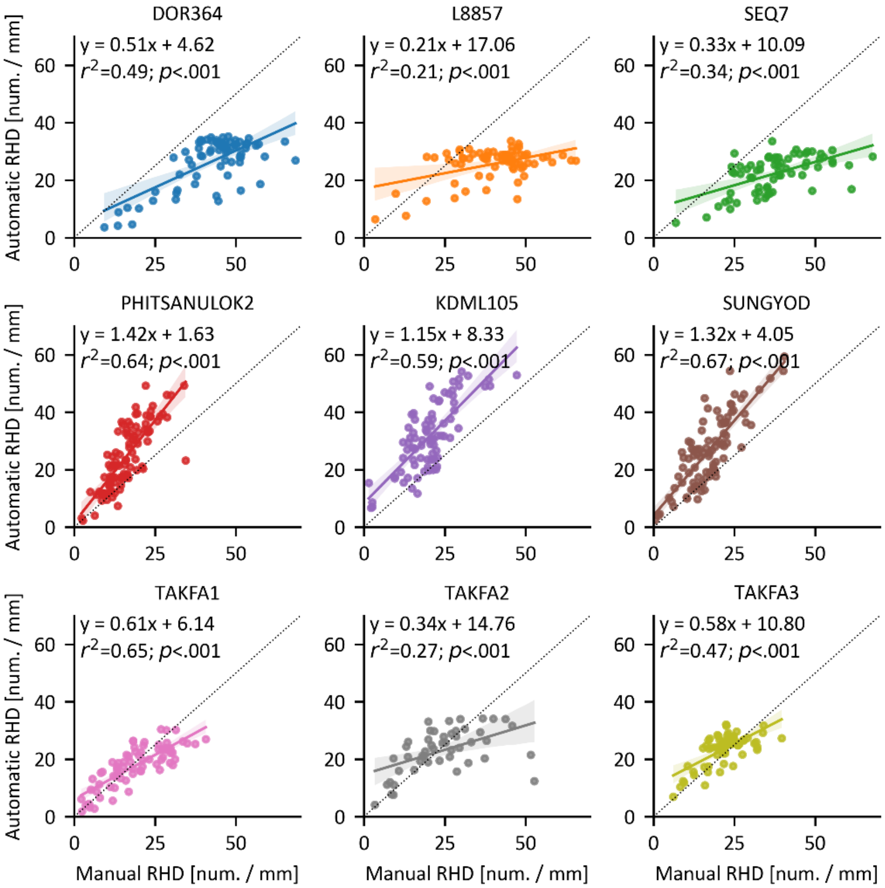

Figure S15: Correlation for automatic and manual measurements of RHD. Each plot includes the results of a single genotype. Each circle represents the RHD in a single image. The lines represent the linear regression models with 95% confidence intervals.

References

Broughton, W. J., & Dilworth, M. J. (1971). Control of leghaemoglobin synthesis in snake beans. *Biochemical Journal*, *125*(4), 1075-1080. https://doi.org/10.1042/bj1251075

Pingault, L., Zogli, P., Brooks, J., & Libault, M. (2018). Enhancing Phenotyping and Molecular Analysis of Plant Root System Using Ultrasound Aeroponic Technology. *Curr Protoc Plant Biol*, *3*(4), e20078. https://doi.org/10.1002/cppb.20078

Qiao, Z., & Libault, M. (2013). Unleashing the potential of the root hair cell as a single plant cell type model in root systems biology. *Frontiers in Plant Science*, *4*, 484.

Virtanen, P., Gommers, R., Oliphant, T. E., Haberland, M., Reddy, T., Cournapeau, D., Burovski, E., Peterson, P., Weckesser, W., Bright, J., van der Walt, S. J., Brett, M., Wilson, J., Millman, K. J., Mayorov, N., Nelson, A. R. J., Jones, E., Kern, R., Larson, E., . . . SciPy, C. (2020). SciPy 1.0: fundamental algorithms for scientific computing in Python. *Nature Methods*, *17*(3), 261-272. https://doi.org/10.1038/s41592-019-0686-2